BLINKING CORRELATION IN NANOCRYSTAL QUANTUM DOTS PROBED WITH NOVEL LASER SCANNING CONFOCAL MICROSCOPY METHODS

by

Ryan Alf Hefti

A dissertation submitted to the faculty of
The University of North Carolina at Charlotte
in partial fulfillment of the requirements
for the degree of Doctor of Philosophy in
Nanoscale Science

Charlotte

2013

Approved by:

_____
Dr. Patrick Moyer

_____
Dr. Marcus Jones

_____
Dr. Stuart Smith

_____
Dr. Yuri Nesmelov

_____
Dr. Jiancheng Jiang

ABSTRACT

RYAN ALF HEFTI. Blinking correlation in nanocrystal quantum dots using novel laser scanning confocal microscopy methods. (Under the direction of DR. PATRICK J. MOYER)

Semiconductor quantum dots have a vast array of applications: as fluorescent labels in biological systems, as physical or chemical sensors, as components in photovoltaic technology, and in display devices. An attribute of nearly every quantum dot is its blinking, or fluorescence intermittency, which tends to be a disadvantage in most applications. Despite the fact that blinking has been a nearly universal phenomenon among all types of fluorescent constructs, it is more prevalent in quantum dots than in traditional fluorophores. Furthermore, no unanimously accepted model of quantum dot blinking yet exists.

The work encompassed by this dissertation began with an in-depth study of molecular motor protein dynamics in a variety of environments using two specially developed techniques, both of which feature applicability to live cell systems. Parked-beam confocal microscopy was utilized to increase temporal resolution of molecular motor motion dynamics by an order of magnitude over other popular methods. The second technique, fast-scanning confocal microscopy (FSCM), was used for long range observation of motor proteins. While using FSCM on motor protein assays, we discovered an unusual phenomenon. Single quantum dots seemingly communicated with neighboring quantum dots, indicated by a distinct correlation in their blinking patterns.

In order to explain this novel correlation phenomenon, the majority of blinking models developed thus far would suggest a dipole-dipole interaction or a Coulomb

interaction between singly charged quantum dots. However, our results indicate that the interaction energy is higher than supported by current models, thereby prompting a renewed examination. We propose that the blinking correlation we observed is due to a Coulomb interaction on the order of 3-4 elementary charges per quantum dot and that multiple charging of individual quantum dots may be required to plunge them into a non-emissive state. As a result of charging, charge carriers are displaced into a wide distribution of trap sites in the surrounding matrix, resulting in the expected power-law probability distribution of off times ubiquitous in quantum dots. Our discovery also implies that quantum dot blinking can be controlled, advocating the creation of switchable nanoscale emitters.

DEDICATION

This dissertation is dedicated to my wonderful wife, Rebecca, who is the love of my life.

ACKNOWLEDGEMENTS

I am indebted to several people for their gracious help through the course of the work summarized in this dissertation. First and foremost, I would like to thank my advisor, Dr. Patrick Moyer. His technical expertise and scientific creativity were both crucial to every aspect of my graduate research. Like all great advisors, he provided excellent guidance whenever needed. Above all, he fostered an environment that encouraged scientific exploration with an enthusiasm that is beyond compare.

I am very thankful to my dissertation committee for agreeing to offer their expertise and guidance for this dissertation. Dr. Marcus Jones has been a tremendous resource in and out of group meetings. His expertise has been invaluable in the development of a large portion of the ideas that will be summarized on the pages that follow. Dr. Stuart Smith and Dr. Yuri Nesmelov have both offered a great deal of assistance and guidance throughout many stages of my research. Special thanks go to Dr. Jiancheng Jiang for joining my committee and offering his support.

Our research group has been a tremendous one throughout my graduate career. Fellow member Wes Parker worked countless hours in the lab with me exploring hundreds of motor protein assays. He also provided sound advice and perspective, both of which I still consider and appreciate today. Dr. Sharonda LeBlanc has also provided help whenever needed and has been an excellent resource in the progression of my research. Julie Harriss was an amazing contributor despite only being a formal member of our group for one summer. She conducted experiments and analyzed data with an efficiency that I almost would not have believed possible. I will be forever grateful for her contributions. Todd Mendenhall and Kaleb Templeton, who only recently joined our

group, have quickly become superb experimentalists. They have both contributed substantially to this body of work.

I am very appreciative of all of the feedback and contributions from numerous members of other groups, particular the Jones group. Danielle Woodall, Scott Williams, Dr. Kevin Major, Drew Tobias, Gaurav Singh, Jose Castaneda, and Michael Guericke have all provided vital feedback and unique insights into my research. I am grateful to Cheng Li for including me in his exciting work in optical materials. Dr. Feilong Lin graciously chose to develop our custom imaging software as part of his graduate project and I appreciate his expertise every time I set foot in our lab.

Dr. Christopher Yengo and his research group were instrumental for the motor protein research detailed herein. By providing most of the myosin V studied as well as a majority of the biologically sourced reagents, we only then were able to perform the needed experiments. Likewise Dr. Kathy Trybus and Dr. Alex Hodges contributed multiple reagents and myosin V motor constructs during our work with the assays. Without their help, we would have never gotten our fast scanning experiments off the ground.

I am extremely thankful for Dr. Thomas Schmedake and his diligence while recruiting me into the Nanoscale Science program in the first place. Numerous other people have made the program a success in short order and I am indebted to all of them as well. I would especially like to thank Dr. Jordan Poler, Dr. Bernadette Donovan-Merkert, and Dr. Edward Stokes who have all made a sizeable impact while I have been in the program. I am also grateful to Caroline Kennedy and Robin Burns for their unwavering commitment to supporting students and faculty in the program. Dr. Robert

Hudgins, Dr. Lou Deguzman, and Alec Martin each offered specialized training on various instruments and I am indebted to them all for their help.

One person deserves special recognition for the effect he has had on me, particularly on my development as an educator. Dr. Richard Jew has continually offered brilliant advice in all aspects of scientific pedagogy. He has been a resolute advocate for the advancement of my career as an educator for the duration of my teaching assistant career. Quite notably, he has demonstrated a superior style of teaching and a dedicated attitude towards education that I can only hope to emulate in the future. I would also like to thank Susan Michael for her incredible support in many of the same ways. My appreciation for both Dr. Jew and Mrs. Michael cannot be overstated.

Most importantly, I would like to thank my wife, Rebecca Hefti. She may be the only person to have read every word in this dissertation. While that alone would be amazing, she has also been unendingly supportive throughout my time as a graduate student. In reality, the appreciation I owe her cannot be sufficiently expressed here in a reasonable number of words.

There are numerous people not specifically mentioned that have directly impacted my tenure as a graduate student. My appreciation is not limited to the people listed here. There are many students, peers, and mentors who I undoubtedly value, particularly those that have been a part of my graduate school experience. I would like to thank everyone who has been a part of my life in any way for the past five years. You have all played a role in shaping who I am today.

TABLE OF CONTENTS

LIST OF FIGURES

LIST OF TABLES

LIST OF ABBREVIATIONS

ADP	adenosine diphosphate
APD	avalanche photodiode
ATP	adenosine triphosphate
BPF	band-pass filter
BSA	bovine serum albumin
CdSe	cadmium selenide
CPR	center peak ratio
DBS	dichroic beam splitter
DTT	dithiothreitol
F-actin	filamentous actin
FRET	Förster/fluorescence resonance energy transfer
FSCM	fast-scanning confocal microscopy
FWHM	full width at half maximum
HBT	Hanbury Brown and Twiss
KMg50	potassium and magnesium based buffer
LSCM	laser scanning confocal microscopy
NEM	N-ethylmaleimide
PMMA	poly(methyl methacrylate)
PPMCC	Pearson product-moment correlation coefficient
PSF	point spread function
PZT	lead zirconium titanate
SEM	scanning electron microscope

smFRET	single molecule fluorescence resonance energy transfer
TIRF	total internal reflection fluorescence
ZnS	zinc sulfide

CHAPTER 1: INTRODUCTION

Over three decades ago, nanocrystal quantum dots were first discovered[1] and have since become useful in an enormous range of applications. A few sample niches that quantum dots have occupied are as probing tools in biological systems,[2-6] as physical and chemical sensors,[7-10] and as photovoltaic devices.[11-15] Even though their prominence continues to grow, many phenomena about quantum dots are not fully understood. One attribute still debated is the blinking, or inconsistent fluorescence, which most quantum dots exhibit.[16-18] The motivation behind this research is to provide fresh insight into the mechanism of quantum dot blinking with the hope that a universal model of blinking behavior may soon be developed. In order to utilize quantum dots to their fullest potential in applications such as those listed above, the blinking must be fully understood and preferably controlled in quantum dot systems.

Quantum dots, often referred to as nanocrystals, are semiconductor materials with a size such that electron-hole pairs, or excitons, generated are confined in all three spatial dimensions.[1] The result is that quantum confinement of the exciton largely influences the band gap, or distance between the ground state and the first excited state. The degree of confinement is dictated by the size of the quantum dot, which means that the band gap, and therefore fluorescence wavelength, is tunable according to the size of the synthesized nanocrystals.[19-21] All else being equal, the size of a quantum dot is inversely proportional to the band gap energy of the nanocrystal.[20] This is enormously convenient in the

colloidal synthesis of quantum dots since a range of sizes can be synthesized during a single reaction.[22] Besides the utility of optimizing the size of quantum dots for particular fluorescence emission energies, the excitation energy required to excite electrons is likewise proportional to the band gap. Therefore, tailoring the size of quantum dots to maximally absorb or emit a certain wavelength of light is also feasible.

A tunable band gap is only one of several prominent features of quantum dots that make them ideal candidates for multiple applications. Their resistance to photobleaching relative to molecular probes, especially compared to organic molecules,[3] makes many studies more viable. Their high mechanical stability in biological systems has been often noted as well.[2-4,8,23] In addition, quantum dots are tremendously luminescent in comparison to their counterparts, lending primarily to their substantially large absorption cross sections.[24] Other potentially beneficial features include long fluorescence lifetimes, a broad absorbance spectrum, and customizable ligands.

Despite all of the advantages of using quantum dots over analogous molecular fluorophores, especially in single-molecule experiments, some disadvantages must also be noted. Many nanocrystals contain materials that are toxic to relevant biological systems.[25] With sizes in the range of 2-20 nm, quantum dots can also be intrusive in certain applications. Added ligands can further add to their size, which can further limit their application when minimal size or mass is vital. Finally, a commonly discussed characteristic of quantum dots is their proclivity to fluorescence intermittency, or blinking. An ideal fluorophore would emit constantly without seemingly random fluctuations in fluorescence. So, it is vital to understand the cause of blinking and continue to investigate possible solutions. Although most fluorophores, like organic dyes

and fluorescent proteins, also exhibit blinking, the prominence of blinking in quantum dots is generally more pronounced.[16] A standard blinking trace is shown in Figure 1.1, where the photon counts are plotted over the course of approximately 17 seconds. Photon counts are totaled every 20 ms, producing the histogram shown in the Figure. The nanocrystal is a common cadmium selenide core with a zinc sulfide shell (CdSe/ZnS).

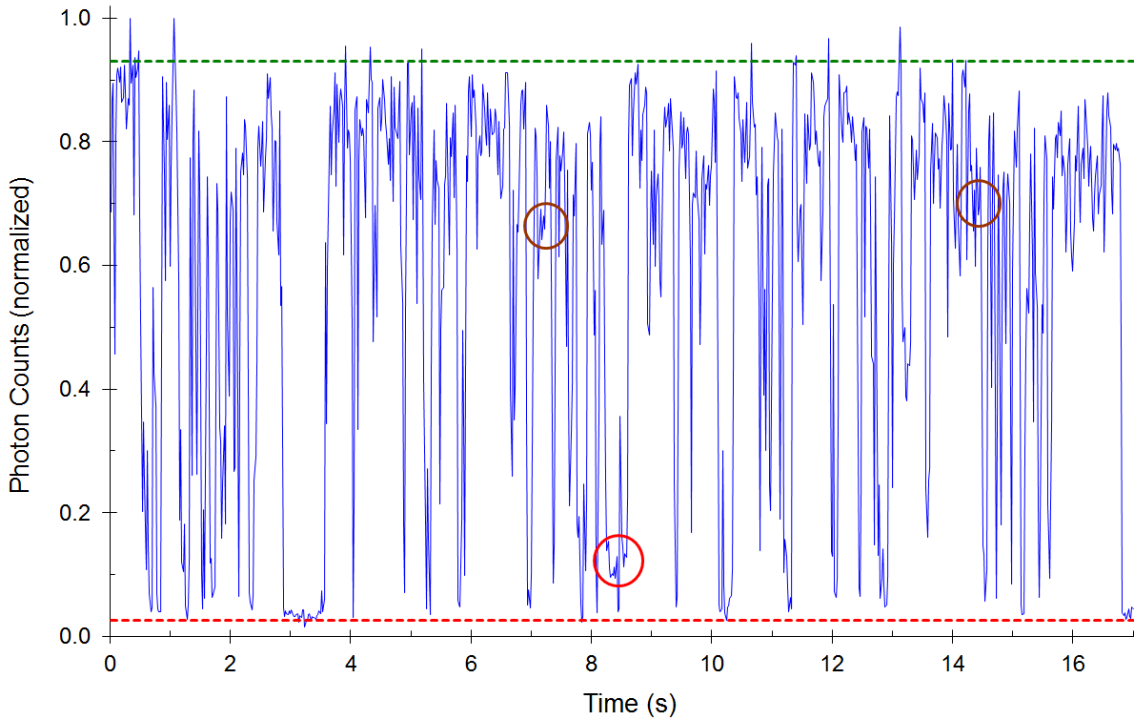

Figure 1.1: Blinking trace of a CdSe/ZnS quantum dot. The green and red dotted lines represent approximations of a fully emissive level of photon counts and non-emissive level of photons counts, respectively. Circled areas exhibit possible intermediate states in which the quantum dot is neither fully emissive nor in a non-emissive state.

Multiple blinking models to explain the observed dynamics have been proposed. The most prominent model asserts that the ejection of a single electron is primarily responsible for shifting an emitter to an off-state.[17] The trapped electron exists somewhere in the matrix surrounding the dot, thereby creating an ionized environment in

which Auger processes dictate the fate of excitons. Instead of the normal luminescent decay of an excited electron, non-radiative recombination dominates. If and when the trapped electron recombines, the dot may again photoluminesce since Auger decay is not as likely. Most proponents of this model argue that the hole from the electron-hole pair involved in ionization may also be delocalized and become trapped near the shell or on the surface of the quantum dot.[26] After such an event, the quantum dot would be temporarily returned to an emissive state until the electron-hole pair recombine or until the return of either charge carrier to the core of the nanocrystal.

Some of the detractors to this model argue that Auger recombination is not sufficient to plunge a quantum dot into a complete dark state, as is often observed experimentally.[27] Zhang *et al.* found experimental evidence that quantum dots continue to emit even after being charged and therefore do not display discrete on and off states.[27] The finding was confirmed by other groups as well, who found that intermediate emissive states were possible.[28] Quantum dots are thought to experience charged states, which can still be emissive, even if at reduced intensity levels.[29] This phenomenon is illustrated in Figure 1.1 as noted by the circled areas. In each of the noted locations, the fluorescence intensity is neither at the peak (on) nor at the lowest intensity level (off). Instead, the quantum dot displays a fluorescence intensity corresponding to a middle point between fully emissive and non-emissive exists, now commonly known as an emissive gray state.[29-31]

One of the most popular rationalizations for the existence of gray states is the model classified as a multiple charging scenario.[29,32,33] The multiple charging model also serves to explain other anomalies that the single charging model fails to explain. Since

Auger processes have been shown to be dominant with rates that far exceed fluorescence lifetimes,[34,35] a biexciton or multiexciton state should yield sufficiently low photoluminescence quantum yields since Auger processes are likely in both cases. However, Zhao et al. observed quantum yields for quantum dots in biexciton and multiexciton states that were an order of magnitude greater than predicted by a single charging model.[32] Researchers have further argued that Auger recombination alone is insufficient to explain off states of quantum dot systems.[36] Califano argued that multiple charging can account for the dynamics of partial on states and full quenching of emission to off states.[33]

Insight into blinking mechanisms is provided by quantifying the on and off times of quantum dots, which are well known to fall into a wide distribution spanning 4-7 decades.[18] If a single rate was responsible for shifting the emissivity, a probability distribution of on and off times would be exponential. However, the probability distribution consistently follows an inverse power law.[18,26,37,38] To explain the power law behavior, a large number of rates must be responsible for shifting the emissivity of an emitter. If change in emissivity was dependent on a single rate, the probability distribution of on or off times would follow an exponential function.

So far, the discussion of multiple charging has been primarily focused on scenarios in which either positive or negative trions exist. Although the charged trion model resolves some of the inconsistencies of the single charging model, such as grey states, we propose that multiple charging be expanded further to include multiple ejected charge carriers, which may become trapped in the surrounding matrix. We find that two quantum dots, separated by distances of up to one micrometer, fundamentally

communicate through their blinking pattern. The blinking of neighboring dots is correlated, suggesting a long-range interaction between quantum dots that cannot be explained by a single charging model.

The discovery of the blinking correlation phenomenon occurred only due to an endeavor to establish laser scanning confocal microscopy (LSCM) as a viable tool for studying biomolecular motor motion dynamics. We developed two novel LSCM methods, one of which offers temporal resolution of full motor dynamics that is superior to all popular observation techniques. The second technique further established LSCM as an appropriate tool in the study of molecular motors. More importantly, the discovery of the blinking correlation phenomenon was a direct result of the unique images generated by the method.

The use of a multiple charging model to explain the blinking correlation between quantum dots is further supported by numerous experiments. The temporal separation between excitation of neighboring quantum dots is first varied in a set of experiments. Then, excitation intensity, which is expected to drive the level of multiple charging,[39] is varied while the blinking correlation, fluorescence lifetime, and multiphoton emission is measured from multiple sets of quantum dots. The blinking correlation is also studied in an environment in which multiphoton emission dominates, providing further insight into the overall mechanism. Multiphoton emission is studied even more thoroughly in a series of single quantum dot scanning experiments, shedding new light on multiphoton emission dynamics.

Certain blinking mechanisms proposed thus far can be corroborated with the discovery of blinking correlation. Ejected charges almost certainly settle into a wide

distribution of trap sites located in the surrounding matrix. Much like the mechanism proposed by Verberk *et al.*,[26] this allows for a power law distribution of off times due to the inherent inhomogeneities among various trap sites. To explain the on time power law probability distribution, varying degrees of multiple charging can be considered. Verberk *et al.* considered that an electron ejection could be closely followed by relocation of the hole to the shell or trap sites on the nanocrystal surface, resulting in a long lived emissive state while a Coulomb blockade would prevent further ionization.[26] While the dynamic shifting of a hole could also be supported by a multiple charging model, the Coulomb blockade would have to be minimally effective to allow for further charge ejection. However, an amply large distribution of on times could result from the dynamic surface or shell trapping of multiple holes, as opposed to a single hole, coupled to previously ejected electrons.

Several applications of blinking correlation could be developed through future work. Optimizing conditions for the blinking correlation phenomenon might pave the way for switchable nanoscale emitters, in which the on and off states of individual quantum dots could be controlled by a simple interaction mechanism. Another viable opportunity would be the utilization of quantum dots as electric field sensors. Provided that their emissivity can be controlled by an electric field potential in their vicinity, it is possible to directly measure an electric field and its strength using strategically placed nanocrystal quantum dots. Although the work summarized by this thesis has been focused on the discovery and explanation of the blinking correlation phenomenon, future experiments could provide the basis for these types of devices. The first step in realizing

such devices is to enhance the blinking correlation effect by altering specific conditions, many of which are explored in the following pages.

CHAPTER 2: EXPERIMENTAL APPARATUS

The majority of the work presented here has been accomplished using a home-built laser-scanning confocal microscope. The capabilities of the microscope include fluorescence imaging, time-resolved fluorescence microscopy, photon antibunching, and photoluminescence spectroscopy. There are numerous derivatives of these techniques that will be detailed later, most of which are made possible by the fact that the instrument is entirely customizable with appropriate optics, detectors, a scanning stage, high temporal resolution electronics, as well as custom imaging software. A schematic of the home-built microscope is shown in Figure 2.1.

The laser excitation source is selectable, and typically one of two options was utilized for our studies. The first laser source is a picosecond pulsed laser diode source, with a fixed wavelength of 420 nm and peak power of 1 mW. The laser pulse repetition rate was almost exclusively set at 10 MHz. The pulse width, dependent on laser power, ranged from 70 ps to 300 ps. The second laser source, a tunable argon-ion continuous wave laser, is capable of emission wavelengths ranging from 454 nm to 514 nm. The peak power level for the argon-ion source is wavelength dependent, but generally is capable of approximately 100 mW.

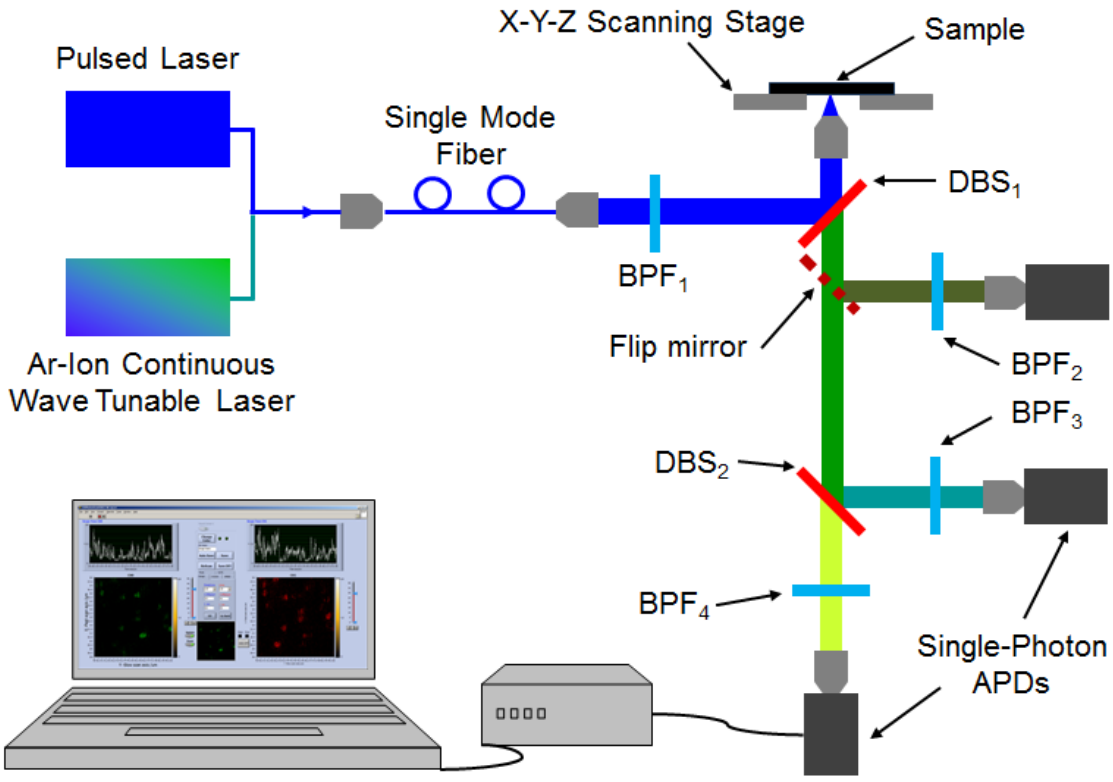

Figure 2.1: Schematic of home-built laser scanning confocal microscope. The entire light path is indicated, from the laser source to the avalanche photodiode detectors.

Both the pulsed and the continuous wave laser are coupled into a single mode optical fiber using a 10x objective lens. By narrowing the modal distribution of the excitation laser, the light can then be columnated using a second 10x objective lens while also propagating with a well-defined beam profile. To eliminate most of the outlying frequencies from the excitation source, a band-pass filter (BPF) with a 20 nm bandwidth is placed in the excitation path. The excitation beam is then reflected by the main dichroic beam splitter (DBS) and reflected by another mirror into the main objective lens, which is a Nikon 100x lens with a 1.25 numerical aperture. The beam is focused onto the sample surface, which is attached to the scanning stage. The stage is a high-speed lead zirconium titanate (PZT) actuated 3-axis "nanopositioning system" from Mad City Labs.

It has considerable lateral range of 75 μm in the plane of the sample as well as a focal range of up to 50 μm. Scan speed can be adjusted up to 400 Hz, supporting nearly 2 images per second for standard 256 x 256 pixel resolution images.

Fluorescent light is collected by the main objective lens and directed back towards the main DBS. Careful choice of the correct DBS assures that the majority of the emitted light passes through it instead of being reflected like the incident laser light. A flip mirror is used to direct light to a specialized imaging avalanche photo diode detector (not shown in Figure 2.1). Often, the mirror is down, permitting the use of a second DBS, which further splits the light when using dual emitters or performing two simultaneous experimental studies. After the second DBS, an appropriate BPF is placed in line with each detector path. Both of the detectors are avalanche photo diodes with the flexibility to be routed to either the imaging system or to the computer system used to perform high resolution time-resolved studies.

Custom LabView based imaging software is loaded on one computer system to handle the imaging data from any of the three detectors. Full stage control is provided through the custom software as well. The standard software interface is shown in Figure 2.2. A two color sample is demonstrated in the interface and the numerous software features are noted in the caption of Figure 2.2.

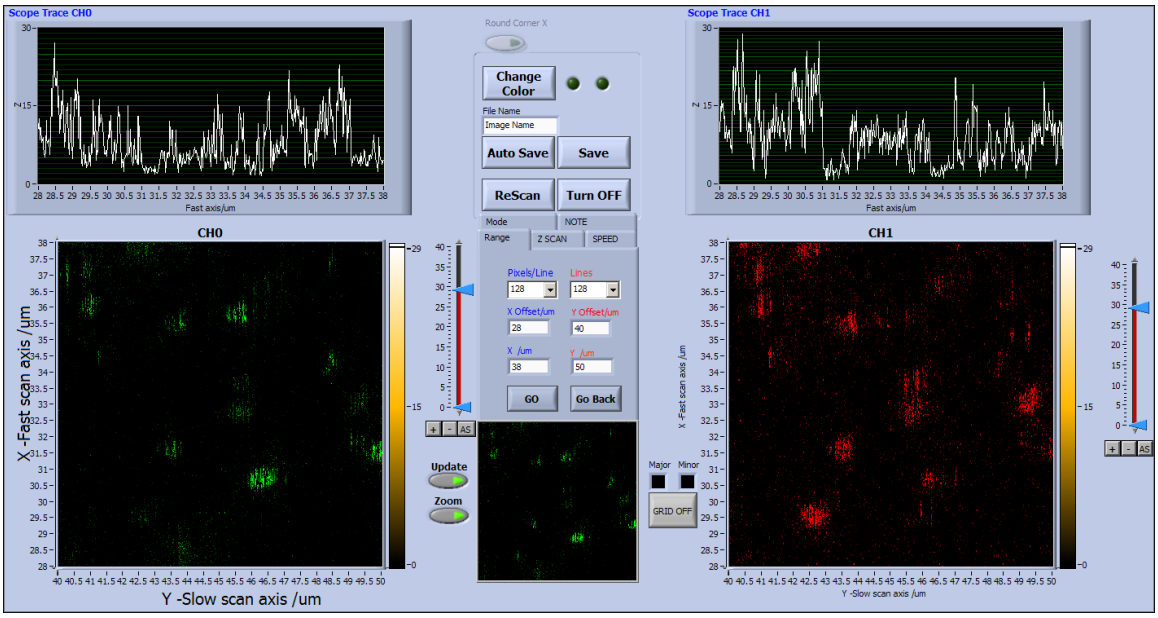

Figure 2.2: LabVIEW Imaging software interface. Pixel density, scan range, color profiles, and scan speed could all be controlled through the custom interface. Additional features, such as focus, custom image contrast, quick zooming, continual saving, and reverting to a previously scanned area were also incorporated into the software.

In order to probe time-resolved dynamics of systems, the laser driver delivers a pulsed signal concurrently with each light wave pulse. The pulsed signal is delivered to a time-correlated single photon counting computer board made by Picoquant. With 4 input channels, a time resolution of about 30 ps, and the ability to process up to 3 million photons per second, the board supports many time-resolved studies. Studies requiring macro time-tagged and intra-pulse time-resolved recording were made possible using the computer board. One important example of time-resolved studies includes lifetime decay experiments, which are conducted in reverse start-stop mode. Reverse start-stop mode requires that a photon be received by a detector which is in turn marked as the start time. The stop time is marked when the next pulse signal from the laser driver is delivered to the computer board. Since the laser pulses at a constant rate, a simple calculation

provides the actual time from incident pulse to emitted photon, namely the radiative lifetime decay for the detected photon.

A slightly modified configuration of a detector's output signal can be used for photon correlation experiments. Using what is known as a Hanbury Brown and Twiss[40] (HBT) setup, the pulse generated by the laser driver is disconnected and in its place the output from one of the detectors is connected. In the HBT setup, the two detectors furthest from the excitation source were used since a DBS, non-polarizing cube beamsplitters, or polarizing beam splitter could be placed at the DBS_2 location in Figure 2.1. One detector is designated as the pulse signal since any photons received by it define the start time, also known as the zero time. Any photons received by the other detector are sorted relative to the start time. Photons are correlated to each other based on their temporal separation between the two detectors. A histogram of the time differences is then generated.

CHAPTER 3: MYOSIN V STUDIES

3.1 Background and Motivation

My first undertaking as a graduate student was to develop and refine an LSCM technique to study motion dynamics of biomolecular motors, which are also generally referred to as motor proteins. Among the three most common motor proteins, myosin, kinesin, and dynein, myosin V was chosen for these studies, primarily due to its availability. Motion dynamics have traditionally been explored using total internal reflection fluorescence (TIRF) microscopy.[41-43] A significant disadvantage to using TIRF is that the maximum imaging depth is approximately 200 nm. Using LSCM, it is not only possible to image to depths of several micrometers, but three dimensional images can be generated, potentially revealing even more information about motor protein dynamics. In the course of the work with myosin, we developed two viable techniques for examining molecular motor motion with LSCM. To prove the *in vivo* viability of both techniques, we also created a patterned nanostructure array to better emulate cytoskeletal structure.

Motor proteins have long been admired for their utility in nature as well as their extraordinary attributes and capabilities. Almost every organism on the planet makes use of motor proteins, whether in muscle motion, cellular motility, intracellular transport, among many other functions. The size of most motor proteins ranges from a few nanometers to almost a micrometer, yet they seamlessly interact in a concerted manner to

provide the mechanical force in the muscles of all animals. In the hectic environment of a cell's cytoplasm, individual motors accomplish tasks such as cargo transport in absence of any apparent external directing stimuli. Among all of these attributes, many motor proteins maintain efficiencies of nearly 100%,[44] which is almost implausible, considering that useful macroscopic motors always demonstrate less than perfect efficiency. Nearly all motor proteins convert chemical to mechanical energy by way of a readily available reaction, the hydrolysis of adenosine triphosphate (ATP) to adenosine diphosphate (ADP). The hydrolysis of ATP is an exergonic reaction and the thermochemical equation is noted as

$$\mathrm{ATP}^{4-} + \mathrm{H_2O} \rightleftharpoons \mathrm{ADP}^{3-} + \mathrm{HPO_4}^{2-} + \mathrm{H}^{+} \quad \Delta G = -30.5\ \mathrm{kJ/mol} \qquad (3.1)$$

under normal physiological conditions. The reaction is easily reversible to maintain appropriate ATP concentrations in order to sufficiently supply energy to molecular motors.

A basic drawing of a myosin motor protein is shown in Figure 3.1. The location of ATP hydrolysis is contained in the head of the motor, which is where the motor contacts actin filaments, which is the structure on which the motor steps in order to move. The neck of the motor contains the light chains, which are important in the regulation of motion and dictating the primary actions of the motor. The tail is mostly structural in nature, providing a location to attach to cargo or be used as an anchor point for synchronizing motion with other motors. Although the structure of other motors differs from that of myosin V, most of the functional elements are essentially the same.

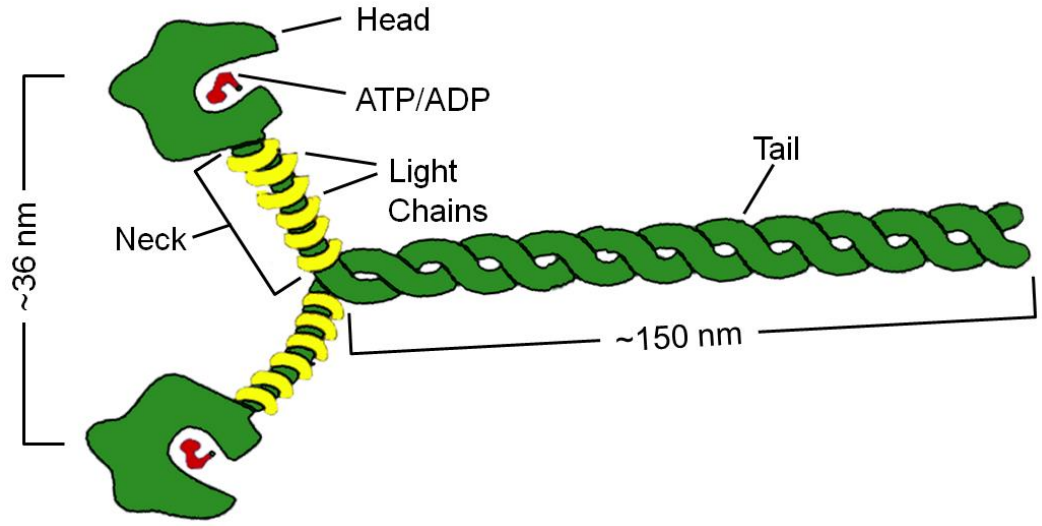

Figure 3.1: A myosin V construct is shown with all major components noted. Myosin, in addition to many other molecular motors, "walks" on its head while the tail is used for carrying cargoes or entangled with other proteins in muscle systems.

To control motor proteins and utilize them in specific applications, particularly on the nanoscale, the mechanics of their motion must first be understood. The means by which they accomplish such outstanding efficiencies and direct themselves seemingly in absence of a central control point in a cell must also be ascertained. Their motion dynamics have been studied intensely for the past decade. However, new techniques are always in development to learn new information about motor proteins. Since the majority of studies are done *in vitro*, techniques that can apply to live cells are in high demand. Confocal microscopy provides a means to image and track single motor proteins in live cells. Therefore, our focus was to develop techniques that could be applied to *in vivo* studies in order to learn as much as possible about motion dynamics in the natural environment of a motor protein.

The first technique, designated the parked-beam method, was developed with the intention of vastly improving temporal resolution of motor protein motion dynamics

while maintaining the spatial resolution of popular techniques. TIRF imaging of motor proteins, capable of spatial resolutions on the order of a single nanometer, is generally limited temporally to resolutions of 200 ms to 1 s, depending on the instrument and experimental conditions.[41,45] Holden *et al.* recently reported a tenfold improvement in the temporal resolution of TIRF for a single molecule Förster resonance energy transfer (smFRET) experiment.[46] Still, TIRF falls short of the temporal resolution of widefield epifluorescence microscopy techniques, which have also been used to image and track individual motor proteins. Pierobon *et al.* reported a temporal resolution of 5 ms while tracking myosin V *in vivo*.[47] We demonstrate that the parked-beam method attains a temporal resolution of 10 ms using a standard molecular fluorophore. By using a brighter probe, such as a quantum dot, this could be improved to resolutions of 1 ms or better, given the superior brightness of quantum dots. Spatial resolution is not sacrificed, given that the parked-beam method localizes the position of individual molecules to within 2-3 nanometers.

Another technique, fast-scanning confocal microscopy (FSCM), was designed to image the length of any filament while monitoring motor activity at all points along the filament. Temporal resolution of FSCM is at least 100 ms, with spatial localization to within 2-3 nanometers. Although FSCM cannot attain the temporal resolution of the parked-beam method, it does offer distinct advantages. Namely, multiple motors can be monitored at one time while individual motors can be tracked for distances greater than the width of the laser intensity profile.

Both techniques offer spatial resolutions comparable to other popular single molecule tracking methods while exceeding temporal resolutions of most methods used

to image and track motor proteins. Additionally, they can both be applied directly to *in vivo* studies since LSCM can image to any depth of most cells. The techniques are very adaptable and can typically be implemented on nearly any standard confocal microscope system.

3.2 Assay Preparation and Challenges

The *in vitro* assays prepared for the myosin experiments all followed the same general preparatory steps. Glass microscope coverslips, measuring 25 x 25 mm, were first thoroughly cleaned with ethanol and lint free disposable cleaning cloths. The coverslip was then coated with approximately 4 μL of 1% nitrocellulose with any excess nitrocellulose solution removed using a sweep of a spare coverslip. This assured complete, relatively uniform nitrocellulose coverage of the primary coverslip with a minimal thickness of the layer. Two pieces of double sided clear tape were then applied parallel to one another on top of the nitrocellulose-coated side with a space of 7-10 mm between the tape pieces. An 18 x 18 mm coverslip was applied on top of the tape to create a channel between the two coverslips with a height of roughly 100 μm. Subsequently, assay injections of 12 μL were made with each step of the process overviewed in Figure 3.2. Throughout the process of assay preparation, all injected solutions were kept on ice to advocate protein viability. Injections were made on a specific timeframe, which is outlined in Table 3.1.

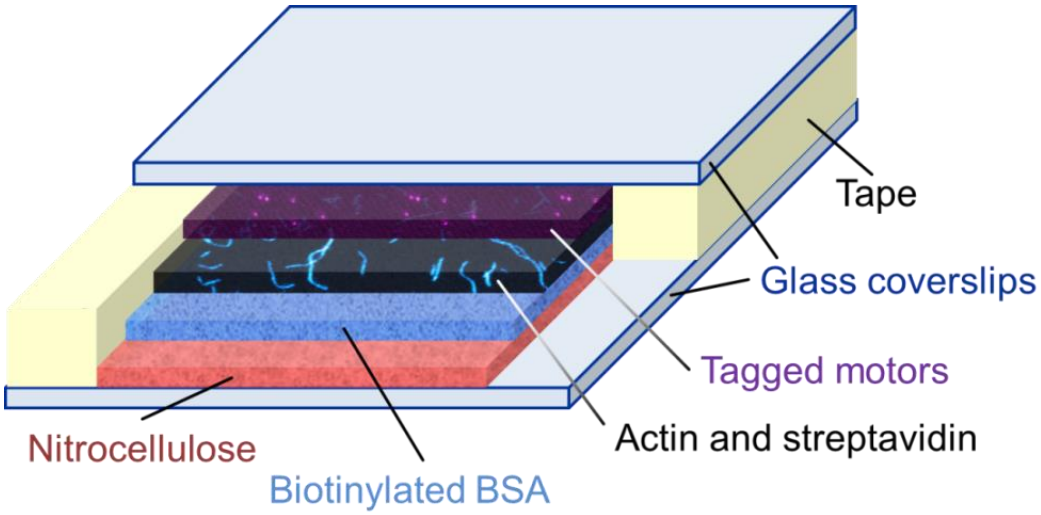

Figure 3.2: Construct of the assay chamber used for many myosin V studies. The most important assay injections are shown sequentially as layers between two glass coverslips.

All injections were prepared by dilution into KMg50 buffer. KMg50 buffer, a common biological assay solution, is comprised of 50 mM potassium chloride, 1 mM magnesium chloride, 1 mM ethylene glycol tetraacetic acid, 1 mM dithiothreitol, and 10 mM imidazole-hydrogen chloride. The first aliquot injected into the assay channel, after a buffer rinse, served to anchor actin filaments to the larger coverslip. Biotinylated bovine serum albumin (BSA) was used to tether actin filaments since biotin has a strong affinity for streptavidin. A concentration of 1 mg biotinylated BSA per 1 mL of buffer solution was used for the injection. The following injection of streptavidin with a concentration of 0.2 mg/mL assured that streptavidin molecules would be firmly affixed to the primary coverslip and ready to accept actin filaments.

Biotinylated actin was added in the next injection. It was prepared using monomeric rabbit skeletal muscle actin available from Cytoskeleton, Inc. In 143 µL of distilled water, 20 µL of KMg50 buffer and 30 µL of 6.6 µM Alexa Fluor® 488 phalloidin were combined. A 1.0 µL aliquot of 1.0 M ATP and 2.0 µL of 1 M

dithiothreitol (DTT) were added to the mixture as well. The polymerization of the actin was completed by adding 4 μL of 2 mg/mL biotinylated actin and placing the resulting solution in the dark for 1 hour at 25° C. This resulted in a 1 μM solution of labeled filamentous actin (F-actin).

About 12 μL of 60 nM F-actin was injected, which firmly affixed it to the main coverslip. Myosin V, labeled with rhodamine 6G was added to the assay using a concentration of about 2.0 nM. Pre-labeled myosin was obtained directly from collaborators and therefore only dilution to appropriate concentrations was necessary. Finally, an activation buffer containing ATP was added to the assay.

The activation buffer was prepared by first mixing an activation stock solution. The stock solution combined 200 μL of methycellulose, 140 μL of distilled water, 10 μL of 250 μM calmodulin, and 10 μL of 250 mg/mL glucose. Immediately preceding assay injection, 2 μL of 1 mM ATP, 1 μL of glucose oxidase/catalase solution, and 0.1 μL of 1 M DTT were added to 50 μL of the activation stock solution. For most of the samples observed using the parked-beam method, the assay concentration of ATP was 25-40 μM. Between all assay additions noted, a 10 μL KMg50 buffer injection was made to rinse untethered proteins and stray molecules out of the assay. A summary of the assay preparation process can be found in Table 3.1, where the most common version of the assay prepared is detailed. Parameters such as actin, myosin, or ATP concentration, specific label, and type of myosin motor could all be modified from the general outline listed. The assay was typically active for at least 30 minutes after the final injection of ATP. Myosin activity was observed up to 2 hours after the final injection at atmospheric conditions.

Table 3.1: Standard myosin assay detailing individual injection amounts, contents and function of each injection, and the time delay after each injection.

Injection number	Volume (μL)	Injection contents	Purpose	Time (min)
1	20	KMg50 buffer solution	rinse and clean of chamber; establish proper pH level	5
2	12	biotinylated BSA (1 mg/mL)	attachment point for streptavidin	4
3	12	KMg50 buffer solution	rinse excess BSA out of channel; maintain pH	2
4	12	streptavidin (0.2 mg/mL)	anchor for actin filaments	4
5	12	KMg50 buffer solution	rinse excess streptavidin out of channel; maintain pH	2
6	12	Alexa Fluor® 488 labeled biotinylated muscle actin (60 nM)	fixed actin filaments	4
7	12	KMg50 buffer solution	rinse excess actin filaments out of channel; maintain pH	2
8	12	rhodamine 6G labeled wild-type myosin Va (2 nM)	attach motors directly to filaments in preparation for activation with ATP	4
9	12	activation solution (25 μM ATP)	provide source of ATP for myosin motors	-

The assay conditions detailed in Table 3.1 were optimized through a significant amount of trial and error. For example, the process used to polymerize actin was modified several times in order to produce appropriately long filaments with adequate assay stability. The primary modified parameters included the concentration of

monomeric actin used and the timing of the addition of phalloidin functionalized fluorophore. Many reagents were freshly prepared on a daily basis while nearly all others were prepared fresh on a weekly or biweekly basis. To assure purity of all assays, the pH was measured on a consistent basis and maintained between 7.0 and 7.5. Reagents were remade immediately if an aberration in pH was detected.

Various other problems with actin were also encountered. Some assays were built using N-ethylmaleimide (NEM) myosin, which is an inactive from of myosin that retains a strong binding affinity for actin. Since the tail of myosin attaches well to the nitrocellulose layer, NEM myosin can replace the BSA and streptavidin layer while permitting the use of non-biotinylated actin. However, nearly all assays with an NEM myosin base exhibited poor results in tethering or bundling of actin filaments.

The numerous issues encountered in preparing a stable actin layer are summarized in Figure 3.3. Satisfactory labeling of actin filaments was strongly dependent on the process of actin polymerization and the concentration of fluorophore used. Images like the one shown in the upper right of Figure 3.3 were indicative of labeling problems. Improper polymerization would also result in insufficiently long filaments, which is also shown in the upper right of the figure. In the bottom left image, problems with tethering the actin filaments are evident. The lower right image demonstrates actin bundling or intertwining of individual filaments, which was likely the most common problem with actin assays.

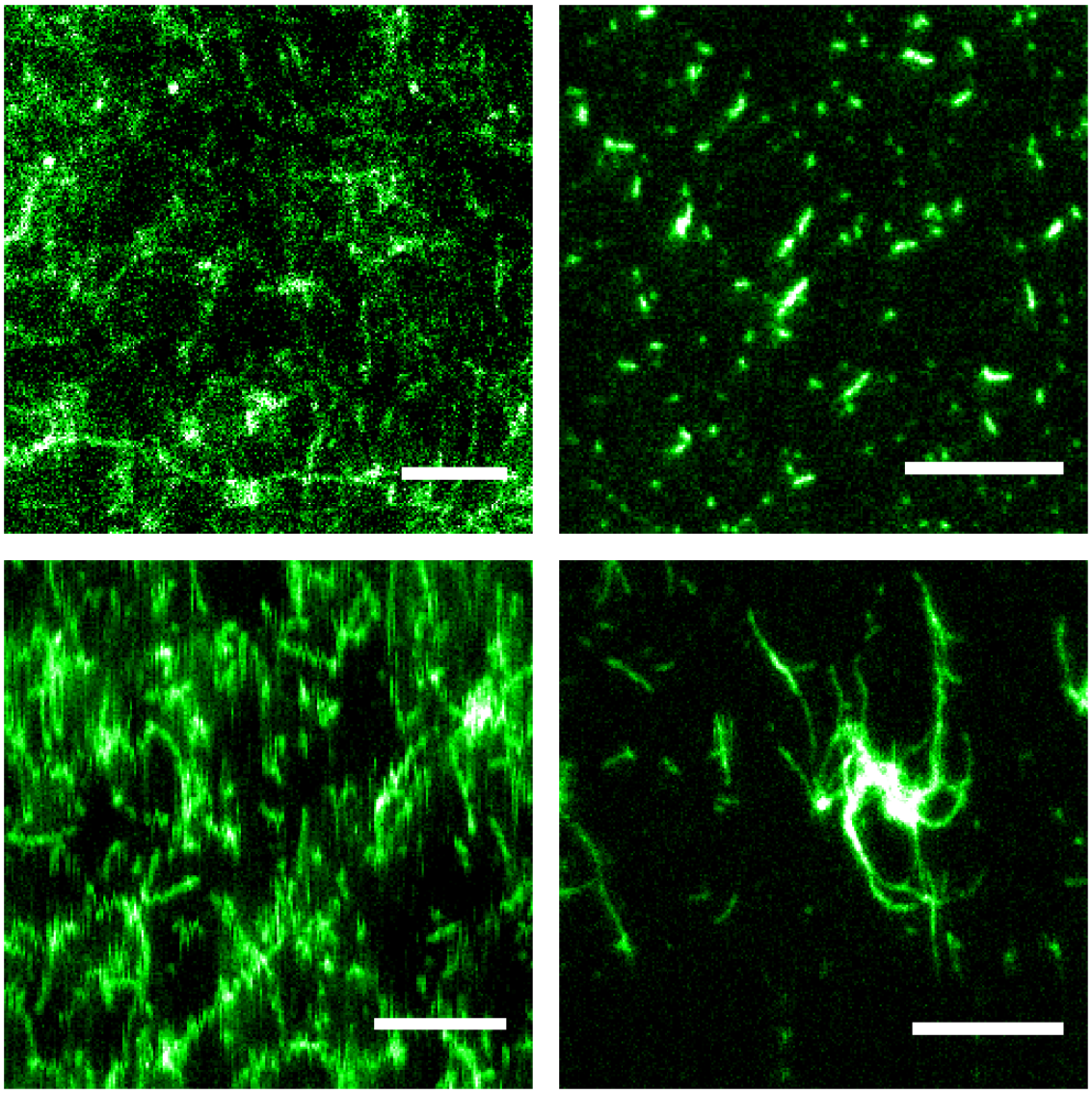

Figure 3.3: Images illustrating various problems with actin in assays. The top left image shows lack of proper labeling of actin filaments. The top right image shows actin that failed to properly polymerize. The bottom left image illustrates actin filaments that are too loosely bound to the substrate when attached through NEM myosin. The final image shows a bundling of actin filaments, which was a prominent issue in many assays.

3.3 Parked-Beam Method

The parked-beam method utilizes the detailed knowledge of the point spread function (PSF) of the laser light profile at the sample. Since myosin motors only process

along actin filaments, we initially imaged samples that were prepared with actin filaments tagged with Alexa Fluor® 488 as shown in Figure 3.4. We subsequently found a single location along an actin filament and halted the scanning stage so that only that location was being observed. The actin filaments were tethered to a glass coverslip while myosin motors tagged with quantum dots were free to process on filaments using available ATP in the assay. While the stage was "parked," any processive myosin motors on the actin filament would pass through the beam, thereby providing detailed information, both spatially and temporally, about the motor's motion.

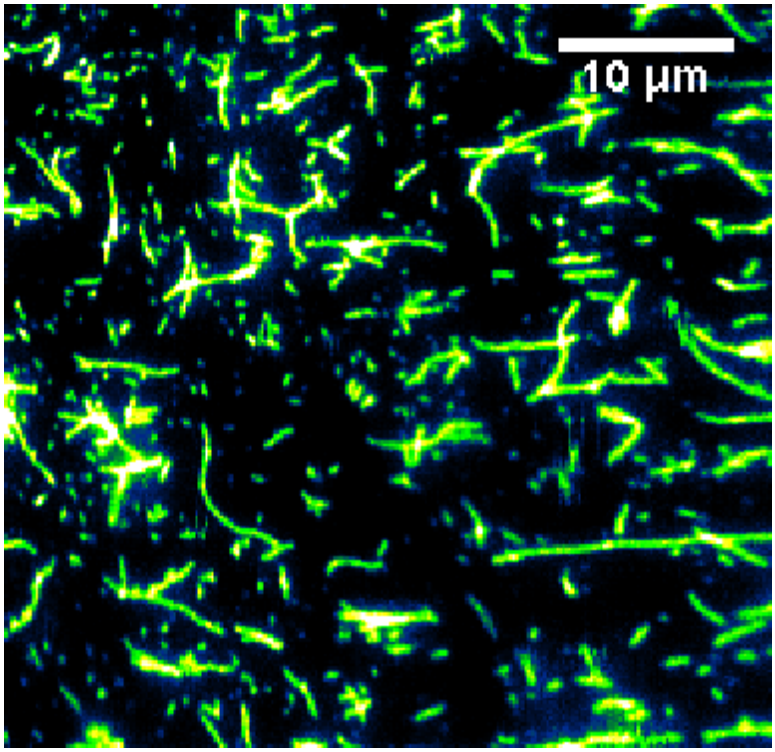

Figure 3.4: 45 x 45 µm image of actin filaments tagged with Alexa Fluor® 488. The concentration of actin is about 40 nM.

The parked-beam method is based on the fact that the PSF of the laser light at the sample can be fit precisely to a Bessel function. To make the fitting even simpler, an excellent approximation of the PSF is provided by a Gaussian function of the form:

$$f(x) = ae^{-\frac{(x-b)^2}{2c^2}} \tag{3.2}$$

where the term *c* gives a relative width of the PSF. Figure 3.5 shows a sample representation of a Gaussian fit to the scan of a single dot using Equation (3.2). The value *a* scales according to the intensity of the laser, where its value is equal to the maximum photon counts at the center of the PSF. In Figure 3.5, this is normalized to a value of 1. The value for *b* is dependent on the position of the beam along the surface of the sample along the *x* axis, which is equivalent to the fast-scanning axis of the stage in this case. Here, an arbitrarily value of 0.5 μm is assigned to *b*. Finally, the value of *c* scales according to the width of the Gaussian function. For the PSF shown in Figure 3.5, the value for *c* is 0.134 μm. The peak of the resulting function has a full-width half-maximum (FWHM) of 322 nm.

Using one channel of the microscope, actin filaments, nominally tagged with Alexa Fluor® 488 were imaged. The peak emission wavelength of Alexa Fluor® 488 is 519 nm, and therefore a 525/50 BPF was used in position 3 from Figure 2.1. Likewise, a 565/40 BPF was used in position 4 to capture emission of rhodamine 6G molecules with a peak emission of 556 nm. By stopping the scanner directly over a specific actin filament, the rhodamine channel could be continuously monitored. Any activity would indicate myosin motility along that filament.

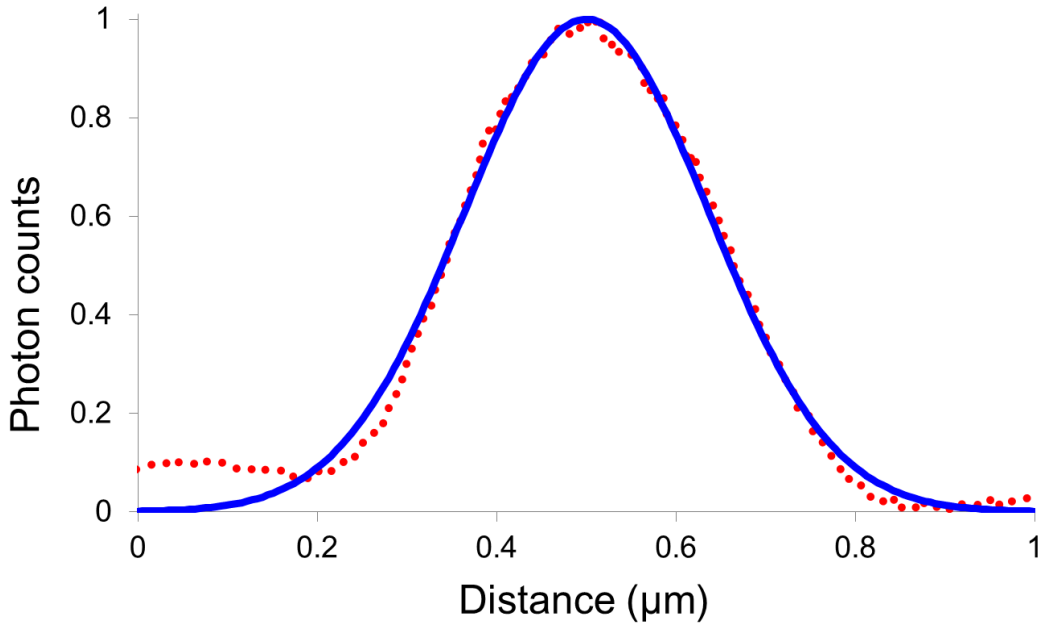

Figure 3.5: Gaussian representation of PSF (solid line) fit to line scan of a single molecule (dots). The Gaussian is a good approximation of the more exact fit of a Bessel function.

Any single molecule fluorophore that passed through the laser beam would follow the approximately Gaussian profile of the laser PSF. Accordingly, myosin motors tagged with single fluorophores could be tracked precisely as they traveled along actin. Even though the velocity of motor proteins is not constant, the relative brightness of the individual rhodamine molecule could be fit to the Gaussian function from Equation (3.1) and localized to within 2-3 nanometers. Using this methodology, we were able to track any motors moving along the actin filament with temporal resolution of 10 ms. The temporal resolution could be significantly improved by using a more stable and bright fluorescent marker, like quantum dots instead of a standard molecular probe like rhodamine 6G. After replacing the probe with quantum dots, it was expected that a temporal resolution of 100 μs or better could be achieved.

Detailed motion dynamics such as velocity, step size, and intrastep behavior could be ascertained from the data. Sample data is shown in Figure 3.6. The motor represented had an average velocity of 150 nm/s and an average step size of 34 nm, both of which are in very close agreement with the commonly accepted values for myosin V. Intrastep behavior could also be ascertained using the parked-beam method. One example is the short-lived backwards steps seen at 1050 ms and 1400 ms. At the time of these studies, the backwards stepping of myosin had predominantly been observed when a backwards force or load was applied to individual motors.[48,49] In fact, wild-type myosin Va, the particular protein used in our experiments, had not been observed to take backwards steps in absence of external strain. Although we were not thoroughly convinced, we advocated that the dotted arrows in Figure 3.6 indicate points at which the myosin V motor stepped backwards, even if only for several milliseconds at a time. Likewise, the solid arrow indicates a forward swinging motion of the motor before a full forward step was made.

An important note is that these results were not published due to the fact that additional evidence was unattainable at the time. Various problems with most assays, many of which were outlined earlier were nearly perpetual. The lack of a reliable myosin V tagging technique also prohibited further studies needed to verify the intrastep dynamics of wild-type myosin V. Although a peer-reviewed article was not published on the parked-beam work, it was presented at the Biophysical Conference in a platform talk in 2010. Most importantly, the work established a useful LSCM method for single motor protein tracking while greatly improving the temporal resolution of other popular tracking techniques. Because of this improvement, intrastep dynamics of any motor protein could be studied, even deep into the cytoplasm of living cells.

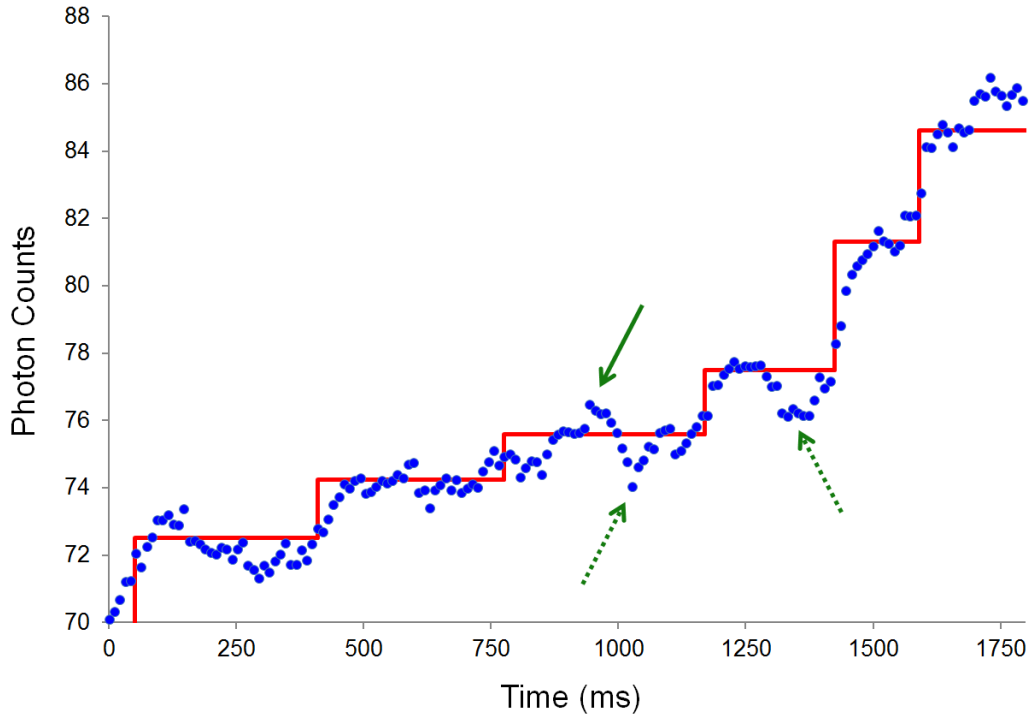

Figure 3.6: Parked-beam data for a single myosin V motor "stepping" through the beam. A Savitzky-Golay filter algorithm was applied to the data (dots) while the solid line trace was fit using a Gaussian function to model the PSF of our laser source beam.

3.4 Fast-Scanning Confocal Microcopy

In an effort to further establish LSCM as a practicable method for studying molecular motors, we developed FSCM. Nearly all molecular motors follow a specific path, namely along a cytoskeletal filament. Therefore, it is feasible to scan continuously along a single filament, provided it is oriented along one of the scanning axes of the microscope stage. By using the fast-scanning axis of the stage and focusing on filaments oriented along it, we were able to indefinitely observe all dynamics on that filament. Although restricted to a single dimension, spatially and temporally detailed information could be gathered using this method. Since an entire filament was imaged, instead of a single spot as in the parked-beam method, data from more motors could be collected in a

given amount of time. The primary tradeoff of utilizing FSCM over the parked-beam method was the loss of temporal resolution.

An image generated by FSCM is shown in Figure 3.7 where the vertical axis is scanned 512 times along an actin filament. Therefore, the horizontal axis of the image shows the location of each fluororescent marker with respect to time. There are four notable "lines," which appear slanted in the image. Each slanted line represents a processive myosin motor. They are each indicated by labeled arrows in Figure 3.7. The velocity of each motor can be calculated for each of the line traces. The processivity, or distance traveled along the filament, could also be found for each of the motors represented. Although step sizes could theoretically be determined, the majority of our experiments were optimized for velocity and processivity measurements, given the superiority of the parked-beam method in measuring step sizes.

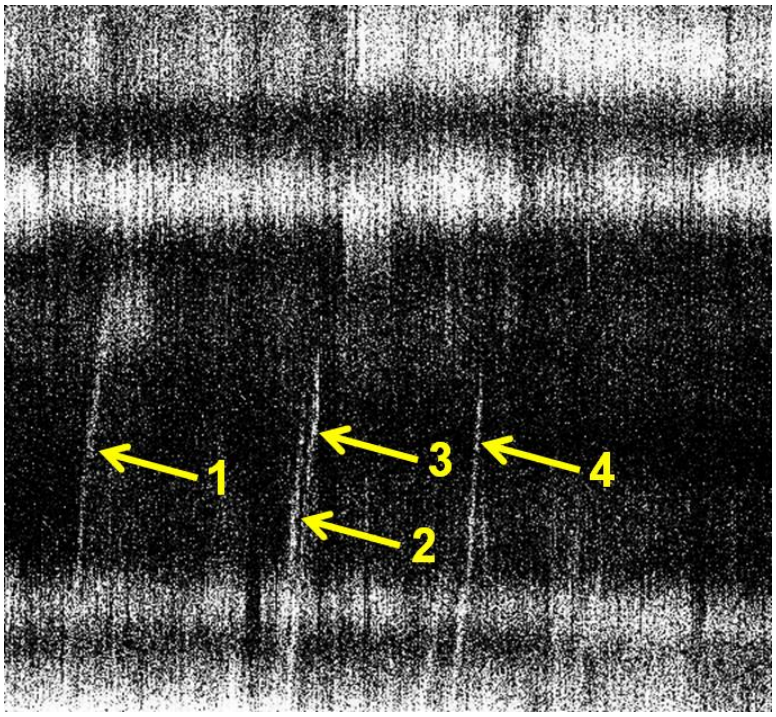

Figure 3.7: Sample image taken using FSCM. There are at least four mostly non-motile motors in the image, represented by the two static traces at the top and bottom of the image. There are also at least three active, motile myosin V motors that processed along the observed actin filament while the image was taken.

Individual line traces were extracted from data represented Figure 3.7 and are shown in Figure 3.8. Eight consecutive lines detail the position of an invidual myosin V motor as it processes along the observed filament. A 200 ms temporal resolution was used to optimize signal and thus more accurately ascertain processivity and average velocity information. Positions at each time interval were determined by fitting the signal peak to a Gaussian function, similar to that demonstrated earlier for the parked-beam method. The motor represented in Figure 3.8 has an average velocity of 746 ± 265 nm/s and a processivity of 1.43 μm. Although the velocity is significantly higher than for the parked-beam experiment, it is appropriately scaled according to the ATP concentration, now at 200 μM. A value of approximately 500 nm/s is expected[47] when the

concentration of ATP is near saturation of the myosin active sites. The saturation limit for this strain of myosin V is an ATP concentration of approximately 1 mM.[50]

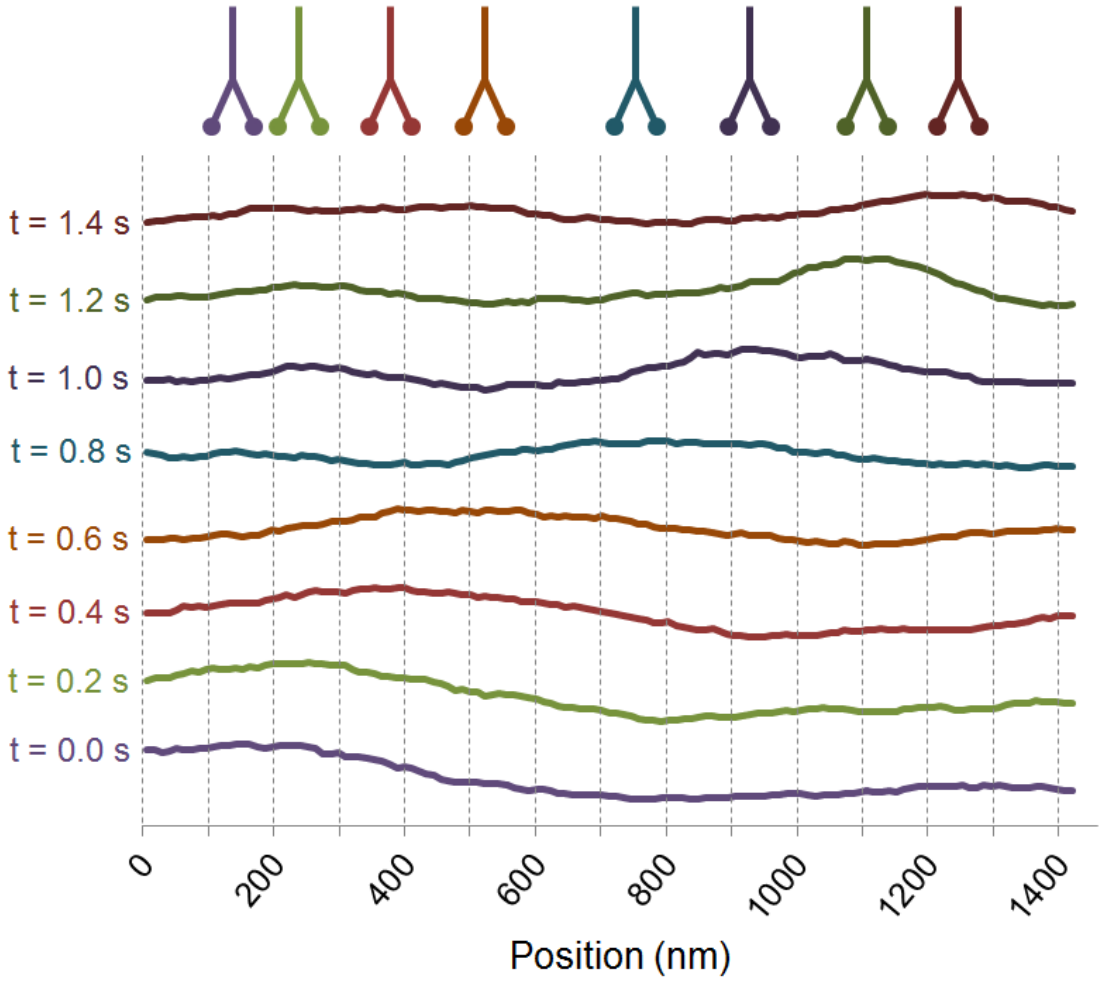

Figure 3.8: Position of a single myosin V motor at 200 ms intervals. The drawings at the top of the figure correspond to the motors position and are drawn close to scale relative to the x-axis of the figure.

The conditions for each of these assays had an ATP concentration near the saturation limit, considerably more than the ATP concentration for the parked-beam experiments. The mean velocity of 15 motors, similar to the one shown in Figure 3.8, was found to be 430 ± 152 nm/s. This is very near the upper limit of mean velocities

observed by other prominent groups under similar assay conditions, most importantly the concentration of ATP.[47,48,50] The mean processivity of 15 motors was also determined by FSCM to be 1.22 ± 0.59 μm. Once again, this value wholly agrees with the reported standard processivity for myosin V.[41,47,51]

LSCM is well known for its capability to produce three dimensional images. One example is shown as a two color image of actin and myosin in Figure 3.9. This is a simple example of the ability of LSCM to provide three dimensional images of even larger entities, such as living cells. In such cases, both the parked-beam method and FSCM could also be used once a three dimensional cellular map is established. This is in contrast to a technique like TIRF, which would be limited for *in vivo* studies. Since most living cells have thicknesses greater than 200 nm, *in vivo* studies would benefit greatly from either of the LSCM methods.

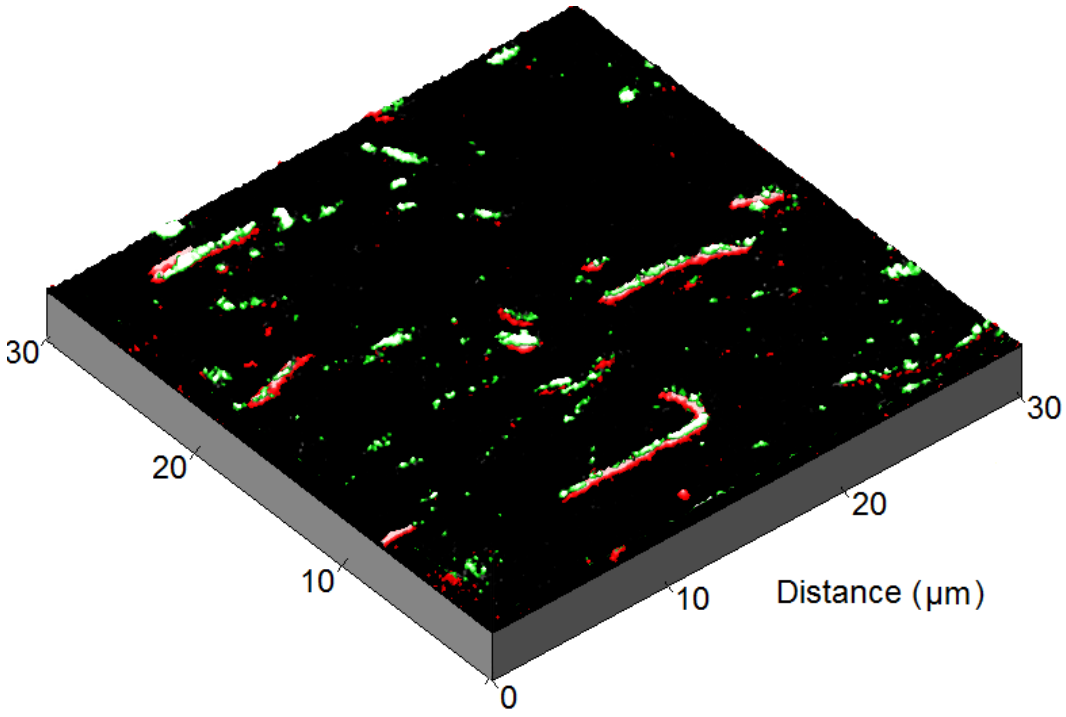

Figure 3.9: Sample three dimensional, two-color image of actin and myosin. Actin filaments (red/white) are tagged with rhodamine 6G and myosin V (green) is tagged with green fluorescent protein.

3.5 Cellular Intermediary Nanostructures

In order to demonstrate the application of both methods *in vivo*, we patterned metal nanostructures, which were meant to emulate the cytoskeletal structure of cells' interiors. An SEM image of the nanostructures is shown in Figure 3.10. With spacing of 2 μm and a height of 200 nm, the gold nanobars were optimized for suspending actin filaments. Using either of the LSCM methods we developed, molecular motor dynamics could be observed in an environment more accurately representative of intracellular actin networks.

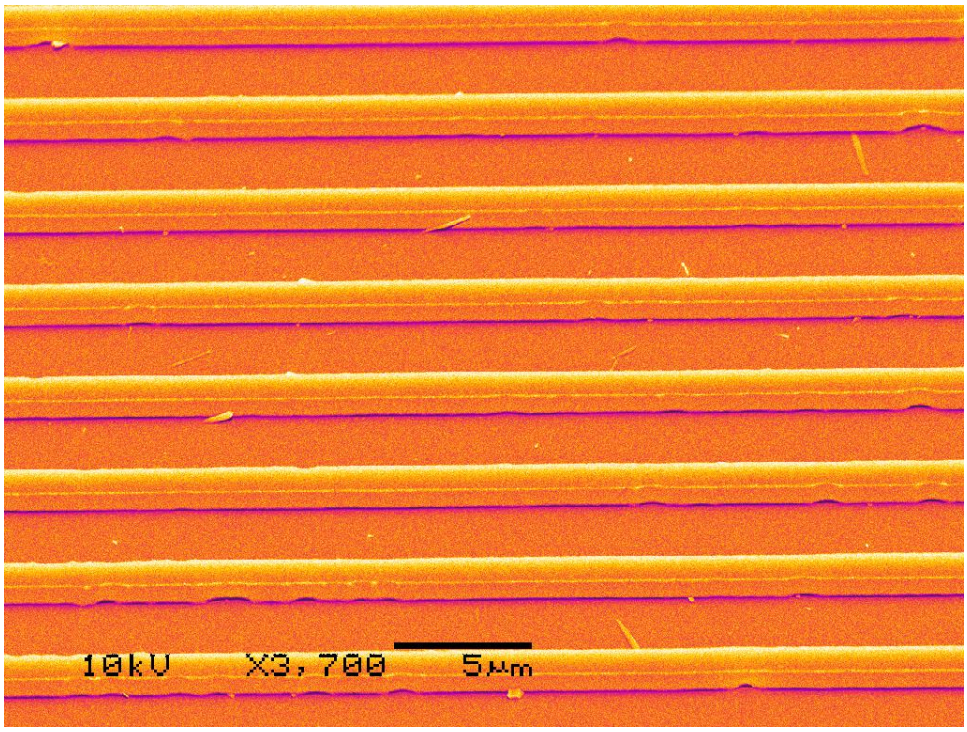

Figure 3.10: SEM image of gold nanostructure pattern. Used in motor protein assays for suspension of actin filaments to emulate a cytoskeletal structure.

Various assays were constructed using the patterned nanostructures shown in Figure 3.10. An assay very similar to the one outlined by Table 3.1 was used to attached the actin filaments directly to the metal nanobars. By positioning the nanobars perpendicular to the direction of flow in the assay chamber, multiple actin filaments were expected to align themselves across the ridges since they readily aligned themselves with the flow of the injections. This would thereby provide 2 μm actin segments over which motor proteins could process without obstruction by the coverslip or any stray protein fragments bound to the coverslip. A sample assay is pictured in Figure 3.11 where multiple actin filaments are aligned vertically in the image. Though most seem to be actin bundles, two single actin filaments, which are suspended firmly across the nanobars, are indicated by two white arrows.

Motor proteins behave slightly differently in cells compared to *in vitro* experiments, with a primary example being the velocity of myosin V. *In vivo* studies suggest that its velocity approaches 1 μm/s, which is over twice the standard mean velocity consistently reported for *in vitro* studies.[52,53] Since all of the reasons for the velocity discrepancy between *in vivo* and *in vitro* molecular motors are not precisely known, an assay utilizing nanostructures similar to our construct could provide more insight into explaining the inconsistencies among motor proteins in different environments. The suspension of actin filaments permits a more natural motion path for molecular motors since they are not hindered by the presence of a substrate on one side of the filaments. Due to problems similar to those encountered in the parked-beam studies, we were unable to ascertain specific motion dynamics of myosin V. However, the ability to adapt assays to incorporate nanostructures with vertically aligned and suspended filaments showed that FSCM, parked-beam, and other methods could be used to probe the movement of motors in an environment analogous to the cytoskeleton. Coincident with our fabrication of the nanosctructures and demonstration of actin suspension, prominent research on myosin X was published using a very similar structure made of poly(methyl methacrylate), or PMMA, in place of the metal nanobars.[54] However, using metal nanobars may prove superior due to the robust mechanical properties of gold in comparison to PMMA.

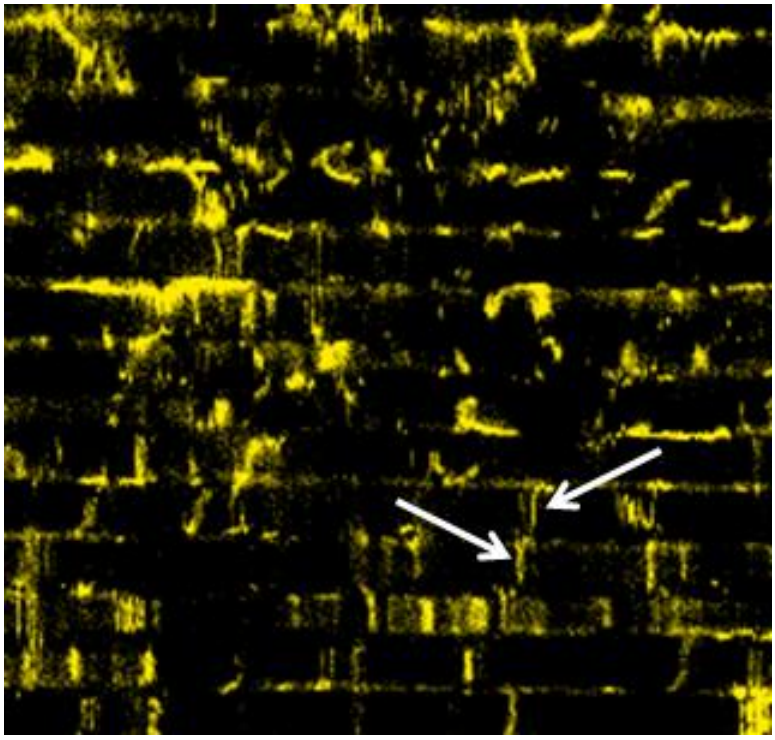

Figure 3.11: Fluorescence image of actin filaments suspended across nanobars. The area represented is 45 × 45 μm with actin tagged with Alexa Fluor® 488 flowed across multiple nanobars (horizontal). Actin filaments are supended in the vertical direction.

3.6 Conclusion

This work revealed two suitable LSCM techniques for use in studies of individual motor protein motion dynamics. The use of either technique can realistically translate to *in vivo* investigations of molecular motors, since confocal microscopy is a proficient tool for intracellular probing due to a sizeable imaging depth and superior optical resolution compared to wide-field microscopy. Both techniques require no alterations to most LSCM configurations since collected data is post processed according to the technique to provide the most useful data. Accordingly, the techniques can be used as compliments to one another or any other work that is done on a single sample.

The parked-beam method revealed potential intrastep dynamics of myosin V, due to superior temporal resolution, which can still be improved significantly in future work

by using biological markers with higher stability and stronger emission. Although non-stepping forward swinging motion of a detached head had been observed in myosin V before, backwards steps in the wild-type variant of myosin V had not been previously witnessed. However, the parked-beam experiments strongly suggest occasional backwards stepping while confirming the forward non-stepping activity of a head of the motor.

FSCM proved to be a viable technique for determining velocity, processivity, and step sizes of molecular motors. All characteristics of myosin V ascertained in the FSCM experiments were in agreement with previously published results. Utilization of both FSCM and the parked-beam method in extended applications of LSCM, such as three dimensional imaging or deep intracellular probing, are possible avenues for future work on nearly any motor protein. Mapping full motor protein dynamics, including highly resolved temporal events, throughout the entire breadth of the cytoskeleton of a cell could be realized by application of these techniques in cells with realiably tagged molecular motors.

CHAPTER 4: BLINKING CORRELATION

Amidst the study of myosin using FSCM, a fascinating phenomenon was encountered. One unfortunate consequence of working with biological motor proteins is that they do not always function properly. As evidenced in Figure 3.7, there are at least four immobile myosin motor proteins for which the quantum dot position does not change throughout the image. Nearly every observed actin filament had some of these "stuck" motors. When the stuck motors were nearby one another, generally within 1 μm, it appeared that the quantum dot blinking behavior on each motor was related to its neighbor. When one of the dots blinked off, it appeared that the neighboring dot would blink off more often than random blinking fluctuations would dictate. Therefore, we took the initiative to study the blinking in dot pairs analytically to determine if a quantifiable correlation in blinking existed.

Before conducting a controlled experiment specifically examining the blinking relationship between neighboring quantum dots, the rationalization was that actin filaments were facilitating charge propagation. Charge propagation along filaments was not a new phenomenon[55] and all of the FSCM experiments to this point had been conducted along filaments. However, control experiments in the absence of actin filaments, outlined in the following sections, proved that conductivity along filaments was not sufficient to explain the findings in blinking correlation.

4.1 Preparation of Samples and Experimental Methods

In order to investigate the alleged blinking correlation, thin film samples of commercial CdSe/ZnS core-shell quantum dots were prepared. Quantum dot concentrations ranging from 1×10^{-11} to 8×10^{-10} M, were dissolved in a solution of ~0.5% PMMA in a base solvent of 98.6% purity toluene. Samples were prepared by spin coating about 25 μL of the solution onto a 25 × 25 glass coverslip using a spin rate of 1500 rpm for 30 seconds. This resulted in a sample comparable to the one imaged in Figure 4.1, where the average distance between individual quantum dots is ~3 μm. This distribution assured that some neighboring quantum dots would be separated by less than 1 μm, which is the approximate distance at which blinking correlations had been observed in our myosin experiments. Laser excitation intensity was approximately 7 $kW \cdot cm^{-2}$ for all of the experiments discussed in this chapter.

FSCM was employed to cover a distance of 3 μm with two neighboring dots captured within that distance. An image such as the one shown in Figure 4.2 was generated for each of the dot pairs with an average scan speed of 10 lines per second. The image resolution was set to 512 pixels by 512 pixels. Therefore, for each image, the behavior of each dot could be compared at 512 different points during the full scan time of approximately 51.2 seconds. Data was only analyzed when both quantum dots displayed blinking behavior for at least 50% percent of the image scan. If one or both of the quantum dots occupied a permanent or semi-permanent non-emissive state continuously for half of the scan length or more, the data for that particular image was not used in the final analysis.

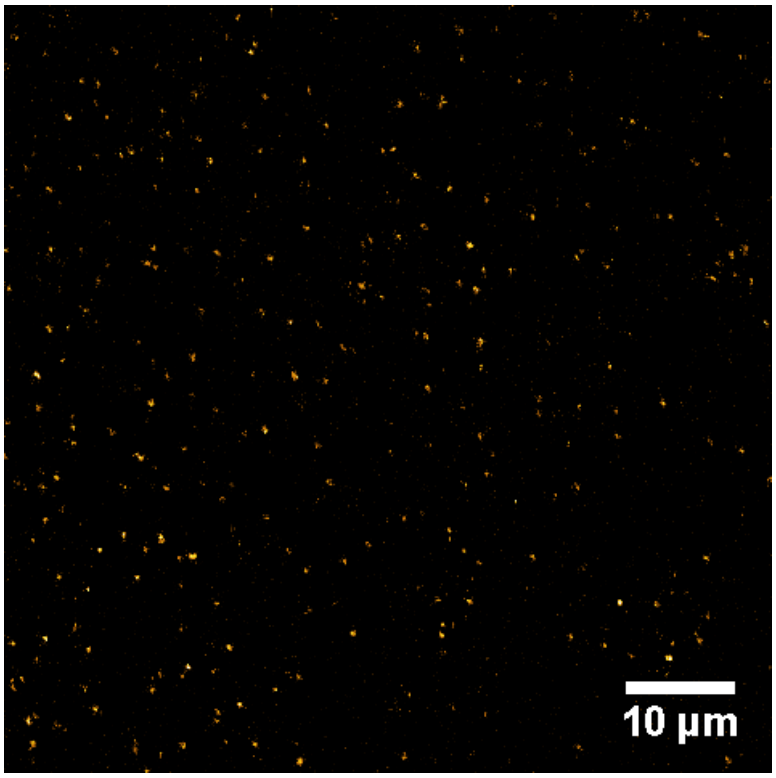

Figure 4.1: 70 × 70 µm image of single quantum dots. The distance separating individual nanocrystals is approximately 3 µm on average.

4.2 Blinking Correlation Results

Initially, an analysis of over 60 dot pairs was conducted. For each image, such as the one in Figure 4.2, the average brightness of each dot was taken from only the center section of the dot. This was done by analyzing only the central 10 pixels of each dot across the image. If the width of a dot encompassed 100 pixels, which is approximately 580 nm based on a 3µm scan range, then only the central 10% of that dot was analyzed for the purpose of determining an on or off state. The reason that only the center of the quantum dot was chosen for analysis was to most discretely determine the blinking behavior since the brightness of the image scales according to the PSF. The center of the quantum dot will display the greatest disparity in brightness and therefore offer the best indication of blinking behavior.

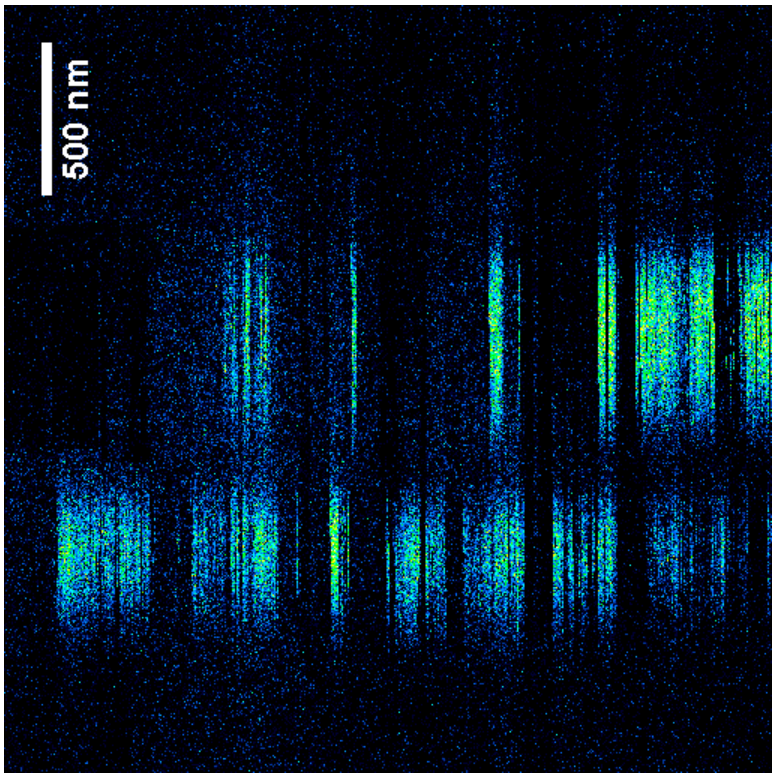

Figure 4.2: A quantum dot pair imaged using FSCM. The horizontal axis has no spatial width but instead represents a total time of 51.2 seconds. There are 512 vertical lines in the image and the on or off status of each dot can be compared to its neighbor for each line.

The brightness of the quantum dot was averaged for 10 pixels near the center of the respective quantum dot at each of the 512 points across the image. For each line with photon counts less than the average photon counts across the image, the quantum dot was assigned as being in an off state. Likewise, for each line with photon counts greater than the average, the quantum dot was assigned as being in an on or emissive state. The on or off values were then compared to the values for the other dot for each line across the image. When the two quantum dots were both on or both off, they were considered to be correlated and when they had opposite values, they were anti-correlated.

Given that the most well understand energy transfer mechanism between two individual quantum dots, namely Förster resonance energy transfer (FRET), is only

functional at distances up to 10 nm,[56] correlated blinking between two quantum dots at distances of hundreds of nanometers was completely unexpected. Therefore, if each quantum dot in a neighboring pair exists in an on state approximately 50% of the time, it would be expected that the blinking between both quantum dots would be correlated as often as it is anti-correlated. Interestingly, analysis of the blinking data showed a positive blinking correlation between neighboring quantum dots.

In order to statistically determine the degree of blinking correlation, the Pearson product-moment correlation coefficient (PPMCC) was employed. It can be calculated using Equation (3.3).

$$\text{PPMCC} = \frac{\sum(x_i - \bar{x})(y_i - \bar{y})}{\sqrt{\sum(x_i - \bar{x})^2 \sum(y_i - \bar{y})^2}} \tag{3.3}$$

The PPMCC was evaluated by assigning non-emissive (off) states as "0" and emissive (on) states as "1". A perfect correlation would correspond to a PPMCC value of 1. This would only result from neighboring dots being in the same state, either on or off, at all 512 points across an image. Likewise, perfect anti-correlation would correspond to a PPMCC value of -1, which would occur if the neighboring dots were in opposite states at all 512 points across the image. Therefore, if no correlation existed, a PPMCC value of 0 should be obtained. The MATLAB routine for finding the PPMCC values and their respective uncertainties is shown in Appendix A.

The distance between neighboring quantum dots for each pair analyzed was also calculated. This was done using the raw image data provided by FSCM. In an image such as the one shown in Figure 4.2, an image array of 512 × 512 numbers is available, with each number indicating the number of photons received at that point in the image. By summing horizontally across the image, a curve like the one shown in Figure 4.3 can

be generated and subsequently fit to a multi-Gaussian formula as shown. The peak values of the Gaussian fits can then be used to deduce the distance between the respective quantum dots.

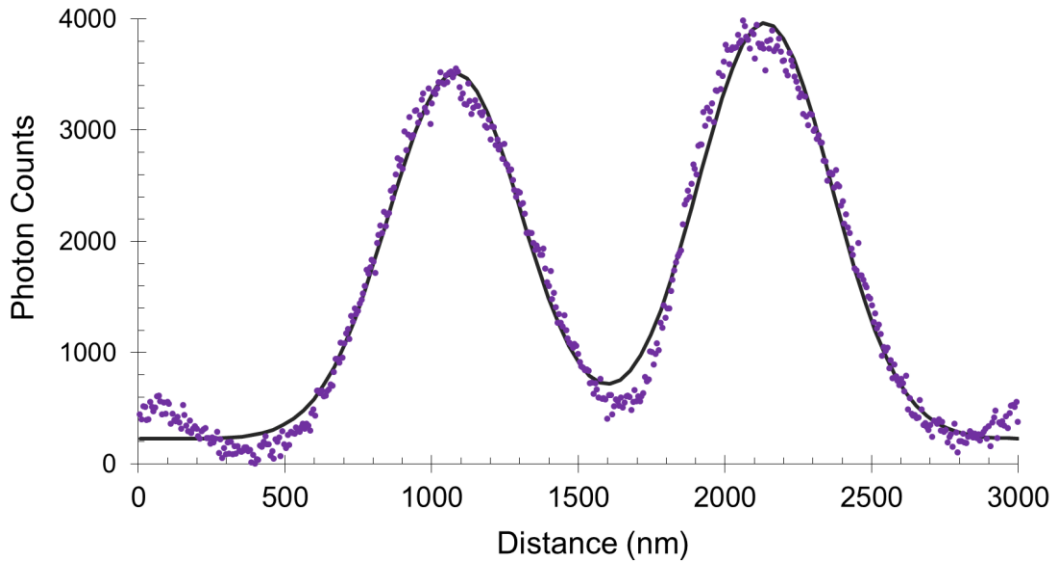

Figure 4.3: Sum of photon counts across an FSCM image. The two neighboring quantum dots are separated by a distance of 1.05 μm. The dark solid line is a two-Gaussian function fit to the data.

Results from the analysis of an initial study of 60 quantum dot pairs are summarized in Figure 4.4. Three different quantum dot sizes were used in the study, all of which were commercially distributed by Evident Technologies. The variety of quantum dots used include a set that emit with peak wavelengths (λ_{em}) of 556 nm, another that emits at 596 nm, and a third that emits at 617 nm. No significant difference in average blinking correlation was found between the different quantum dot sizes. Therefore, all data points were fit to an inverse distance (r) function, which was chosen since it offered the best fit among simple fitting parameters. In addition, the PPMCC was

noted to scale inversely with distance between quantum dots, further supporting the use of an inverse distance fit to the data.

Error bars shown in Figure 4.4 were calculated in two different ways, depending on the reference axis. The horizontal error bars were scaled to the quality of a standard Gaussian fit to each quantum dot's location, specifically ± one standard deviation in distance. The vertical error bars were tabulated by propagating the error from shot noise and the chosen threshold with a large population (~1000) of blinking traces normalized to the original data. The standard deviation of the PPMCC values from the newly created population was taken and reported as the error.

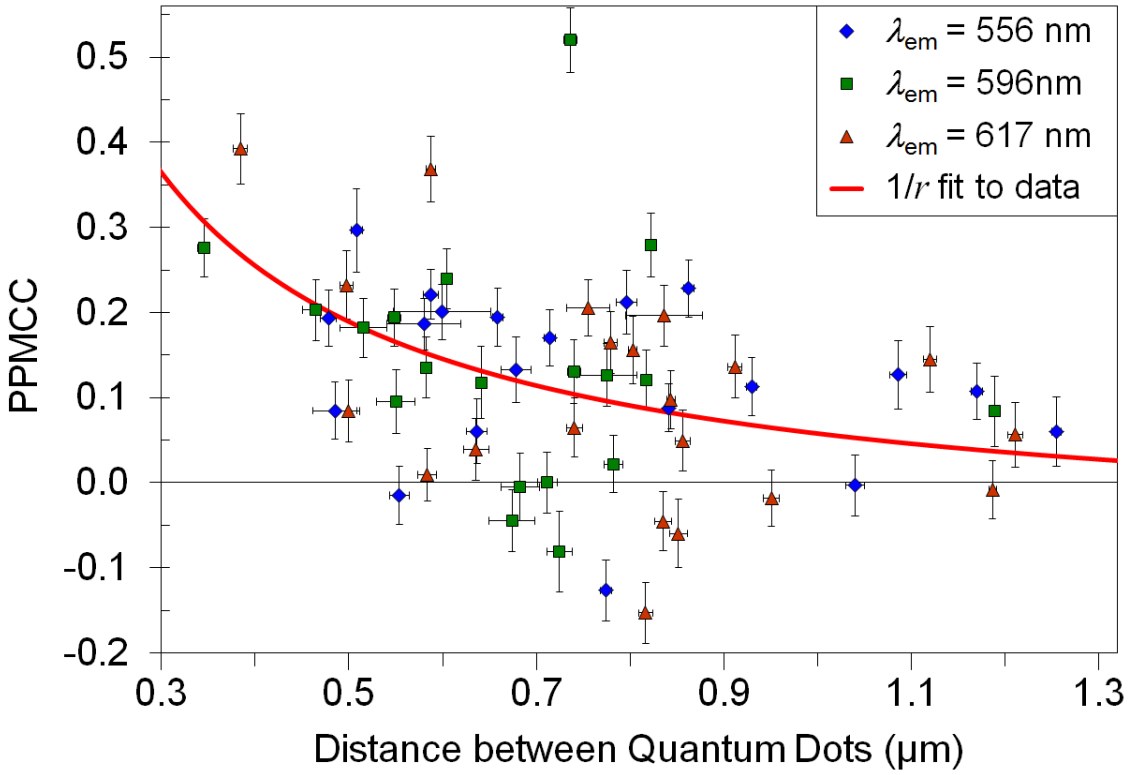

Figure 4.4: The PPMCC of about 60 individual quantum dot pairs. A subpopulation of three different sizes of quantum dots are plotted versus separation distance. The dotted line is a best fit to all data using an inverse distance relationship. All data in this plot was taken at scan speeds of 10 lines per second and with a resolution of 512 lines per image. Horizontal and vertical error bars are shown but are sometimes obscured by the local data point.

The PPMCC would be artificially inflated in situations where quantum dots spend more time in an emissive (or non-emissive) state. Therefore, the average PPMCC was calculated based on randomly pairing the blinking pattern of a single quantum dot to another single quantum dot from a different pair. The PPMCC was found to have an average value of 0.0223 over the course of 60 random pairings. The value was slightly higher than 0 due to the fact that dots spent slightly more time in an emissive state versus being in a non-emissive state. Despite considering a slightly inflated PPMCC across all 60 quantum dot pairs, only 14 of them fell below the random correlation value of 0.0223.

At distances of less than 600 nm, an unmistakable correlation exists, particularly because only one of the nineteen quantum dot pairs displayed anti-correlated blinking. However, at further distances, several of the pairs' blinking was anti-correlated. Heterogeneities in individual quantum dots and variations in the PMMA matrix throughout the sample are to be expected. Consequently, it is not unreasonable that a substantial portion of the quantum dot population would behave erratically due to these localized variations. Moreover, the excited state dynamics and charging behavior of individual quantum dots are known to fluctuate significantly among different individual quantum dots.[57] Nevertheless, the overall trend in blinking correlation suggests that neighboring dots, generally at distances of less than one micrometer, exhibit some type of interaction mechanism.

To verify that the PPMCC values were not partially influenced by an inherent instrument artifact or imaging software anomaly, a cross correlation was done on several of the data series represented in Figure 4.4. The lag was stepped by 1 line in both directions for nine of the data sets with the highest correlations. Each cross correlated array was also appended on both sides with a transposed copy of itself to account for the bias to zero in a standard cross correlation. The results are summarized by Figure 4.5. Individual pairs of quantum dots are represented by gray traces and the overall cross correlation is shown as a dark blue line. No recurring patterns are evident and nearly every data set peaks at a lag of zero. Two of the data series have substantial peaks at non-zero lag points, which is expected for pairs with relatively long periods of remaining in an on or off state. This is characteristic of both quantum dot pairs with less than optimal cross correlation peaks. In one case, a quantum dot was emissive for nearly 20

seconds while the neighboring quantum dot was emissive for 10 seconds during the same timeframe. For the rest of the quantum dot pairs, the blinking is more rapid, thereby producing the expected cross correlation functions.

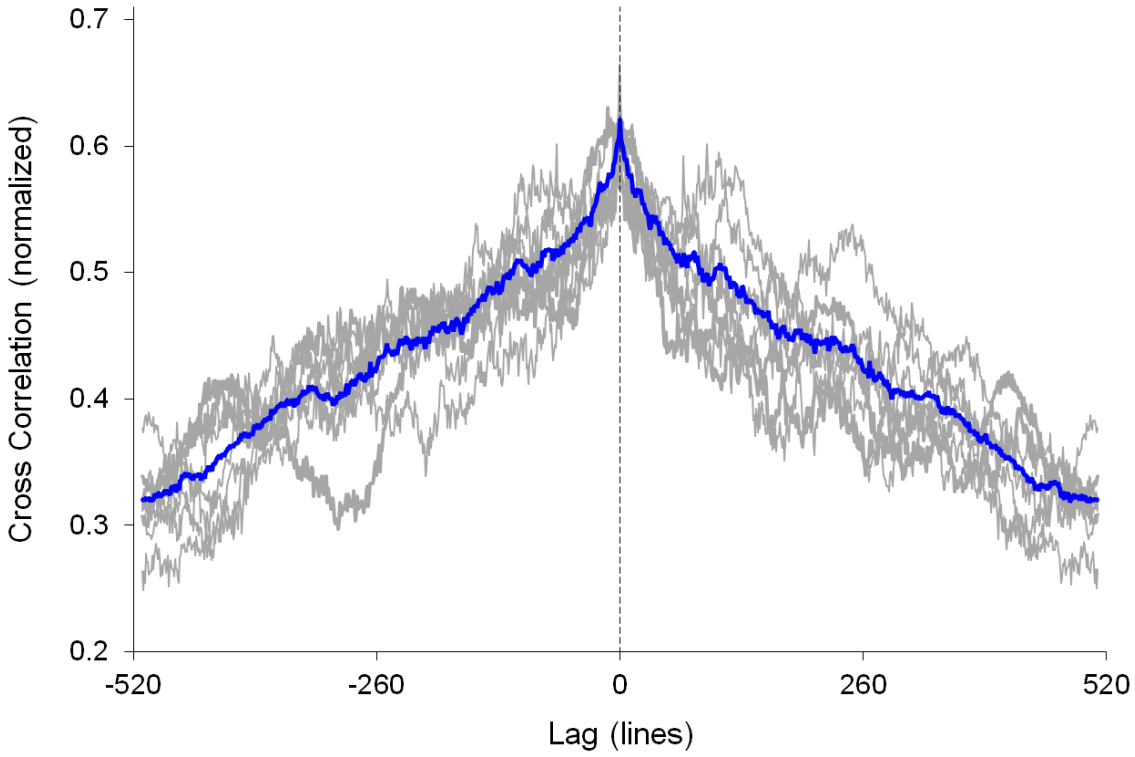

Figure 4.5: Cross correlation of blinking patterns between nine quantum dot pairs. The correlation lag covers all 512 lines in both directions. All nine pairs are represented by gray traces while their average is shown by the solid blue line.

4.3 Fluorescence Overlap and Two Channel Imaging

A primary concern regarding the initial blinking correlation studies was the width of the PSF, which is evident in Figure 4.3. If the PSF overlap was significant enough, the fluorescence from one quantum dot could perhaps influence the calculated state of the neighboring quantum dot. Hence the PPMCC would be inflated due to fluorescence overlap. In order to address this potential issue, an analysis of the overlap and a separate

two channel imaging study were both conducted. Both approaches demonstrated that the PPMCC values were not significantly influenced by fluorescence overlap between neighboring quantum dots.

The overlap of a pair of quantum dots separated by a distance of 465 ± 6 nm, which is the third closest pair shown in Figure 4.4, was analyzed. First, the image data for the pair was summed using the same method used to generate Figure 4.3. The result is plotted in Figure 4.6 represented by the solid circle markers. The summed data was fit to two Gaussian functions, signified by the dashed lines, while the sum of the two Gaussian functions is shown as a solid line. Only 10 out of 512 pixels were used to determine the state of each quantum dot for each line scan. The 10 pixels were chosen using the peak pixel location of the summed data and the nearest 9 pixels that were also furthest from the neighboring dot. In Figure 4.6, the chosen pixels are represented by a lightly shaded area beneath the respective summed peaks. The entire overlap between the two quantum dots is shaded by a grid pattern. The amount of overlap that actually influences the determination of an on or off state is shown by the darkly shaded gray wedges.

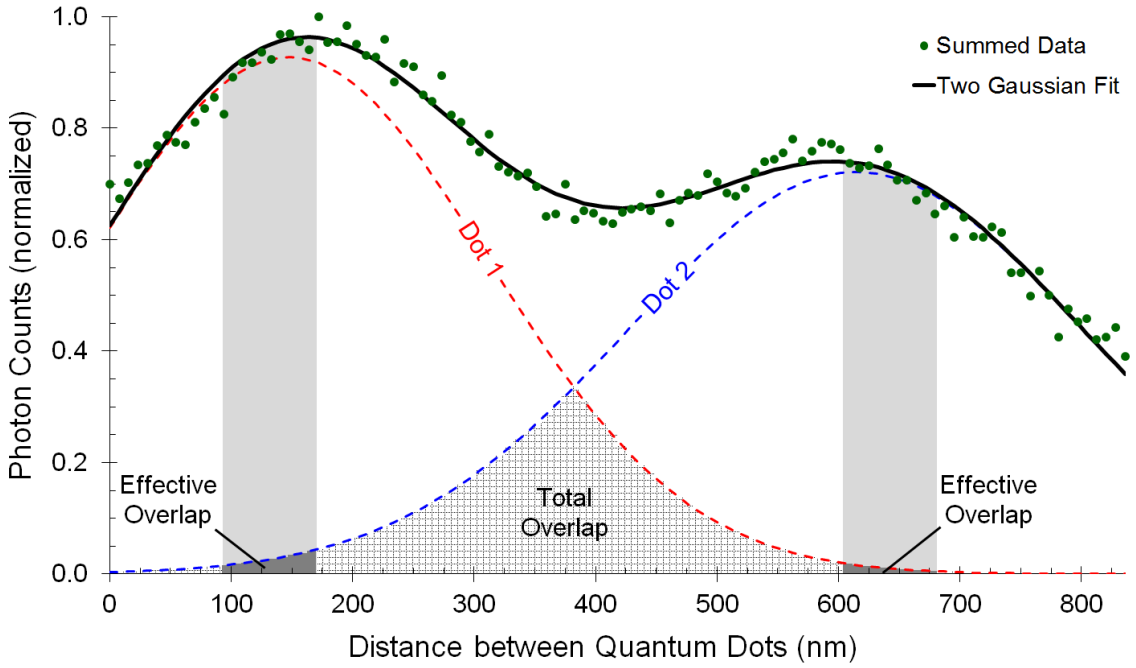

Figure 4.6: Effective overlap for two quantum dots separated by ~465 nm. Data for the two dots was fit to a two Gaussian function, with the individual contributions (a single Gaussian) for each of the two quantum dots represented by dotted lines. The lightly shaded area beneath each of the two main peaks highlights the specific series of photon counts used in the analysis of blinking behavior.

The overlap, Ov_1, of the PSF from 'Dot 2' into the analyzed portion of 'Dot 1' was determined by integrating the effective overlap region beneath Dot 1. Equation (3.4) states the integral used to determine the area in Ov_1, which is approximately 1.851 nm·counts.

$$Ov_1 = \int_{93.75}^{164.06} 0.7212e^{-\frac{(x-614.22)^2}{2(187.68)^2}}dx \tag{3.4}$$

The overlap, Ov_2, was determined similarly using Equation (3.5) and roughly equates to 0.7204 nm·counts:

$$Ov_2 = \int_{609.38}^{679.69} 0.9274e^{-\frac{(x-147.13)^2}{2(164.60)^2}}dx \tag{3.5}$$

where separately dividing both Ov_1 and Ov_2 by the total analyzed area underneath their respective peaks, the percent overlap was determined. The fit, a two Gaussian function, was integrated over the same distance as shown in Equations (3.4) and (3.5). Equation (3.6) displays the integral used to find the respective areas, A_x, which were used in the blinking analysis of each quantum dot.

$$A_x = \int \left(0.7212e^{-\frac{(x-614.22)^2}{2(187.68)^2}} + 0.9274e^{-\frac{(x-147.13)^2}{2(164.60)^2}} \right) dx \qquad (3.6)$$

Since the analyzed area beneath Dot 1 is approximately 66.189 nm·photon, the contribution from the PSF overlap from Dot 2 is 2.80%. Likewise, the analyzed area beneath Dot 2 is about 50.492 nm·photon. The effective PSF overlap from Dot 1 is therefore 1.42%. The average photon counts used to analyze the state of each quantum dot, which is the sum of the counts across the ten chosen pixels for each line, was approximately 160 counts. On average, the overlap thus corresponds to an additional 4 to 5 photon counts if Ov_1 is used as an example. The overlap of two more quantum dot pairs, which were separated by approximately 500 nm, were analyzed and showed very similar overlap percentages.

From the dataset of 60 pairs represented by Figure 4.4, it was determined that the quantum dots spent on average 56% of the time in an emissive state. Based on this, a randomly generated blinking pattern for a hypothetical quantum dot and its neighbor were compared by generating 1000 hypothetical pairs. In addition, respective overlaps of 5.5% and 1.3% were assumed for all of the hypothetical pairs due to the fact that those overlap percentages were the highest found among the calculated overlaps. Even with the maximum overlaps, the average PPMCC was only about 0.035 for the entire random set. This value is significantly less than the average correlations noted in Figure 4.4,

which is a PPMCC approximately equal to 0.20. In addition, the PPMCC of 0.035 is only indicative of the contribution of the PSF for quantum dot pairs that are closer than 500 nm. Many of the pairs studied were separated by distances over more than 500 nm where a significant correlation can still be observed. Therefore, the overall contribution from PSF overlap between quantum dot pairs was deemed to be negligible.

To experimentally show the insignificance of the PSF overlap, another set of studies were conducted utilizing the two channel imaging capability of the LSCM system. First, a 585 nm dichroic mirror was placed in the DBS_2 slot from Figure 2.1. Then, a sample was prepared as outlined previously, except an equal amount of two different sizes of quantum dots, those with emission of 556 nm and those with emission of 617 nm, were spin coated in the PMMA layer. Emitted light below 585 nm was primarily detected by the one APD, while all emitted light above 585 nm was detected by another APD, thereby enabling the imaging of two different sizes of quantum dots during the experiment. To conduct FSCM, a quantum dot of one size was found vertically aligned with a neighboring quantum dot of the other respective size. Examples of the images produced by this technique are shown in Figure 4.7 where the higher wavelength emission can be seen on the left (orange) and the lower wavelength emission is on the right side (green).

The most obvious benefit to this technique is the complete elimination of potential overlap having an effect on the blinking correlation results. As indicated by Figure 4.7, emission from neither of the quantum dots is present in the opposing image. This was also beneficial to study quantum dots at distances closer than possible in the single channel studies. For example, the quantum dots shown in Figure 4.7 are separated by

352 nm. Pairs separated by comparable distances in the single channel studies suffered from overlaps of 5.5% and 1.3%, which corresponded to the PPMCC being inflated by 0.035, as detailed previously. However, the individual blinking behavior of quantum dots with practically zero separation distance could still be studied using a two channel configuration.

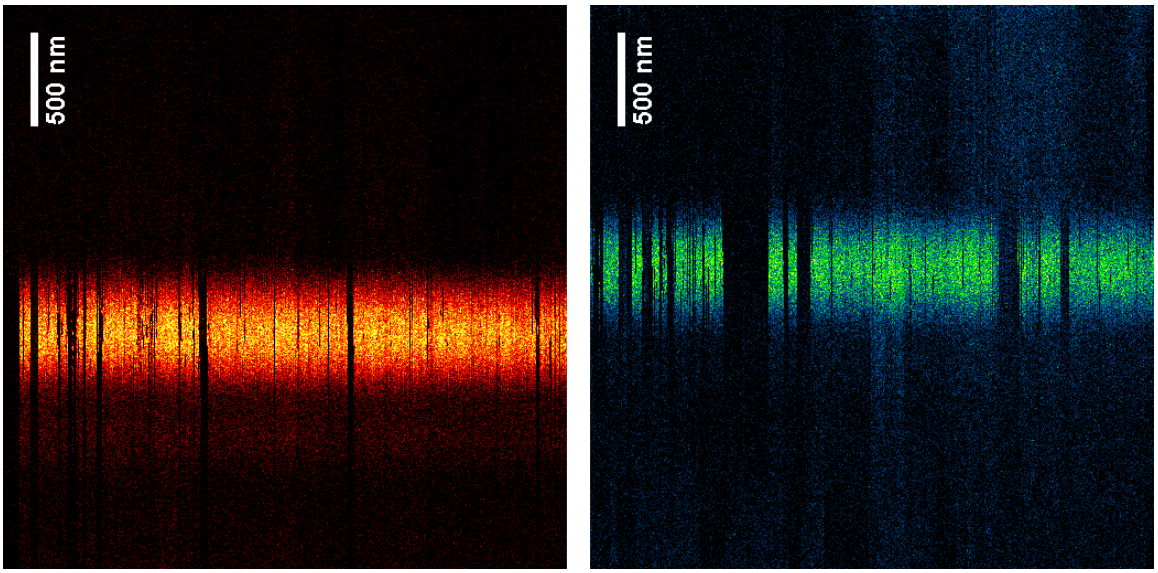

Figure 4.7: FSCM two channel imaging of two different quantum dot sizes. One size has emission wavelength of 617 nm (left) and the other has an emission wavelenght of 556 nm (right). The separation distance between these two quantum dots is 352 nm.

The results of the two channel studies are shown in Figure 4.8. Since the two channel studies required vertical alignment of quantum dots in two separate windows, the difficulty of finding appropriate quantum dot pairs was appreciably higher than in the original studies. Only 22 quantum dot pairs were located for the study, yet the relationship between the PPMCC and the quantum dot separation distance was still applicable. Of particular note is the existence of only 2 of the quantum dot pairs' blinking that is anti-correlated. Only 9.1% of the pairs were anti-correlated compared to

18.3% of the pairs from the one channel studies. Figure 4.8 also shows an inverse distance fit as well as the fit from the 60 quantum dot pairs from the one channel studies, first shown in Figure 4.4.

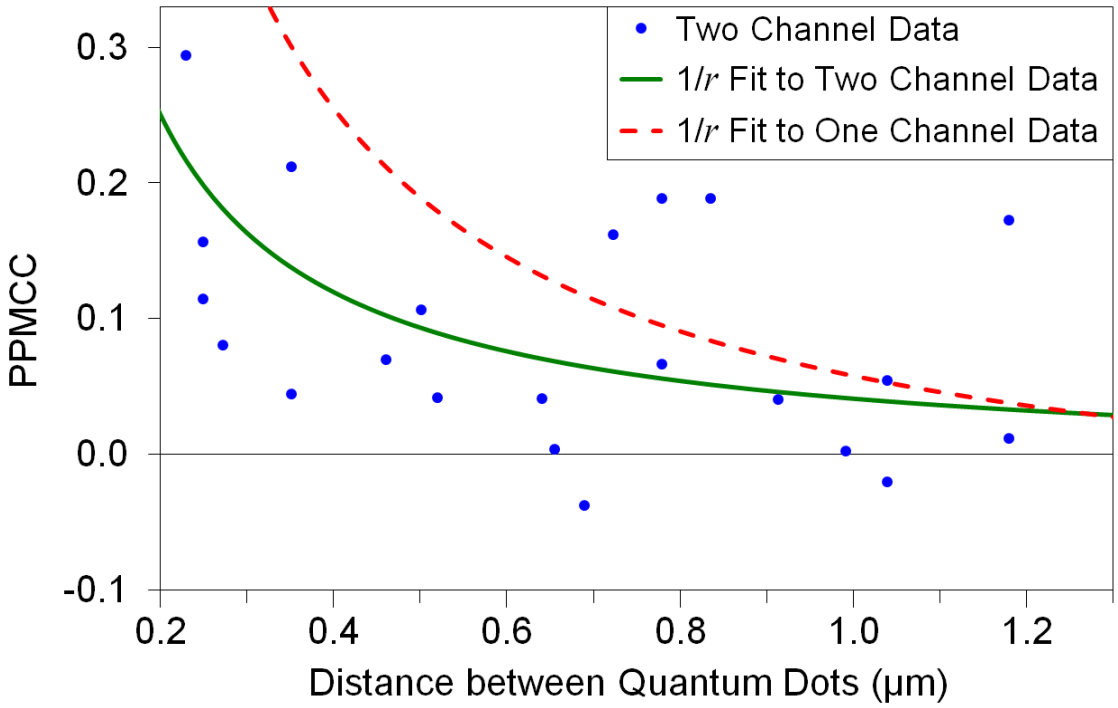

Figure 4.8: The PPMCC of 22 individual quantum dot pairs plotted versus separation distance. All of the pairs included quantum dots from different sizes, initiating the use of two channel imaging. A fit to inverse distance is shown as is the one channel data inverse distance fit, for comparison.

The two channel data is indicative of a blinking correlation that is markedly lower than the correlation for the one channel data. Two straightforward reasons can be given to explain the difference. As outlined previously, for quantum dot pairs less than ~500 nm, a modest addition to the PPMCC value may be considered. Adding the previously calculated PPMCC adjustment value of 0.035 to the PPMCC values for quantum dot pairs closer than 500 nm reduces the difference slightly. Likely more importantly, only 22 quantum dot pairs were located. Once again, heterogeneities among individual

quantum dots likely dictate the decline in overall blinking correlation. With a relatively small population of quantum dots, even a few heterogeneities would have a substantial effect on the fitting results.

The most substantial blinking correlation can be found at distances less than one micrometer. This can be ascertained primarily from Figure 4.4, where PPMCC values do not exceed 0.15. The two channel data follows a similar trend other than a single quantum dot pair, for which the PPMCC is nearly 0.20. Considering only PPMCC values corresponding to separation distances of less than one micrometer, the average PPMCC can be calculated. For the original 60 dot pairs studied, the average PPMCC in this range is 0.128 ± 0.045 while the average PPMCC over the same range for the two channel studies is 0.121 ± 0.044. Using the average as an indicator of blinking correlation is reasonable, since PPMCC values do not vary greatly for separation distances less than one micrometer. The fitted lines shown in Figure 4.8 assume an inverse separation distance relationship, which will be discussed in more detail in the next section.

4.4 Explanations of Blinking Correlation: Charging and Dipole Interactions

In order for the blinking of quantum dots separated by distances of one micrometer or more to be correlated, an interaction energy had to exist with enough magnitude to affect the blinking behavior. Earlier studies have shown that spectral diffusion in the emission of individual quantum dots can be dictated by changes in excitation intensity and ambient temperature, among other factors.[58] Furthermore, spectral diffusion and blinking behavior have been noted to be inexorably linked.[37,59] Spectral diffusion of ~4.2 meV has been tied to a change in the emissive behavior of

single quantum dots.[59] Therefore, an interaction energy between two quantum dots of approximately 4-5 meV could alter their emissive state.

Quantum dots have been found to contain an inherent dipole,[60] which can also be affected by the delocalization of a charge carrier from the core to become trapped near the surface of the quantum dot, as discussed in Chapter 1. Since any dipole-dipole interaction would be considerably less than dipole-point charge interaction, the first consideration was to find the effect of a dipole-point charge interaction to determine if it is sufficient to alter blinking dynamics. The interaction energy of a dipole-point charge, V_{dpc}, can be found using

$$V_{\text{dpc}} = \frac{-\mu_1 q_2 \cos\theta}{4\pi\varepsilon\varepsilon_0 r^2} \tag{3.7}$$

where μ_1 is the dipole moment, q_2 is the magnitude of the point charge, θ is the angle between the dipole and a line connecting the two quantum dots, ε is the dielectric constant of PMMA (3.5), ε_0 is the dielectric permittivity of a vacuum, and r is the separation distance. If all parameters are optimized for the maximum interaction energy for a separation distance of 500 nm, the interaction energy is approximately 6.6 μeV. Since this value is nearly three orders of magnitude less than the energy required to have an effect on blinking dynamics, another interaction was considered.

If two neighboring quantum dots were both charged with one of the charge carriers in an exciton being completely ejected into the surrounding matrix, the interaction would be a purely Coulombic one. The Coulomb interaction between two dots can be calculated using:

$$V = \frac{-q_1 q_2}{4\pi\varepsilon\varepsilon_0 r} \tag{3.8}$$

where all parameters are as noted in Equation (3.7), with the only addition being q_2, the point charge of the second quantum dot. At a separation distance of 500 nm, the Coulomb interaction is approximately 0.82 meV. Since this is still about five times less than the interaction energy necessary to affect blinking, multiple charging must be considered. If both quantum dots undergo ejection of two charge carriers, Equation (3.8) yields an interaction energy of about 3.3 meV. Asserting even higher amounts of charging, such as three charges per quantum dot, a value of 7.4 meV is obtained for a separation distance of 500 nm. The Coulomb interactions for quantum dots with multiple charges are well aligned with the energy needed to affect blinking dynamics, which is between 4 and 5 meV. The three scenarios of neighboring quantum dot interactions are illustrated by Figure 4.9.

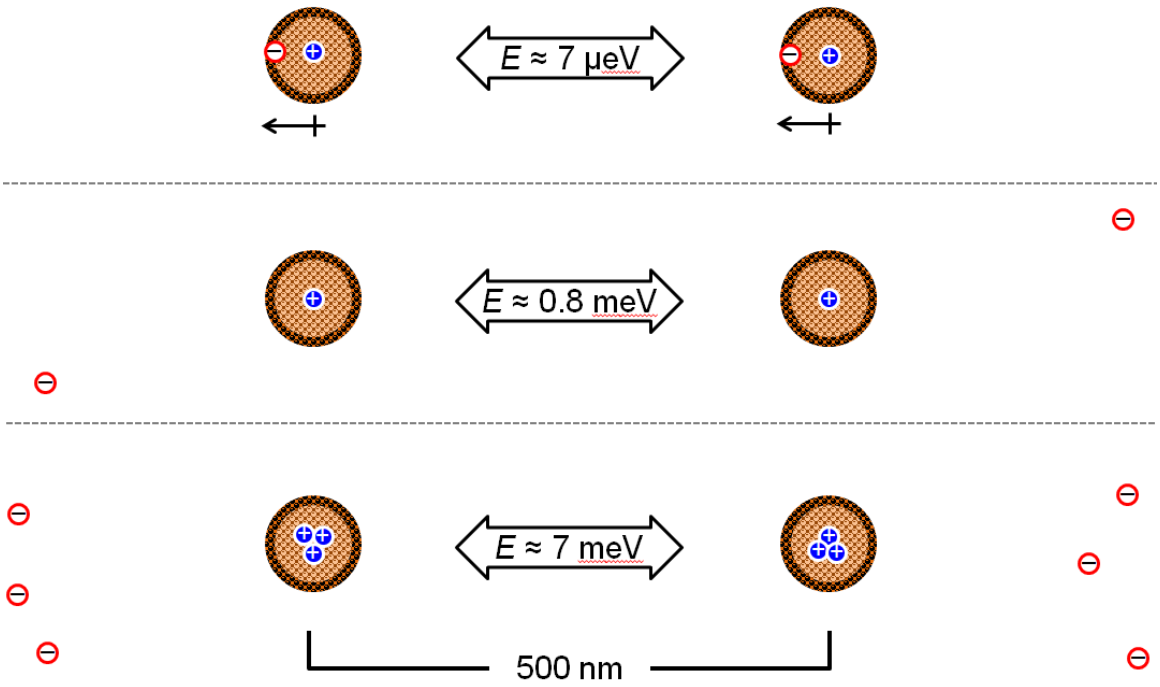

Figure 4.9: Possible interaction mechanisms for quantum dot pairs. Electrons are shown as red outlined circles while holes are solid blue with white outlines. The top scenario represents a dipole-dipole interaction in which the excitons are confined to the core of the respective quantum dots. The second scenario two singly charged quantum dots while the final scenario shows each quantum dot with charges of +3 *e*. The interaction energies for each scenario are given inside of each double sided arrow.

4.5 Slow FSCM experiments

To further test the theory of multiple charging being primarily responsible for the high level of blinking correlation, another experiment was conducted in which the scanning speed was slowed from ten lines per second to only one line per second. In effect, this provided more time for each quantum dot to discharge before its neighbor was to be scanned. If multiple charging and the resulting Coulomb interaction are responsible for the blinking correlation, the blinking correlation was expected to decrease at the slower scan speed.

Figure 4.10 shows the results for the slow scanning studies. The slow scan data clearly suggests a much lower overall correlation than the original "fast scan" experiments. The inverse distance fit to the slow scan data shows a sharp contrast to the original fast scan data fit. Approximately the same percentage of data points, 18.8%, was anti-correlated in the slow scan data in comparison to the 18.3% of anti-correlated data points for the fast scan data. However, a much larger disparity is apparent when comparing the average correlation at distances less than one micrometer. The average PPMCC value for the slow scan data is 0.0457 ± .041 compared to 0.128 ± 0.045 for the fast scan data.

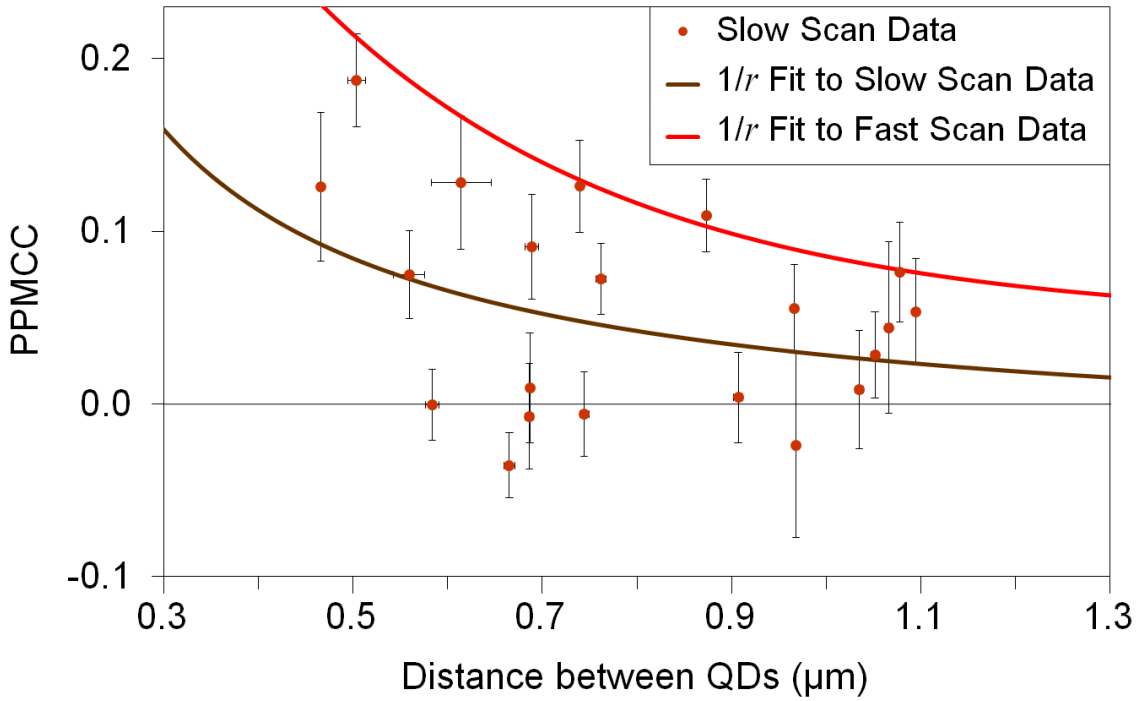

Figure 4.10: The PPMCC values for 22 neighboring quantum dot pairs measured with a scan speed of 1 line per second. The solid line is best fit line using the inverse distance relationship. Error bars are shown and derived using the same methodology used for the ones shown in Figure 4.4. For comparison purposes, the best fit line from Figure 4.4 is also shown.

Since the excitation beam takes longer to travel between the two quantum dots in the slow scan experiments, the lower PPMCC values suggest some level of discharging on a timescale of milliseconds. Since the total scan range for each line was 3 micrometers, quantum dots separated by a distance of one micrometer are separated temporally by ~167 ms considering the beam travels the length of the image twice for each line in order to reset its position for a new line scan. Despite the reduced blinking correlation for the slow scan experiments, a positive correlation still exists. This suggests a discharging rate on the order of 100 or more milliseconds. This is further support of a multiple charging effect since the recombination of a single charge carrier has been shown to happen on a much faster timescale.

One of the major drawbacks to conducting a slow scan experiment was that a single quantum dot pair took over 8.5 minutes to image. Similar to the original fast scan experiments, many of the quantum dot pairs were unusable in final analysis since one or both of the dots would be non-emissive for more than 25% of the full image scan. Due to the time scale of the study, this was a more common occurrence than in the fast scan studies. Conducting an even slower scan experiment, in which the temporal separation is on the order of 1 second or more, would take over an hour per image scan, with no guarantee that an image would be useful. Hence, other methods were explored to further test the theory of multiple charging.

4.6 Conclusion

A summary of the blinking correlation studies can be seen in Figure 4.11. For each of the fits shown, the average PPMCC for separation distances from 300 nm to 1000 nm is referenced in the legend. Based on the average value alone, the fast scan studies

indicate a substantial blinking correlation between neighboring quantum dots. The slow scan study supports a charging model since the lower correlation suggests that individual quantum dots are discharging while not under illumination. Although the two channel fast scan and one channel slow scan fits are very similar, it should be cautioned that heterogeneities among individual quantum dots, the PMMA matrix, or other environmental factors unaccounted for (such as ambient temperature) can have ample effects on the fitted curves.

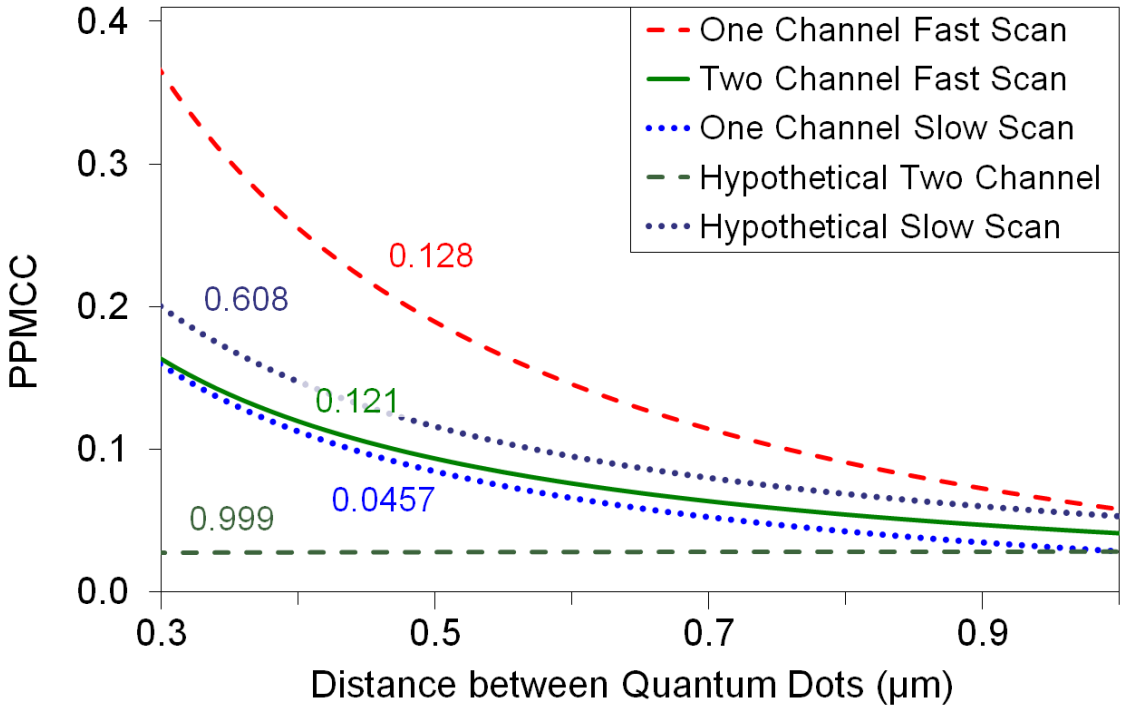

Figure 4.11: Fits to 1/*r* for blinking correlation studies. Included are the fast scan, slow scan, and the two channel studies. Average PPMCC values for distances less than one micrometer are shown adjacent to each trace. Two hypothetical data sets were created and fit to illustrate the effect of heterogeneities on best fit lines.

To illustrate the perceptible effects of heterogeneities on the fits to the relative data sets, two hypothetical data sets were created and fit in Figure 4.11. The slow scan data was modified such that the two lowest PPMCC values for distances of less than one

micrometer were deleted. The modified dataset was fit to the inverse distance relationship and displayed in Figure 4.11 as the hypothetical slow scan fit. Likewise, the two channel data was modified such that the two highest PPMCC values for distances of less than one micrometer were deleted. The newly created dataset was once again fit to an inverse distance relationship and displayed in the figure.

The fit to the modified two channel data trends remarkably low in comparison to the other lines. The hypothetical slow scan fit trends higher than the original two channel data at every distance. Nevertheless, the average PPMCC value of the hypothetical data sets still reveal that the two channel dataset contains a higher blinking correlation when compared to the modified slow scan dataset. This exercise demonstrates the effect that heterogeneities can have on the dataset, particularly regarding the evident trend of the line fits to the blinking correlation. Since the average values still reflect a significantly higher PPMCC value for the modified two channel data compared to the slow scan data, average values should be emphasized in relatively small datasets, exemplified by the two channel data and slow scan data.

CHAPTER 5: BLINKING CORRELATION AND EXCITATION INTENSITY

Numerous external factors have been shown to affect the blinking dynamics of quantum dots.[58] Of particular interest is the noticeable effect that excitation intensity has on the blinking dynamics. Since it is so easily adjustable, experiments can be readily conducted with no alterations to the original samples.

5.1 Experimental Setup

Even more experiments were performed to examine various charging effects on individual quantum dots. Varying the laser excitation intensity and measuring the blinking correlation at each level was suitable to examine different levels of charging over time, given that charging was dictated by the incoming photons. Similar to the slow scanning experiments, low excitation intensities should generate relatively low blinking correlations due to a lower probability of charging via carrier ejection.

The excitation intensity was varied by changing the power control setting on the laser driver. The intensity was measured using a handheld laser power meter with 5% accuracy to intensities as low as 10 μW. The measurement was always taken immediately downstream of the first dichroic mirror, located at DBS_1 in Figure 2.1. Due to loss of beam intensity due to a mirror, the objective lens, the objective lens oil, and the glass coverslip, the reported intensity at the sample was then scaled down appropriately, based upon empirical measurements for the correct scaling. Reported measurements

were converted to units of $kW \cdot cm^{-2}$ using the FWHM of the laser beam at the sample of 321 nm.

Intensities are also reported as average number of photons absorbed per laser pulse, $\langle N \rangle$, by individual quantum dots based on reported values for the absorption cross section of a CdSe nanocrysral.[61] Using the standard absorption cross section and a calculation of fluence, or $photons \cdot cm^{-2}$,[62] $\langle N \rangle$ was found and is reported for each intensity level.

5.2 Results of Varying Excitation Intensities

Figure 5.1 summarizes the results of varying the incident laser excitation intensity on the blinking correlation. The highest level of correlation is clearly exhibited by the highest excitation intensity, which corresponds to approximately 8.4 photons absorbed per pulse on average. Once again, an average of all PPMCC values at distances less than one micrometer was calculated. At $\langle N \rangle = 8.4$, the average PPMCC is 0.142 ± 0.047. The next highest intensity level, with $\langle N \rangle = 4.2$, had an average PPMCC of 0.107 ± 0.044. The third and fourth highest excitation intensities have blinking correlations inconsistent with the other trials. In Figure 5.1 it is apparent that the lowest intensity level, with $\langle N \rangle = 0.29$, exhibits a higher correlation than the intensity level where with $\langle N \rangle = 0.96$. In addition, the average PPMCC for the lowest intensity measurements is 0.0364 ± 0.041, which is greater than an average value of 0.0221 ± 0.039 for the second lowest intensity measurements. Despite this anomaly, the distinctive trend is that blinking correlation scales positively with laser excitation intensity.

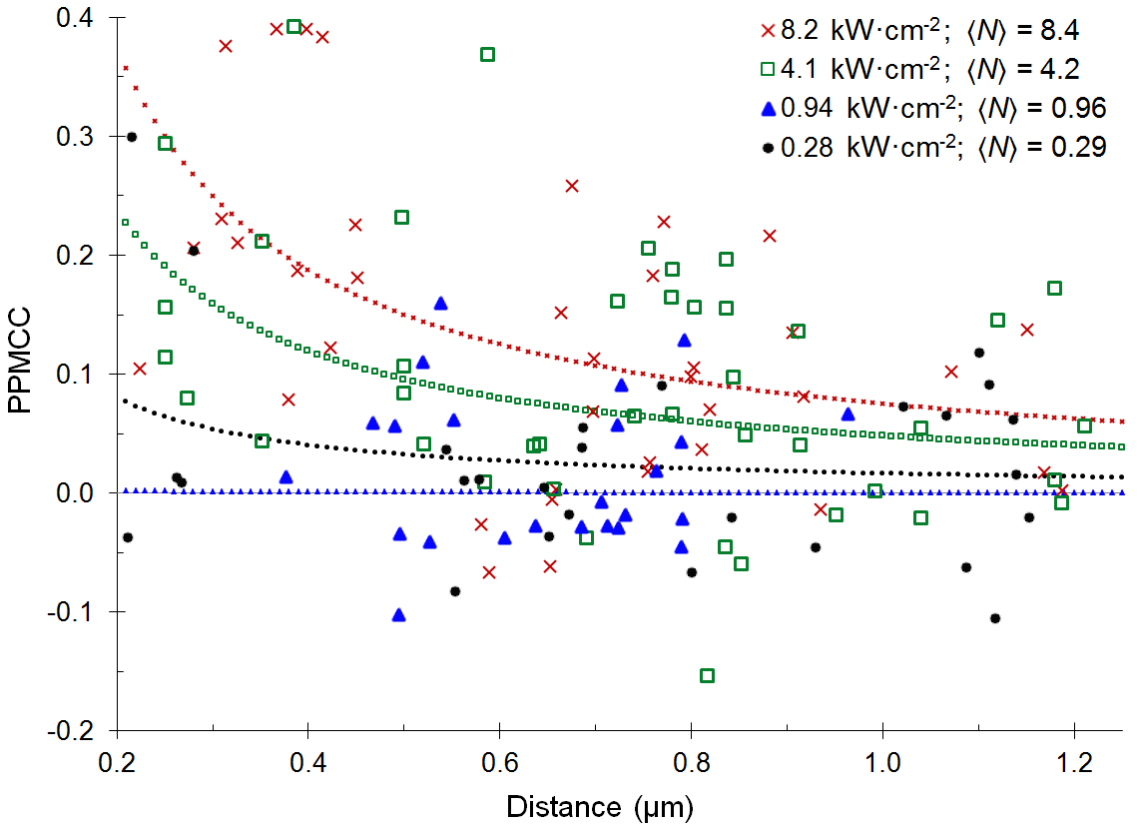

Figure 5.1: The PPMCC of at least 20 dot pairs at each of four different laser excitation intensities. Dotted lines are best fits to an inverse distance relationship. Corresponding intensities are listed in the legend with average number of photon absorbed per pulse noted as well.

A dependence on excitation intensity further supports a charging effect being primarily responsible for the blinking correlation. With a higher number of absorbed photons per pulse, a quantum dot is more likely to absorb enough energy to eject a charge carrier, thereby becoming charged. A higher excitation intensity also fosters a higher number of charge ejections overall, which means the charge on each quantum dot will tend to be higher on average. This is further supported by Califano *et al.* in the modeling work of multiple charging in quantum dot systems.[33] As detailed by Equation (3.8), the interaction energy would in turn increase and the blinking correlation would scale concomitantly with that increase.

5.3 Excitation Intensity and Multiphoton Emission

Individual emitters such as fluorescent protein molecules or chemically derived organic fluorophores are not known to be capable of multiphoton emission. Given a single excitation event, such fluorophores are observed to emit a maximum of a single photon. However, quantum dots have demonstrated the capability of maintaining multiexciton states[63] and also emitting multiple photons as a result of a single excitation event.[64,65] Multiexciton behavior has been shown to be strongly dependent on excitation intensity.[63] As a metric, we conducted a series of experiments to determine the relationship between multiphoton emission, specifically biexciton emission, and the excitation intensity. The results could then be connected to the observed blinking correlation at respective excitation intensities.

Using the HBT configuration outlined in Chapter 2, a photon correlation spectrum was generated for single quantum dots at a variety of excitation intensities. A sample spectrum is shown in Figure 5.2 where fluorescence from single quantum dot was collected over 60 minutes with an excitation intensity of approximately 1 $kW \cdot cm^{-2}$. The central peak, corresponding to a time of 0, is demonstrative of each detector receiving a photon within the same laser pulse. The central peak is often regarded as the biexciton peak or multiphoton emission peak since more than two photons had to be emitted from the quantum dot immediately following a single laser pulse event in order for the peak to appear.

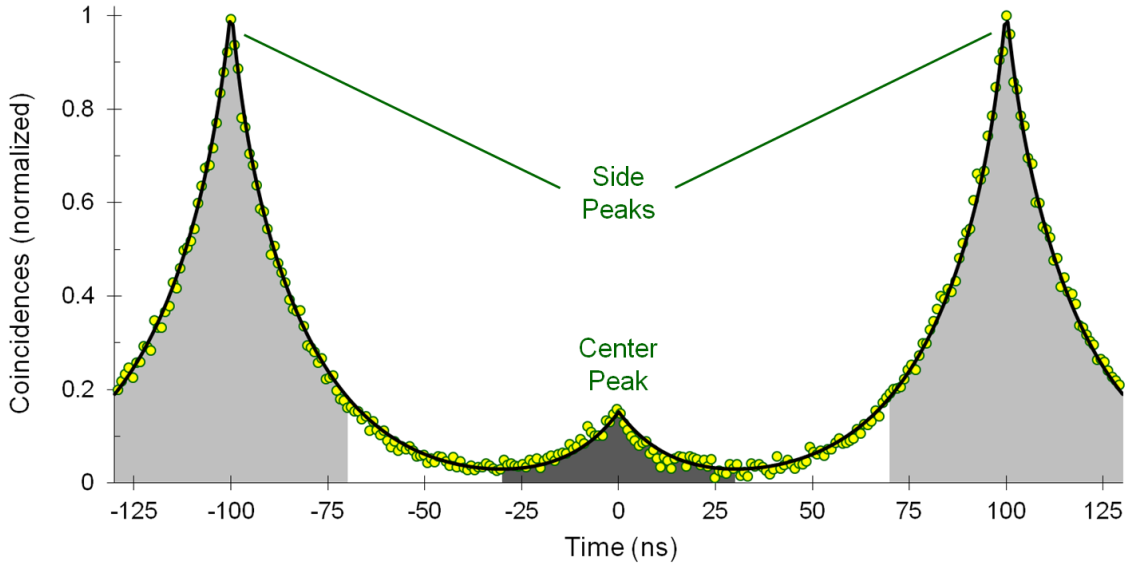

Figure 5.2: Sample photon correlation spectrum. The integrated area of the center peak (shaded dark gray) and the integrated area of the side peaks (shaded light gray) are both noted.

The left and right peaks, or side peaks, in Figure 5.2 are representative of emitted photons received by a detector as a result of the previous or subsequent laser pulse relative to start time established by the HBT configured pulse signal detector discussed in Chapter 2. A straightforward comparison of the center peak to the side peaks is useful for determining the relative amount of multiphoton emission in an experiment. The center peak is integrated over a set range and both side peaks are likewise integrated over a range of equal width. Figure 5.2 shows the resulting integration of the center peak as a dark shaded area, while the integration of the side peaks is lightly shaded. Dividing the integrated area under the center peak by the average integrated area of the two side peaks gives a ratio, which is representative of the likelihood of multiphoton emission for the quantum dot being studied. In Figure 5.2, the center-to-side-peak ratio is approximately 13.9%.

A similar experiment was carried out on a set of approximately 10 different quantum dots, all with a peak emission of 596 nm, for six different excitation intensities. The microscope stage was stopped directly over the nanocrystal and emission was collected for 60 seconds for each measurement. Instead of separately displaying individual measurements at a given excitation intensity, results were averaged at each intensity level. By averaging over 10 measurements, heterogeneities among the individual quantum dots were mostly repressed and the resulting multiphoton emission profiles could be ascertained. The photon correlation spectra derived from the experiments are represented in Figure 5.3.

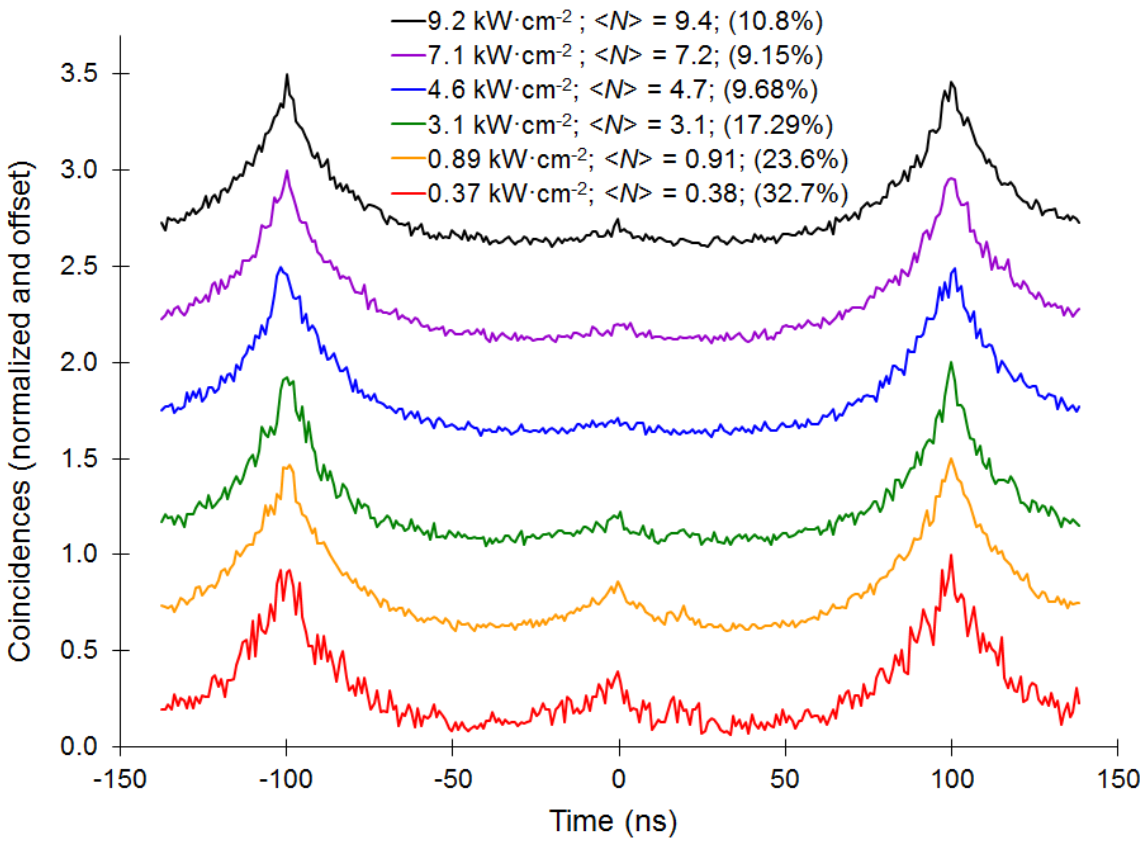

Figure 5.3: Results of photon correlation experiments at six different excitation intensities. They are listed by average irradiance and photons absorbed per pulse. The ratio of the center peak to the average of the two side peaks is presented as a percentage.

Noted in Figure 5.3 is the ratio of the integrated area beneath the center peak to the average of the integrated area beneath the two side peaks. Above an excitation intensity of 3.1 $kW \cdot cm^{-2}$, multiphoton emission decreases substantially. Conversely, the lowest two intensity levels exhibit the highest relative amounts of multiphoton emission. The implication of these findings is that a process in opposition to multiphoton emission tends to dominate at higher excitation intensities. If charging is responsible for blinking correlation, it is reasonable to assert that charging competes with multiphoton emission. Charging can be facilitated by Auger recombination through an assisted charge ejection mechanism in which recombination provides sufficient energy to overcome the binding energy of the charge carrier. Other research groups have already proposed that Auger recombination is in direct competition with radiative biexcition recombination.[66]

Perhaps a more intuitive perspective is to consider the fact that charge carriers cannot be both ejected and recombine radiatively at the same time. In addition, the timescale of a charging event is likely as high as hundreds of milliseconds, as discussed in the previous chapter. Once charging becomes a dominant process, competing processes, such as multiphoton emission, find little opportunity due to the relatively long time scale of a charging event.

One curious aspect of the photon correlation results is that the average number of absorbed photons per pulse is less than one for both of the low intensities, despite the fact that multiphoton emission is only possible in cases of multiphoton absorption. It must be the case that at least two photons are absorbed in a single pulse for a significant portion of the emission events. This is due partially to the probability distribution of incident photons. During some pulses, no photons are absorbed, but during other pulses, multiple

photons may be absorbed. The high multiphoton emission at lower values of $\langle N \rangle$ also implies that the reported value of $\langle N \rangle$ may not be wholly accurate. Even so, the relationship between excitation intensity and the emission of two or more photons in a single pulse is evident.

5.4 Excitation Intensity and Fluorescence Lifetimes

The lifetime of an emitter is the time it remains in an excited state before the excited charge carrier returns to a ground state. Fluorescence lifetime applies specifically to instances in which the carrier's return to the ground state also results in the emission of a photon. Measuring the fluorescence lifetime over a range of excitation intensities provides additional insight into the excited state dynamics, which can be utilized in the justification of the blinking correlation between neighboring quantum dots.

With the LSCM system, lifetimes can be easily measured using the reverse start-stop configuration detailed in Chapter 2. Ten separate quantum dots, all with peak emission of 596 nm, were chosen for the fluorescence lifetime measurements at each excitation intensity. At the lowest intensities, each measurement lasted 30 seconds, while at the highest intensities, measurements were reduced to 5 seconds to avoid overloading the lifetime software. All data was compiled at each intensity level and average lifetimes for the ten quantum dots studied were found. The results of the lifetime studies are shown in Figure 5.4.

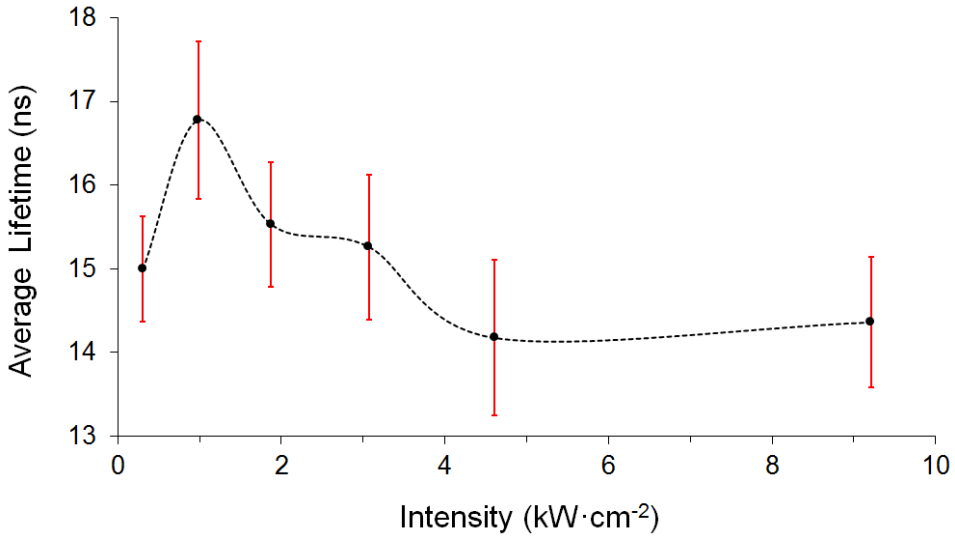

Figure 5.4: Average fluorescence lifetimes of 10 individual quantum dots at different excitation intensity levels. Error bars are one standard deviation of the average.

The general trend in fluorescence lifetimes is that higher excitation intensities produce the lower lifetimes. This trend is mostly consistent other than the lowest intensity measurement, the lifetime of which incongruously drops significantly compared to the second lowest intensity level.

A charging mechanism functions well in explaining the overall trend of lifetimes. Charge carriers are more likely to be ejected, likely by way of Auger recombination, if they spend a long time in an excited state. At higher excitation intensities there is a higher probability of Auger processes occurring since more excitons are being created per pulse, on average. It follows that a greater number of charge carriers, particularly those with long lifetimes will be affected by Auger recombination. The disproportionate loss of charge carriers with long lifetimes statistically lowers the average lifetime measurement.

The charging mechanism can also help to explain the trend in lifetimes considering the generally accepted belief that charged quantum dots utilize additional

relaxation pathways compared to an uncharged state.[67,68] The radiative and non-radiative decay rates both increase in the presence of multiple excitons. In cases of a localized multiple charge, an excited charge carrier would be significantly drawn towards the localized charges. A good demonstration of this scenario is when an electron enters an excited state, in which the hole is left behind. In the case of multiple charging, multiple holes exist in the vicinity of the last excited electron. The scenario virtually assures that a long fluorescence lifetime would be unlikely due to rapid recombination facilitated by additional positive charges, all of which contribute to a greater interaction energy with the excited electron.

5.5 Discussion

A possible scenario of how a charging event affects the fate of an exciton is shown in Figure 5.5. The quantum dot represented begins with a single exciton amidst the nearly simultaneous event of the creation of another exciton from an absorbed photon. Both excitons are created as a result of incident photons from the same laser pulse. Generally, the lifetime of a single exciton is 10 to 30 ns,[69] but the existence of two excitons changes the dynamics considerably.[29] The second stage in Figure 5.5 presents a possible outcome where one exciton is eliminated due to very fast Auger processes, within approximately 40 to 50 ps.[34] Auger recombination is responsible for the fast transition by transferring energy to the other excited electron and propelling it into the surrounding matrix. As a result of one of the ensuing laser pulses, another photon is absorbed by the quantum dot, which is now charged. The newly excited electron experiences a much shorter lifetime due to the existence of more pathways, having two holes instead of a single hole, as is the case for the electron from the first stage of the

figure. Therefore, the lifetime of the electron in the last stage is considerably smaller than the first stage electron.

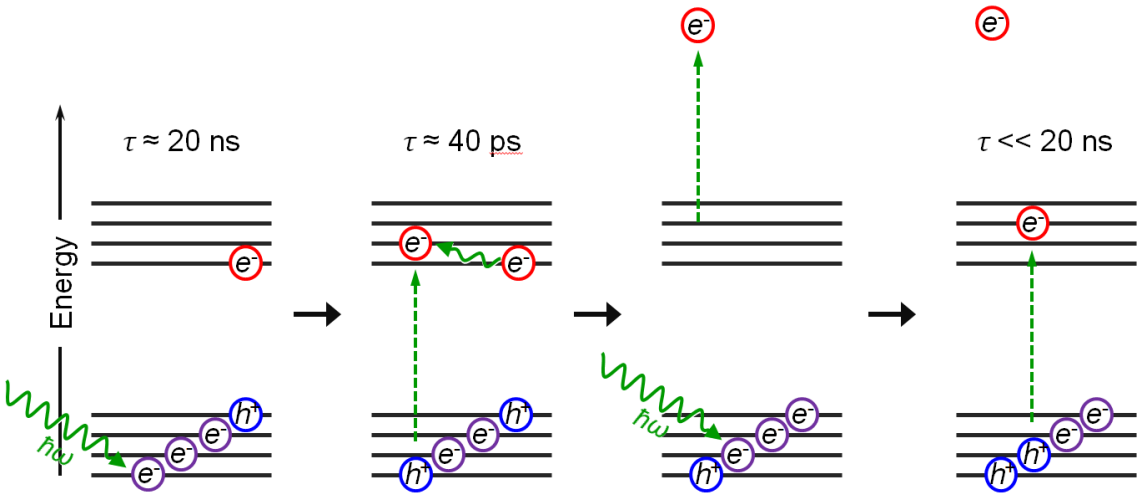

Figure 5.5: Possible mechanism by which an electron is ejected by Auger recombination. A charged, negative trion state results thereby altering the excited state dynamics of the system. Noted lifetimes (τ) are estimated based on published studies by various researchers.[29,47,69]

The probability distribution of on and off times follow an inverse power law trend primarily according to a mechanism proposed over a decade ago by Verberk *et. al*. A single ejected charge is expected to land in one of many static trap states in the surrounding environment, leading to a distance dependent recombination time.[26] The broad range of possible trap sites accounts for the power law behavior of on times. The same model further proposes that charging events may be followed by removal of the excess carrier from the core of the quantum dot. Usually, an ejection of an electron would be followed by the removal of the hole to a trap site in the shell or on the surface of the nanocrystal. The dynamic removal of the hole in this manner would switch the emission to a long lived on state, thereby partly accounting for the power law behavior of the on state. Multiple charging however, does not allow for the advancement of another

stipulation of this model, namely that charge ejection introduces a Coulomb blockade that would eliminate the possibility of any further charging.

Another mechanism could resolve the discrepancy that a Coulomb blockade renders further charging impossible. Kuno et al. proposed that time dependent shifts in the tunneling barrier between the core of a quantum dot and the surrounding trap sites would produce the requisite power law distribution of on and off times.[18] Instead of a Coulomb blockade, a dynamic tunneling barrier, dependent upon the extent of charging and excess carrier delocalization, would yield a higher distribution of on times. This model must concede that quantum dots may still be emissive given a set of ejected charges and the corresponding carriers relocated from the core. The corresponding changes of the tunneling barrier could be explained by the dynamic process of charge ejection and removal rather than by conformational changes in ligands, as proposed by Kuno *et al*.

A wide degree of configurations are possible, each of which affect the tunneling barrier size, thereby contributing to a large distribution in sizes. For example, given the ejection of a single electron and the subsequent relocation of the hole to the shell, three unique positions of the tunneling barrier are evident, including the native state, the charged state and the final state in which both charge carriers are delocalized from the core. Subsequent ionization would permit more configurations. A wider distribution of configurations are possible, given that delocalized holes could occupy any number of trap sites near the surface. In addition, the ejection distance of the electron would affect the tunneling barrier potential.

Although multiple mechanisms may contribute to blinking, our results offer little support of several popular proposals. Diffusion of the trapped charge, whether energetic[37,38] or spatial,[70] would not be necessary in a multiple charging model. Static trap sites for ejected charge carriers are likely in a polymer medium. Likewise, surface traps in polymer-embedded quantum dots would be expected to undergo far less energetic changes, compared to a solution environment. Our results are supportive of mechanisms with a distribution of static trap sites.

Other models propose that charging of quantum dots does not have to occur for power law blinking behavior to be explained. Rather, hole trapping occurs, rendering the quantum dot non-emissive. Given a long time scale of hole trapping, sufficiently long off times occur and power law blinking behavior can be explained.[71,72] The hole trapping rates depend either on diffusion of the excited state electron or on dynamic trap site availability. In these models, ejected charges are not considered since Auger processes are instead imposed by hole trapping and not by a charged quantum dot core. Therefore, it is difficult to substantiate hole trapping models based on our observations.

5.6 Conclusion

Excitation intensity is expected to affect the average charge on individual quantum dots as well as the degree of charging.[39] The findings outlined in this chapter support this claim and additionally advocate a mechanism by which quantum dots remain emissive even in a charged state. Blinking correlation between neighboring dots increases similarly with excitation intensity. Since blinking correlation necessitates the presence of multiple charges, singly charged states may still be emissive as is the case in

states with two or more charges. The point of charging at which a quantum dot becomes non-emissive is still up for debate.[66]

The requirement of quantum dots to become charged to demonstrate a blinking correlation also affects the probability of multiphoton emission. A higher charging probability is expected to lower the emission of two or more simultaneous photons since a charge carrier cannot radiatively recombine and be ejected from the construct at the same time. The lifetime decay times of the quantum dots at various excitation intensities further support these claims, considering that lifetime decay rates are expected to increase with the level of charging.

CHAPTER 6: BLINKING CORRELATION NEAR A GOLD SURFACE

In the presence of gold, multiphoton emission has been found to be greatly amplified.[62] The justification for the enhancement was suggested to be the result of strong coupling with multipole modes of the plasmon modes in a gold layer. The apparent reciprocal relationship between blinking correlation and multiphoton emission prompted a study of blinking between neighboring quantum dots in the presence of a gold layer. Based on the experiments already done in absence of gold, the expected outcome was that the blinking correlation would be at least partially mitigated in the presence of gold.

Figure 6.1 summarizes two photon correlation experiments, one for quantum dots in the presence of gold and the other without a gold presence. Both experiments were conducted using an excitation intensity of 4.6 $kW \cdot cm^{-2}$, which is equivalent to $\langle N \rangle = 4.7$. As shown by the figure, the multiphoton emission is intensified for quantum dots in the presence of gold. Quantitatively, the center peak size for the data without gold is 9.3% of the side peak. In the presence of gold, this ratio increases to 22.6%, an increase of more than twofold. The presence of gold also fosters an additional, fast lifetime decay component. Due to this addition, the data for the quantum dot near gold is fit using two exponential components in the decay. This is in contrast to the fit for the data with no gold, where all peaks were fit to single exponential decays.

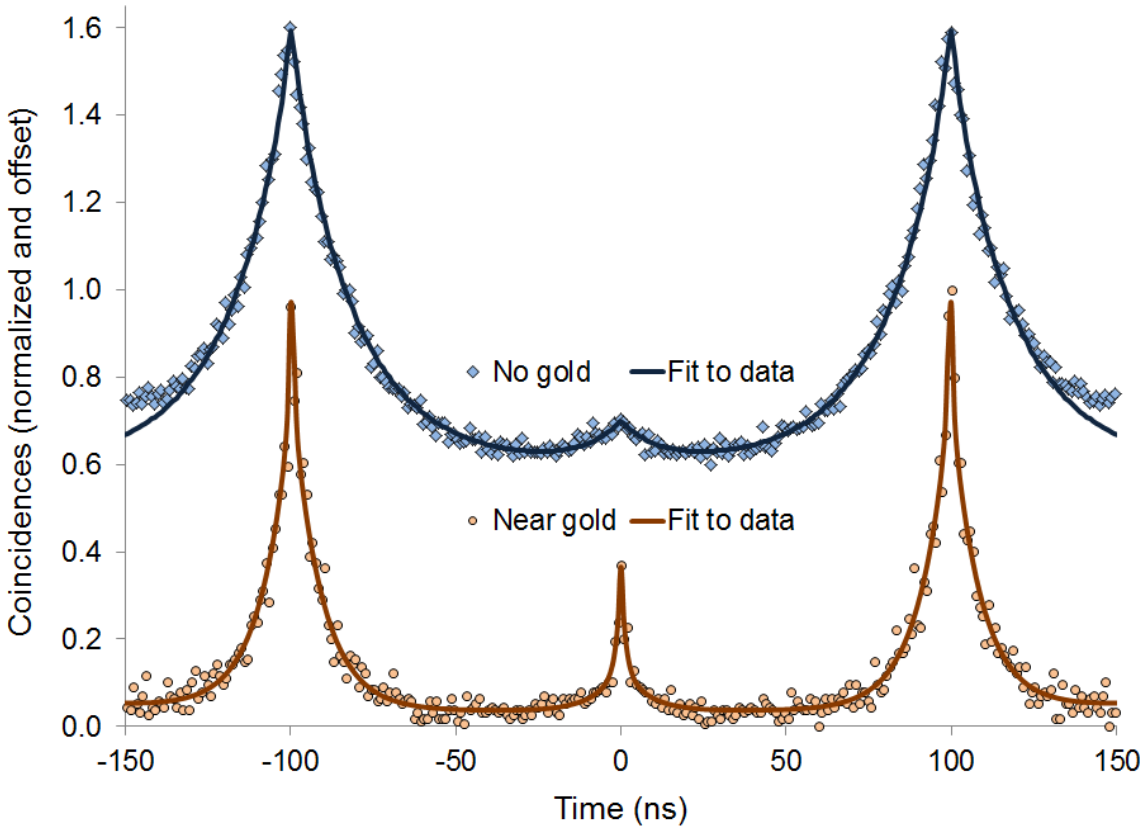

Figure 6.1: Illustration of increased multiphoton emission near a gold surface. A photon correlation experiment without gold is represented by the blue diamonds while the same experiment in the presence of gold is shown with gold circles. The fit to the data without gold is done using single exponential decays at each peak. The data taken near a gold surface is fit using two exponential decays for each peak.

6.1 Experimental Setup

Commercial CdSe/ZnS quantum dots with peak emission of 596 nm were mixed in a solution of 1.5% PMMA in toluene. The final concentration of quantum dots was approximately 1.0×10^{-11} M. The solution was spin coated onto a 25 × 25 mm glass coverslip at 1500 rpm for 30 seconds. The thickness of the PMMA was estimated to be 75 nm based on well documented protocols for ultrathin layers of PMMA.[73,74] Using a DC power sputtering tool, an AJA International ATC 1800-F, a power of 25 Watts was applied for 15 minutes, producing a gold layer with thickness of approximately 100 nm

on top of the dried PMMA layer. An illustration of the sample is shown in Figure 6.2. Although the gold is represented as a flat surface, it is relatively uneven due to the preparation of the PMMA layer. The PMMA layer is not smoothed beyond basic spin coating and the resulting gold sputtered surface contains many imperfections on the order of several nanometers.

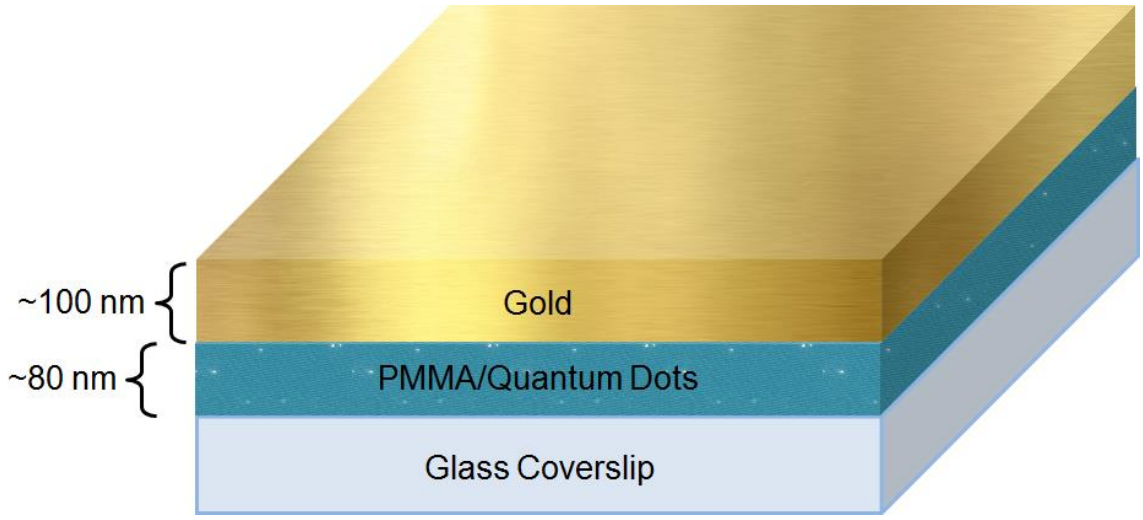

Figure 6.2: Sample prepared with quantum dots near a gold layer. A layer of quantum dots suspended in PMMA is covered in a thin layer of gold. The gold layer is a relatively rough surface since the PMMA was not smoothed.

FSCM was utilized with a standard 512 × 512 pixel image size and a scan speed of 10 lines per second, resulting in 51.2 second image generation. Only images in which each quantum dot remained in an emissive or blinking state for at least 50% of the image were analyzed. Over 100 quantum dot pairs were studied, but numerous blinking profiles were unusable, leaving approximately 60 pairs with blinking patterns sufficient for analysis. A series of excitation intensities was also applied, from 0.4 $kW \cdot cm^{-2}$ to over 9 $kW \cdot cm^{-2}$. The customary 605/50 BPF filter was placed in the emission path for these experiments.

6.2 Experimental Results

The results for all six different excitation intensity levels are summarized in Figure 6.3. Since there was no statistical difference in the average PPMCC values for each intensity level, all 60 quantum dot pairs, regardless of excitation intensity, were fit to a single inverse distance function, represented by the solid black line in the figure. The average PPMCC value for all pairs within 1000 nm of each other is 0.0327 ± 0.0405. Since the overlap of the PSF is expected to contribute at least somewhat to the PPMCC value for each pair, the average nearly demonstrates a completely random blinking correlation. Even when compared to the relatively low correlation values from the slow scan experiments, the trend for the PPMCC of quantum dot pairs represents a smaller correlation.

Another notable aspect of the fluorescence profile of quantum dots near a gold surface is that their total emission is reduced compared to the standard sample without a gold layer. For example, at an excitation intensity 4.6 $kW \cdot cm^{-2}$, the total emitted photons over the course of a 51.2 second scan of two dots averages just over 5 million when there is no gold layer. In contrast, in the presence of gold and at the same excitation intensity, the average emitted photons from two quantum dots during a 51.2 second scan is approximately 4.3 million.

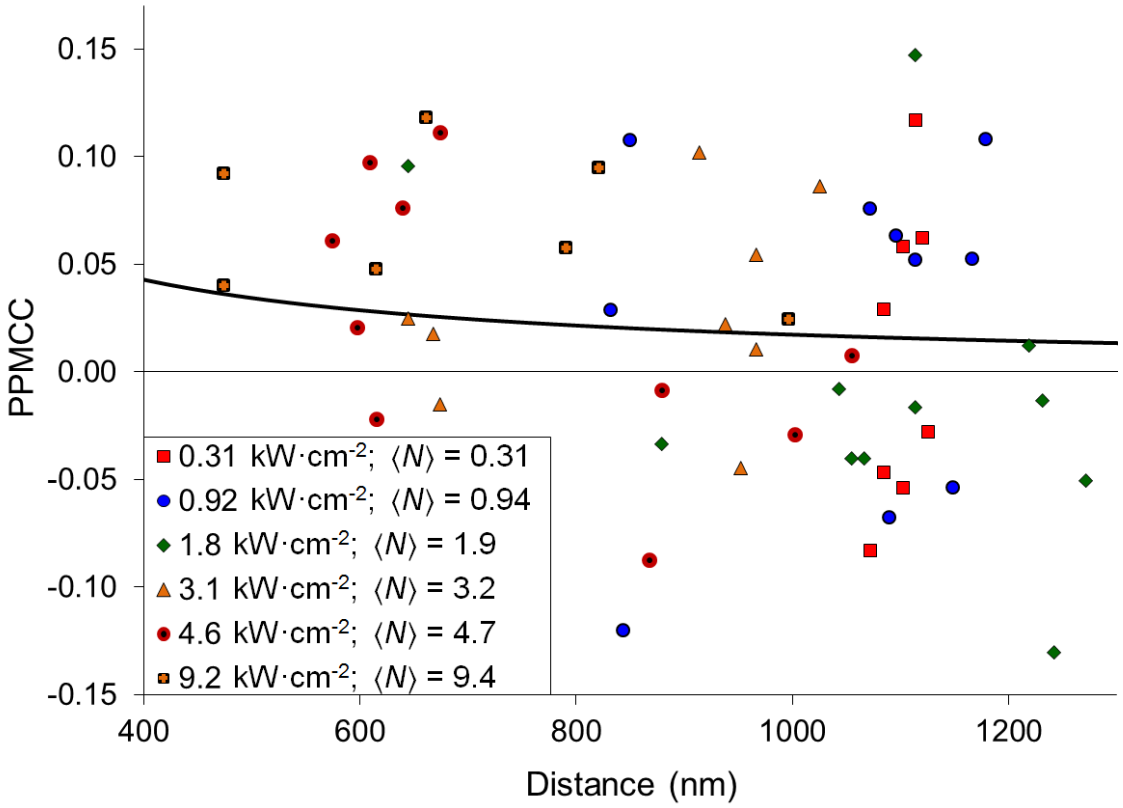

Figure 6.3: Blinking correlation near a gold surface. Six different excitation intensities are represented but universally fit to an inverse distance relationship (solid line). For quantum dots separated by less than 1000 nm, the average PPMCC is 0.0327.

6.3 Discussion

The lack of excitation intensity dependence for the data indicates that the mechanisms present in these experiments, which seem to be in competition with charging, scale with intensity. In fact, they scale at least as significantly as the charging mechanism. As discussed in the previous chapter, an increase in excitation intensity is expected to increase the charging of individual quantum dots. Based on the results of the experiments in absence of gold, a much higher blinking correlation is observed, strongly suggesting a higher probability of charging. However, the same relationship between

excitation intensity and blinking correlation is not observed in the presence of gold, indicating that charging is heavily mitigated by gold.

The increased probability of multiphoton emission in the presence of gold is indicative of enhancement mechanism due to surface plasmon coupling.[75-77] A surface plasmon is a resonant oscillation of the resident electron cloud in a metallic layer. If the resonance frequency of the plasmon corresponds to an incident electromagnetic wave, the plasmon will be appropriately amplified. The resonant frequency of the plasmon of gold is nominally in the visible spectrum, although the exact wavelength depends on numerous factors including the shape of the gold, the surface roughness, its purity, and numerous other factors.[78]

As noted in the experimental results, the quantum efficiency or overall emission of quantum dots in the presence of gold is not increased. Since this is in stark contrast to the response of the multiphoton emission, the surface plasmon interaction must therefore couple only to a biexciton, trion, or greater excited state. One proposition is that the quadrupole that is created as a result of a biexciton couples very efficiently to the quandrupole moment in the plasmon.[62] The coupling effectively neutralizes many of the opportunities for multiple charging. The increase in multiphoton emission means that Auger recombination is likely suppressed, thereby decreasing the probability of charge ejection by means of an Auger process pathway.

6.4 Conclusion

The process of multiphoton emission has been shown once more to be in direct competition with the mechanism responsible for blinking correlation between neighboring quantum dots. As we are inclined to suggest a multiple charging process as

the rationale for the blinking correlation phenomenon, it is therefore likely that a gold surface prohibits charging by mitigating relevant pathways, such as Auger processes. This is most likely due to a coupling of the gold plasmon with the emissive biexciton state of a quantum dot.

CHAPTER 7: MULTIEXCITON IMAGING

To more thoroughly examine the excited state dynamics of quantum dots in the presence of gold, a new set of experiments was designed. In samples without gold, the multiexciton emission was inversely related to the excitation intensity as shown by Figure 5.3. Conversely, in the presence of gold, quantum dots had a higher probability to emit multiple photons during a single excitation event. This phenomenon strongly affected the blinking correlation between neighboring quantum dots. By studying the extent of multiexciton emission while scanning across the width of a single quantum dot, a more detailed description of the phenomenon could be obtained. In addition, a high resolution version of imaging could also be developed. By utilizing the trend in multiexciton emission as a single quantum dot was scanned, the PSF could effectively be narrowed, yielding a version of imaging with higher spatial resolution.

7.1 Experimental Setup

A construct identical to the one shown in Figure 6.2 was prepared. Once again, a quantum dot concentration of approximately 1.0×10^{-11} M was used to obtain a sample in which single particles could be imaged. Once located, single quantum dots were slowly scanned by placing the quantum dot at the center of an image with a 1000 nm width. The height of the image was set to effectively zero, thereby creating a single dimension spatial image, similar to the FSCM imaging. An image in which a quantum dot is positioned near the center of the scan range is shown in Figure 7.1. The image shown

was taken over the course of 256 seconds using a scan rate of two lines per second on a 512×512 pixel image.

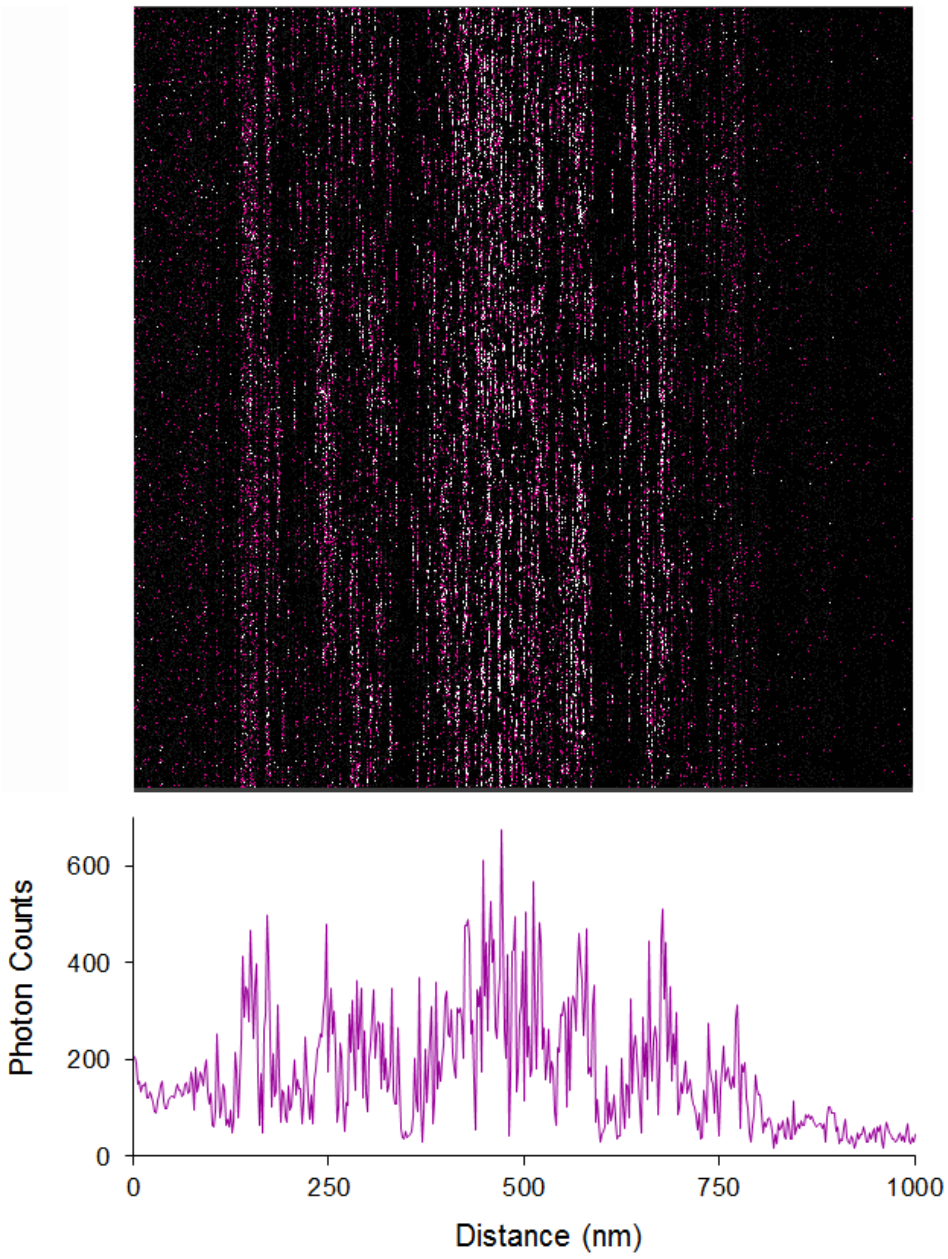

Figure 7.1: Image generated by a one dimensional scan across the center of a single quantum dot. The sum of each line is shown in the chart below the image.

Before acquiring a full data scan with multiphoton emission statistics, the main flip mirror, shown in Figure 2.1, was utilized to first allow imaging using the first APD. Once the scan coordinates were established, the full scan was conducted with the mirror down, utilizing the two APDs behind the flip mirror. Emitted photons were randomly directed towards either APD using a non-polarizing cube beamsplitter. The standard HBT configuration was employed to record photon correlation spectra. The full scan time of 256 seconds was slightly abridged to 250 seconds and subsequently divided into ten equal time segments of 25 seconds each. The center peak ratio (CPR) was determined by first counting the number of photons found in the center peak area, from –25 to +25 seconds. This was divided by the average photons found from the two neighboring side peaks at times of –125 to –75 and +75 to +125 seconds, respectively. The peak areas highlighted in gray from Figure 5.2 appropriately represent the ratio of the center peak to the side peak. The CPR was calculated for each 25 second time interval.

7.2 Experimental Results

A representative data sample is shown in Figure 7.2, where the maximum CPR observed was approximately 0.57, while the minimum peak ratio was approximately 0.19. The CPR was not tabulated near the edge on either side of the quantum dot due to an insufficient amount of emitted photons. Even so, the CPR outlines a profile of the quantum dot almost precisely aligned with the actual Gaussian fit shown. This is evident in the figure by the red shading near the edges of the Gaussian and the blue shading near the center. A consistent trend of the highest CPR on the outside of the quantum dot to the

lowest CPR at the center is followed. An adapted version of the MATLAB routine shown in Appendix B can be used to generate the data shown in Figure 7.2.

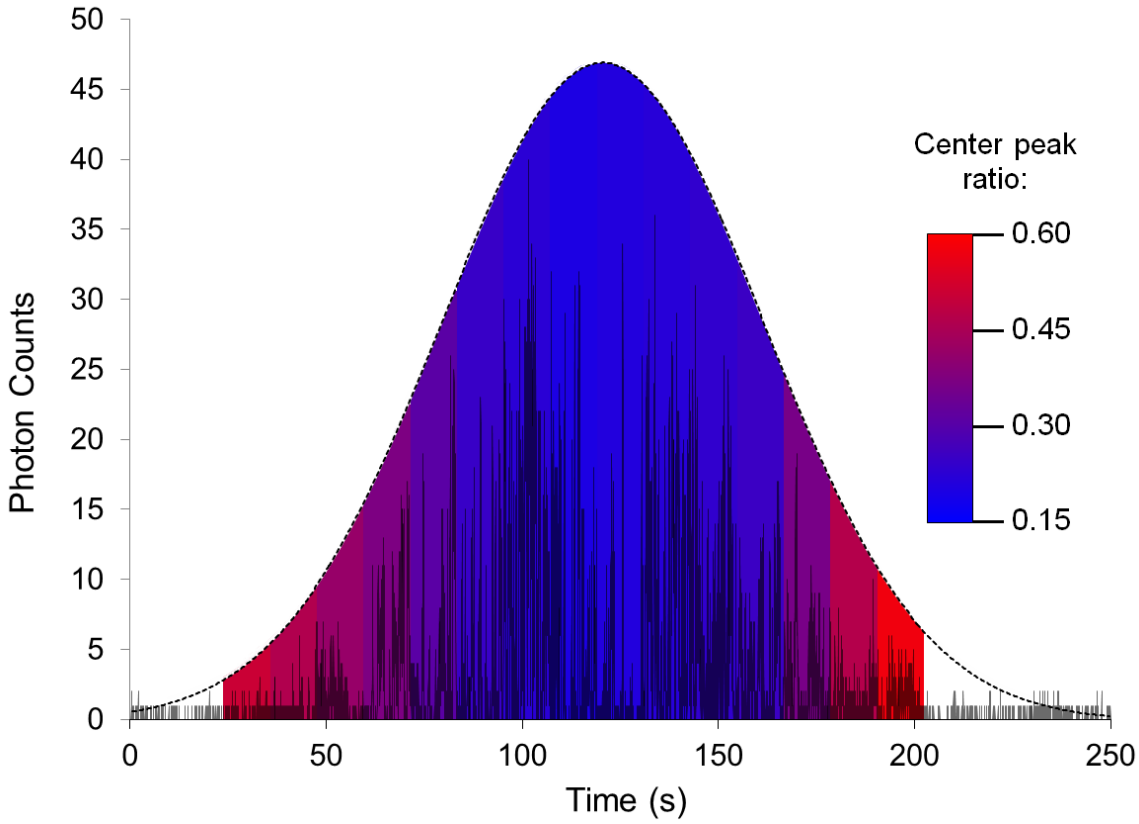

Figure 7.2: Multiexciton emission profile across a scan of a single quantum dot. A Guassian fit, with manually adjusted parameters, is filled by the appropriate center-to-side peak ratio at each time interval of 12.5 seconds. The dark gray semi-transparent trace is the blinking pattern of the quantum dot, which corresponds to the y-axis shown.

The Gaussian fit to the quantum dot profile shown in Figure 7.2 is manually added and sized appropriately. Applying an automated fit to a profile with blinking can be very difficult, depending on the amount of blinking. For example, an automated Guassian fit to the data shown in Figure 7.2 is not entirely accurate despite a fairly consistent emission profile of the quantum dot. The difficulty of fitting a standard quantum dot trace is due to many factors, the most obvious being that large gaps in data

can exist while the quantum dot is non-emissive. The width of the histogram bins for the blinking trace also determines the smoothness of the data. For example, in Figure 7.2 bins of 30 ms were used for the gray trace. Smaller bin sizes typically make fitting more difficult due to greater disparities in counts.

A scan of another quantum dot, with more prominent blinking and longer off-times than the one represented by Figure 7.2, is shown in Figure 7.3. The raw fluorescence data is shown as a dark gray trace in the figure. The actual location of the quantum dot was manually added to the figure and is shown as a light gray area, which is representative of the PSF convolution of the quantum dot. The red line in the figure is a Gaussian function fit using a standard least squares regression with appropriate constraints on size and position. The blue line in the figure is a Gaussian trace fit by utilizing only five data points from the CPR. As shown in Figure 7.2, the CPR reaches a minimum at the center of the quantum dot and a maximum near the edges. Despite the fact that only five data points were obtainable due to the low signal to noise, the CPR is fit to generate the blue line in Figure 7.3.

Particularly noteworthy is the fact that the center peak fit localizes the quantum dot at a position of 466 nm, only 15 nm from the actual location of 481 nm. The standard least squares regression fitting technique shows a location of 670 nm, a difference of 189 nm from the real value. Simply stated, if the blinking of a quantum dots is substantial, then it cannot be localized easily. However, utilization of the CPR to determine the location of a quantum dot can be extremely accurate even with minimal and erratic fluorescence from an emitter. This method of applying the CPR is suggestive of an

imaging technique that would be very useful when the emitter, nominally a quantum dot, displays a great deal of fluorescence intermittency.

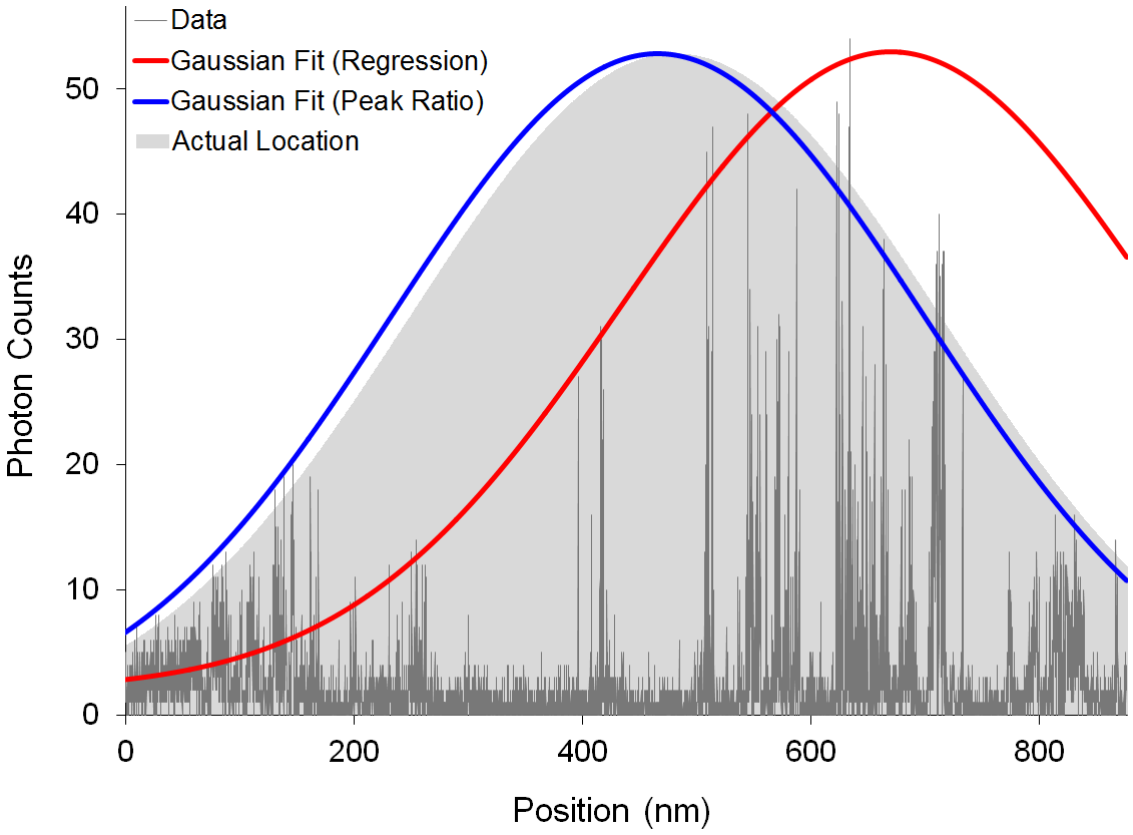

Figure 7.3: Using the CPR to localize a quantum dot. The fluorescence data with substantial blinking is shown in dark gray and a manually positioned Gaussian fit (solid light gray) shows the actual location of the quantum dot. A normal Gaussian fit by regression analysis is applied to the data (red line), while the Gaussian fit according to the CPR is shown by the blue line. All Gaussian fits are normalized for a more convenient comparison.

A higher resolution form of imaging utilizing the CPR was also applied by imaging a quantum dot in two dimensions. A 1 × 1 micrometer scan of a single quantum dot was conducted over the course of seven minutes. The image was broken up into 20 × 16 segments, resulting in 320 points where the CPR was calculated. The CPR at all 320 points for one of the quantum dots is shown in Figure 7.4. As noted in Figure 7.2, the

CPR is inversely proportional to the location of the quantum dot. Therefore, the image shown in Figure 7.4 is representative of the inverse shape of a particle. The MATLAB routine used to generate the image array is given in Appendix B.

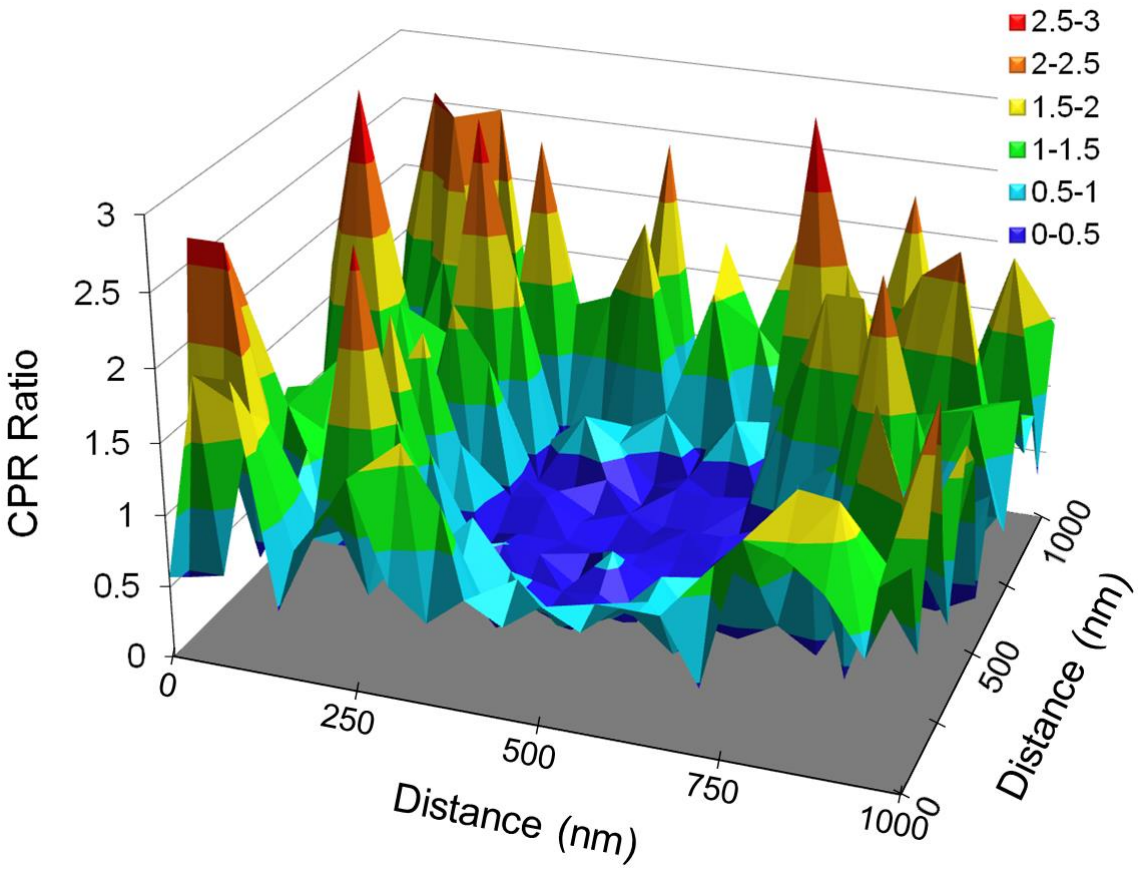

Figure 7.4: CPR over a 1 × 1 μm area scan of a single quantum dot. The legend is color coded to correspond to the vertical axis, which indicates the CPR.

The inverse of the CPR has been shown to provide an approximate outline of a quantum dot. This is demonstrated by the surface plot in Figure 7.5. A plot in this format could be used to visualize and localize a single quantum dot. This is especially useful when substantial blinking makes fitting to the fluorescence profile difficult.

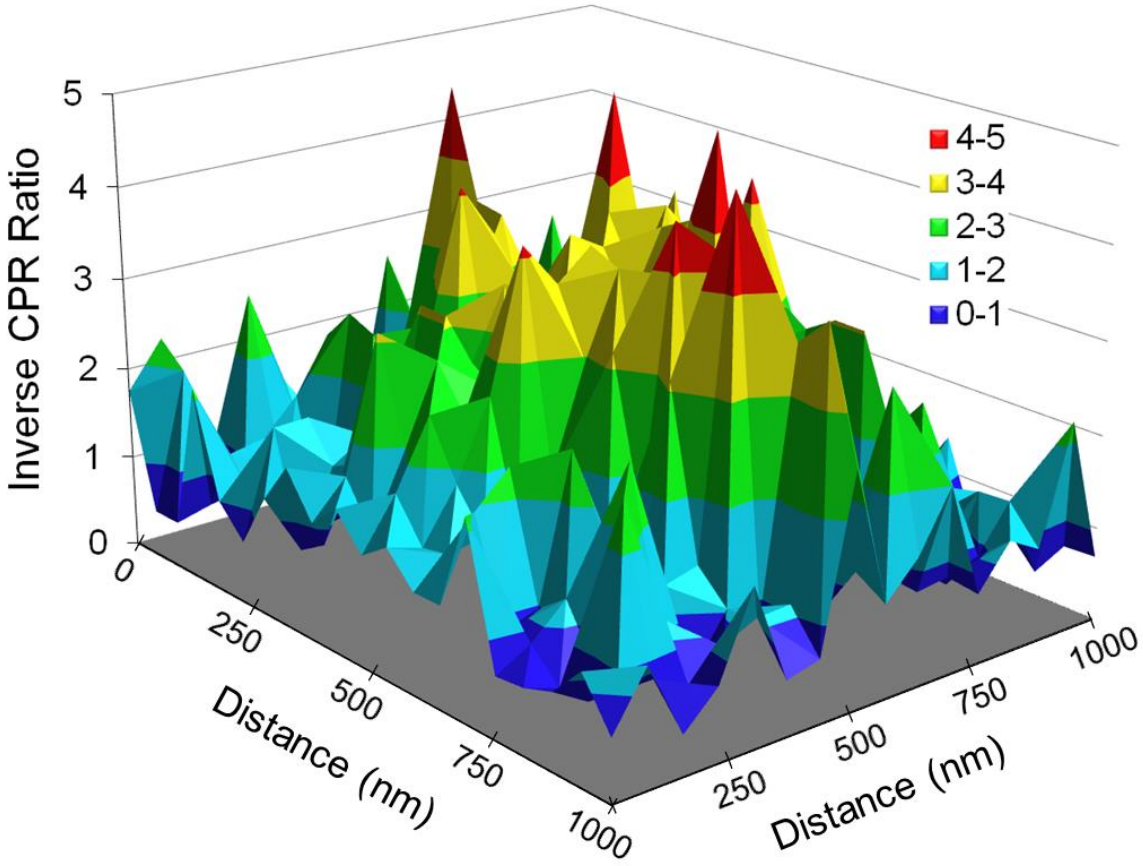

Figure 7.5: Inverse CPR of a 1 × 1 scan of a single quantum dot. An approximate outline of a single particle is rendered.

7.3 Elucidation and Application of Multiexciton Imaging

The extent of multiphoton emission has previously been shown to scale with excitation intensity.[62] However, results from this chapter demonstrate that the inherent intensity profile of the excitation beam across a single quantum dot does not affect the multiphoton emission in the same way. The exact opposite occurs, with the highest multiphoton emission occurring at the edges of the excitation beam, where the incident laser intensity is lowest. This is due to a well understood phenomenon in which excitation of a surface plasmon is most likely when incident light strikes the plasmonic surface at an angle where total internal reflection is possible.[79-81] Total internal reflection

is only possible when the incident angle of excitation light is greater than the critical angle. Since the light at the center of the excitation beam strikes the surface with a minimal incident angle, very little surface plasmon resonance is possible. However, at the edges of the excitation beam, a substantial proportion of the incident light strikes at a much higher angle, resulting in a higher probability of triggering surface plasmon resonance behavior. This effect is illustrated in Figure 7.6.

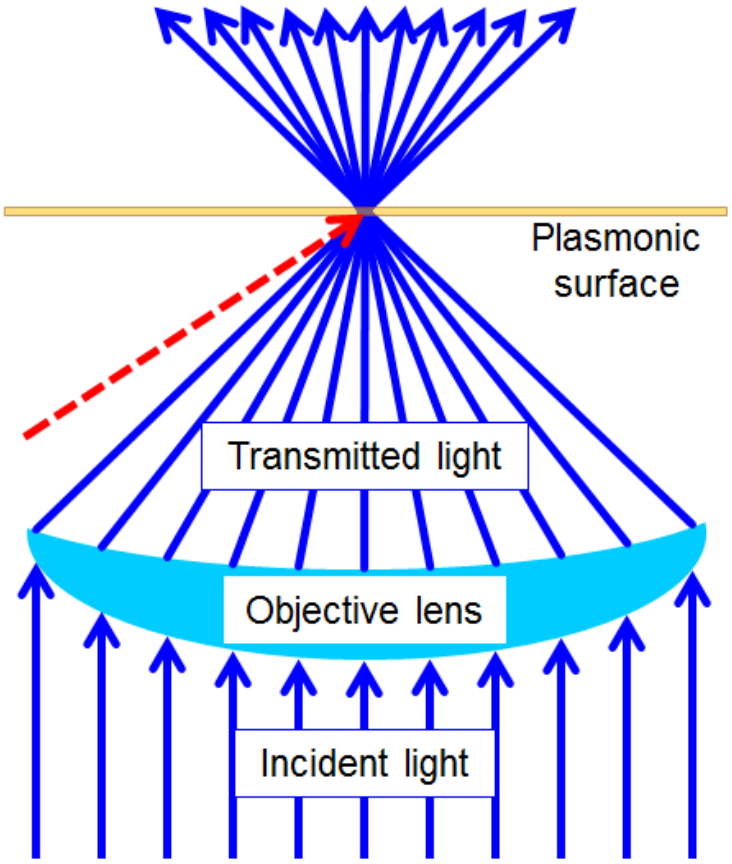

Figure 7.6: Refracted incident light and its ability to trigger surface plasmon resonance. Incident light is columnated and strikes the lens at different angles, resulting in different degrees of refraction. An approximated incident angle for ideal generation of surface plasmon resonance is shown by the red dotted arrow. Accordingly, the most highly refracted portions of the incident beam have the highest probability of coupling with the surface plamson.

The most refracted incident light is largely responsible for the generation of surface plasmons. Since the majority of the refracted light lies at the edges of excitation beam profile, it is expected that the highest probability of exciting surface plasmons will occur there. The CPR as a function of the location of the quantum dot, as shown in Figure 7.4, can therefore be explained. When the laser excitation beam is positioned at the center of the quantum dot, emission is dominated by incident light that failed to couple with the surface plasmon resonance due to a minimal incident angle for the majority of the excitation light. Near the edges, the refracted incident light dominates the excitation of the quantum dot while also coupling to the surface plasmon of the gold, thereby producing a high CPR.

Several advances in multiexcition imaging are still necessary before wide range application of this technique is possible. The signal to noise ratio must be increased substantially for multiple applications. Figures 7.4 and 7.5 are representative of data taken over the course of approximately seven minutes. Standard microscopy techniques generally need to function on much faster time scales. Thus far, the use of multiexcition imaging on appropriate timescales results in unusable data due to a signal dominated by noise. The additional limitation of a plasmonic material in close proximity to the emitter severely limits the applicability of this technique. However, development of an all-in-one semiconductor based nanocrystal with a plasmonic layer could resolve the issue.

CHAPTER 8: CONCLUSION AND FUTURE RESEARCH

We have demonstrated two new methods for measuring motion dynamics of any motor protein that moves along a filament or microtubule. Both methods have been shown to work well *in vitro* and could be applied to similar *in vivo* studies. The parked-beam method has been shown to offer superior temporal resolution in comparison to popular motion tracking techniques in use today. Both the parked-beam method and FSCM can be utilized in cellular environments where imaging depths on the order of several hundred nanometers to micrometers are desired. The techniques have each yielded motion dynamics parameters of myosin V that are well aligned with currently accepted values.

We have discovered a distinct blinking correlation between neighboring quantum dots through the use of FSCM. Coulomb interactions adequately explain the correlation with the corollary that multiple charging of individual quantum dots be possible. This assertion is supported by many experiments. The slow scan experiments showed that the blinking correlation effect is decreased given a greater temporal separation between the excitation of neighboring quantum dots. An increase in excitation intensity concurrently rises with blinking correlation while a higher tendency towards multiphoton emission decreases the blinking correlation. Each of these findings directly supports a multiple charging model of quantum dot excited state dynamics. Many aspects of currently proposed blinking models can be corroborated by the presence of blinking correlation.

Most notably, a charging model, in which a broad distribution of static external charge carrier trap sites exist, aligns best with our findings.

To further investigate our claim that a Coulomb interaction is primarily responsible for the observed blinking correlation, several experiments are being considered. Most experiments are designed to enhance the blinking correlation phenomenon to more readily study its origins. By varying any one of multiple parameters, including scan speed, matrix material, quantum dot construct, or externally applied electric fields, the blinking correlation may be altered. The development of switchable nanoscale emitters is also being considered. By optimizing the materials, size, or ligands of a quantum dot, it could be optimized to respond to very subtle changes in the surrounding electric field. Individual quantum dots could therefore be switched to fully emissive or non-emissive, depending on an applied electric field.

Additional work is also being done to develop the high resolution multiple exciton imaging technique. Despite the fact that nearly all quantum dots blink, they can still be precisely localized using this technique. Optimization of signal is the most important step in advancing the technique. Future work also includes the creation of an all-in-one plasmon enhanced semiconductor nanocrystal, which would support multiexcition imaging using a single particle.

The discovery of blinking correlation may emerge to be a revolutionary finding in the field of quantum dot photophysical models. It may also lead to the development of nanoscale devices with switchable fluorescent profiles. Two novel motor protein techniques are now available to be employed by researchers with access to a confocal microscope. Exploiting the multiphoton emission of quantum dots near a plasmonic

surface may soon lead to one or more high resolution imaging techniques. This is especially likely through the development of an all-in-one plasmon coupled nanocrystal construct.

REFERENCES

1 Ekimov, A. I. & Onushchenko, A. A. Quantum Size Effect in 3-Dimensional Microscopic Semiconductor Crystals. *Jetp Letters* **34**, 345-349 (1981).

2 Bruchez, M., Moronne, M., Gin, P., Weiss, S. & Alivisatos, A. P. Semiconductor nanocrystals as fluorescent biological labels. *Science* **281**, 2013-2016, doi:10.1126/science.281.5385.2013 (1998).

3 Chan, W. C. W. & Nie, S. M. Quantum dot bioconjugates for ultrasensitive nonisotopic detection. *Science* **281**, 2016-2018, doi:10.1126/science.281.5385.2016 (1998).

4 Mattoussi, H. *et al.* Self-assembly of CdSe-ZnS quantum dot bioconjugates using an engineered recombinant protein. *Journal of the American Chemical Society* **122**, 12142-12150, doi:10.1021/ja002535y (2000).

5 Pathak, S., Choi, S. K., Arnheim, N. & Thompson, M. E. Hydroxylated quantum dots as luminescent probes for in situ hybridization. *Journal of the American Chemical Society* **123**, 4103-4104, doi:10.1021/ja0058334 (2001).

6 Willard, D. M., Carillo, L. L., Jung, J. & Van Orden, A. CdSe-ZnS quantum dots as resonance energy transfer donors in a model protein-protein binding assay. *Nano Letters* **1**, 469-474, doi:10.1021/nl015565n (2001).

7 Lieberman, M. *et al.* Quantum-dot cellular automata at a molecular scale. *Molecular Electronics Ii* **960**, 225-239 (2002).

8 Tran, P. T., Goldman, E. R., Anderson, G. P., Mauro, J. M. & Mattoussi, H. Use of luminescent CdSe-ZnS nanocrystal bioconjugates in quantum dot-based nanosensors. *Physica Status Solidi B-Basic Research* **229**, 427-432, doi:10.1002/1521-3951(200201)229:1<427::aid-pssb427>3.0.co;2-k (2002).

9 Chen, Y. F. & Rosenzweig, Z. Amino acid and peptide capped CDS quantum dots (QDS) as novel Zn2+ions luminescent sensors. *Abstracts of Papers of the American Chemical Society* **223**, U67-U67 (2002).

10 Liang, J. G., Ai, X. P., He, Z. K. & Pang, D. W. Functionalized CdSe quantum dots as selective silver ion chemodosimeter. *Analyst* **129**, 619-622, doi:10.1039/b317044f (2004).

11 Greenham, N. C., Peng, X. G. & Alivisatos, A. P. Charge separation and transport in conjugated-polymer/semiconductor-nanocrystal composites studied by photoluminescence quenching and photoconductivity. *Physical Review B* **54**, 17628-17637, doi:10.1103/PhysRevB.54.17628 (1996).

12 Fogg, D. E. *et al.* Fabrication of quantum dot-polymer composites: Semiconductor nanoclusters in dual-function polymer matrices with electron-transporting and cluster-passivating properties. *Macromolecules* **30**, 8433-8439, doi:10.1021/ma970626i (1997).

13 Pan, D., Towe, E. & Kennerly, S. Photovoltaic quantum-dot infrared detectors. *Applied Physics Letters* **76**, 3301-3303, doi:10.1063/1.126613 (2000).

14 Shim, M. & Guyot-Sionnest, P. N-type colloidal semiconductor nanocrystals. *Nature* **407**, 981-983, doi:10.1038/35039577 (2000).

15 Nozik, A. J. Quantum dot solar cells. *Physica E-Low-Dimensional Systems & Nanostructures* **14**, 115-120, doi:10.1016/s1386-9477(02)00374-0 (2002).

16 Nirmal, M. *et al.* Fluorescence intermittency in single cadmium selenide nanocrystals. *Nature* **383**, 802-804, doi:10.1038/383802a0 (1996).

17 Efros, A. L. & Rosen, M. Random telegraph signal in the photoluminescence intensity of a single quantum dot. *Physical Review Letters* **78**, 1110-1113, doi:10.1103/PhysRevLett.78.1110 (1997).

18 Kuno, M., Fromm, D. P., Hamann, H. F., Gallagher, A. & Nesbitt, D. J. Nonexponential "blinking" kinetics of single CdSe quantum dots: A universal power law behavior. *Journal of Chemical Physics* **112**, 3117-3120, doi:10.1063/1.480896 (2000).

19 Brus, L. E. Electron-electron and electron-hole interactions in small semiconductor crystallites - The size dependence of the lowest excited electronic state. *Journal of Chemical Physics* **80**, 4403-4409, doi:10.1063/1.447218 (1984).

20 Rossetti, R., Ellison, J. L., Gibson, J. M. & Brus, L. E. Size effects in the excited electronic states of small colloidal CdS crystallites. *Journal of Chemical Physics* **80**, 4464-4469, doi:10.1063/1.447228 (1984).

21 Rossetti, R., Hull, R., Gibson, J. M. & Brus, L. E. Excited electronic states and optical spectra of ZnS and CdS crystallites in the almost-equal-to-15 to 50-A size range - Evolution from molecular to bulk semiconductor properties. *Journal of Chemical Physics* **82**, 552-559, doi:10.1063/1.448727 (1985).

22 Murray, C. B., Norris, D. J. & Bawendi, M. G. Synthesis and Characterization of Nearly Monodisperse CdE (E=S, Se, Te) Semiconductor Nanocrystallites. *Journal of the American Chemical Society* **115**, 8706-8715, doi:10.1021/ja00072a025 (1993).

23 Liu, W. *et al.* Compact biocompatible quantum dots functionalized for cellular imaging. *Journal of the American Chemical Society* **130**, 1274-1284, doi:10.1021/ja076069p (2008).

24 Larson, D. R. *et al.* Water-soluble quantum dots for multiphoton fluorescence imaging in vivo. *Science* **300**, 1434-1436, doi:10.1126/science.1083780 (2003).

25 Choi, H. S. *et al.* Renal clearance of quantum dots. *Nature Biotechnology* **25**, 1165-1170, doi:10.1038/nbt1340 (2007).

26 Verberk, R., van Oijen, A. M. & Orrit, M. Simple model for the power-law blinking of single semiconductor nanocrystals. *Physical Review B* **66**, doi:10.1103/PhysRevB.66.233202 (2002).

27 Zhang, K., Chang, H. Y., Fu, A. H., Alivisatos, A. P. & Yang, H. Continuous distribution of emission states from single CdSe/ZnS quantum dots. *Nano Letters* **6**, 843-847, doi:10.1021/nl060483q (2006).

28 Amecke, N. & Cichos, F. Intermediate intensity levels during the emission intermittency of single CdSe/ZnS quantum dots. *Journal of Luminescence* **131**, 375-378, doi:10.1016/j.jlumin.2010.10.026 (2011).

29 Gomez, D. E., van Embden, J., Mulvaney, P., Fernee, M. J. & Rubinsztein-Dunlop, H. Exciton-Trion Transitions in Single CdSe-CdS Core-Shell Nanocrystals. *Acs Nano* **3**, 2281-2287, doi:10.1021/nn900296q (2009).

30 Spinicelli, P. *et al.* Bright and Grey States in CdSe-CdS Nanocrystals Exhibiting Strongly Reduced Blinking. *Physical Review Letters* **102** (2009).

31 Ye, M. & Searson, P. C. Blinking in quantum dots: The origin of the grey state and power law statistics. *Physical Review B* **84** (2011).

32 Zhao, J., Nair, G., Fisher, B. R. & Bawendi, M. G. Challenge to the Charging Model of Semiconductor-Nanocrystal Fluorescence Intermittency from Off-State Quantum Yields and Multiexciton Blinking. *Physical Review Letters* **104**, doi:10.1103/PhysRevLett.104.157403 (2010).

33 Califano, M. Off-State Quantum Yields in the Presence of Surface Trap States in CdSe Nanocrystals: The Inadequacy of the Charging Model To Explain Blinking. *Journal of Physical Chemistry C* **115**, 18051-18054, doi:10.1021/jp203736y (2011).

34 Klimov, V. I., Mikhailovsky, A. A., McBranch, D. W., Leatherdale, C. A. & Bawendi, M. G. Quantization of multiparticle Auger rates in semiconductor quantum dots. *Science* **287**, 1011-1013, doi:10.1126/science.287.5455.1011 (2000).

35 Fisher, B., Caruge, J. M., Zehnder, D. & Bawendi, M. Room-temperature ordered photon emission from multiexciton states in single CdSe core-shell nanocrystals. *Physical Review Letters* **94**, doi:10.1103/PhysRevLett.94.087403 (2005).

36 Rosen, S., Schwartz, O. & Oron, D. Transient Fluorescence of the Off State in Blinking CdSe/CdS/ZnS Semiconductor Nanocrystals Is Not Governed by Auger Recombination. *Physical Review Letters* **104**, doi:10.1103/PhysRevLett.104.157404 (2010).

37 Tang, J. & Marcus, R. A. Mechanisms of fluorescence blinking in semiconductor nanocrystal quantum dots. *Journal of Chemical Physics* **123**, 12, doi:10.1063/1.1993567 (2005).

38 Shimizu, K. T. *et al.* Blinking statistics in single semiconductor nanocrystal quantum dots. *Physical Review B* **63**, 5, doi:10.1103/PhysRevB.63.205316 (2001).

39 Riley, E. A., Hess, C. M. & Reid, P. J. Photoluminescence Intermittency from Single Quantum Dots to Organic Molecules: Emerging Themes. *International Journal of Molecular Sciences* **13**, 12487-12518, doi:10.3390/ijms131012487 (2012).

40 Brown, R. H. & Twiss, R. Q. Correlation between photons in 2 coherent beams of light. *Nature* **177**, 27-29, doi:10.1038/177027a0 (1956).

41 Yildiz, A. *et al.* Myosin V walks hand-over-hand: Single fluorophore imaging with 1.5-nm localization. *Science* **300**, 2061-2065, doi:10.1126/science.1084398 (2003).

42 Funatsu, T., Harada, Y., Tokunaga, M., Saito, K. & Yanagida, T. Imaging of single fluorescent molecules and individual ATP turnovers by single myosin molecules in aqueous-solution. *Nature* **374**, 555-559, doi:10.1038/374555a0 (1995).

43 Tokunaga, M., Kitamura, K., Saito, K., Iwane, A. H. & Yanagida, T. Single molecule imaging of fluorophores and enzymatic reactions achieved by objective-type total internal reflection fluorescence microscopy. *Biochemical and Biophysical Research Communications* **235**, 47-53, doi:10.1006/bbrc.1997.6732 (1997).

44 Kinosita, K. F-1-ATPase: A rotary motor that can work at near 100% efficiency. *Faseb Journal* **14**, A1586-A1586 (2000).

45 Kaksonen, M., Toret, C. P. & Drubin, D. G. A modular design for the clathrin- and actin-mediated endocytosis machinery. *Cell* **123**, 305-320, doi:10.1016/j.cell.2005.09.024 (2005).

46 Holden, S. J. *et al.* Defining the Limits of Single-Molecule FRET Resolution in TIRF Microscopy. *Biophysical Journal* **99**, 3102-3111, doi:10.1016/j.bpj.2010.09.005 (2010).

47 Pierobon, P. *et al.* Velocity, Processivity, and Individual Steps of Single Myosin V Molecules in Live Cells. *Biophysical Journal* **96**, 4268-4275, doi:10.1016/j.bpj.2009.02.045 (2009).

48 Mehta, A. D. *et al.* Myosin-V is a processive actin-based motor. *Nature* **400**, 590-593 (1999).

49 Gebhardt, J. C. M., Clemen, A. E. M., Jaud, J. & Rief, M. Myosin-V is a mechanical ratchet. *Proceedings of the National Academy of Sciences of the United States of America* **103**, 8680-8685, doi:10.1073/pnas.0510191103 (2006).

50 De La Cruz, E. M., Wells, A. L., Rosenfeld, S. S., Ostap, E. M. & Sweeney, H. L. The kinetic mechanism of myosin V. *Proceedings of the National Academy of Sciences of the United States of America* **96**, 13726-13731 (1999).

51 Vale, R. D. & Milligan, R. A. The way things move: Looking under the hood of molecular motor proteins. *Science* **288**, 88-95 (2000).

52 Schott, D. H., Collins, R. N. & Bretscher, A. Secretory vesicle transport velocity in living cells depends on the myosin-V lever arm length. *Journal of Cell Biology* **156**, 35-39, doi:10.1083/jcb.200110086 (2002).

53 Levi, V., Serpinskaya, A. S., Gratton, E. & Gelfand, V. Organelle transport along microtubules in Xenopus melanophores: Evidence for cooperation between multiple motors. *Biophysical Journal* **90**, 318-327, doi:10.1529/biophysj.105.067843 (2006).

54 Sun, Y. *et al.* Single-molecule stepping and structural dynamics of myosin X. *Nature Structural & Molecular Biology* **17**, 485-U131, doi:10.1038/nsmb.1785 (2010).

55 Craddock, T. J. A., Tuszynski, J. A., Priel, A. & Freedman, H. Microtubule ionic conduction and its implications for higher cognitive functions. *Journal of Integrative Neuroscience* **9**, 103-122, doi:10.1142/s0219635210002421 (2010).

56 Wu, P. G. & Brand, L. Resonance Energy Transfer - Methods and Applications. *Analytical Biochemistry* **218**, 1-13, doi:10.1006/abio.1994.1134 (1994).

57 Nair, G., Zhao, J. & Bawendi, M. G. Biexciton Quantum Yield of Single Semiconductor Nanocrystals from Photon Statistics. *Nano Letters* **11**, 1136-1140, doi:10.1021/nl104054t (2011).

58 Empedocles, S. A. & Bawendi, M. G. Influence of spectral diffusion on the line shapes of single CdSe nanocrystallite quantum dots. *Journal of Physical Chemistry B* **103**, 1826-1830, doi:10.1021/jp983305x (1999).

59 Neuhauser, R. G., Shimizu, K. T., Woo, W. K., Empedocles, S. A. & Bawendi, M. G. Correlation between fluorescence intermittency and spectral diffusion in single semiconductor quantum dots. *Physical Review Letters* **85**, 3301-3304, doi:10.1103/PhysRevLett.85.3301 (2000).

60 Shim, M. & Guyot-Sionnest, P. Permanent dipole moment and charges in colloidal semiconductor quantum dots. *Journal of Chemical Physics* **111**, 6955-6964, doi:10.1063/1.479988 (1999).

61 Leatherdale, C. A., Woo, W. K., Mikulec, F. V. & Bawendi, M. G. On the absorption cross section of CdSe nanocrystal quantum dots. *Journal of Physical Chemistry B* **106**, 7619-7622, doi:10.1021/jp025698c (2002).

62 LeBlanc, S. J., McClanahan, M. R., Jones, M. & Moyer, P. J. Enhancement of Multiphoton Emission from Single CdSe Quantum Dots Coupled to Gold Films. *Nano Letters* **13**, 1662-1669, doi:10.1021/nl400117h (2013).

63 Dekel, E. *et al.* Multiexciton spectroscopy of a single self-assembled quantum dot. *Physical Review Letters* **80**, 4991-4994, doi:10.1103/PhysRevLett.80.4991 (1998).

64 Achermann, M., Hollingsworth, J. A. & Klimov, V. I. Multiexcitons confined within a subexcitonic volume: Spectroscopic and dynamical signatures of neutral and charged biexcitons in ultrasmall semiconductor nanocrystals. *Physical Review B* **68**, doi:10.1103/PhysRevB.68.245302 (2003).

65 Caruge, J. M., Chan, Y. T., Sundar, V., Eisler, H. J. & Bawendi, M. G. Transient photoluminescence and simultaneous amplified spontaneous emission from multiexciton states in CdSe quantum dots. *Physical Review B* **70**, doi:10.1103/PhysRevB.70.085316 (2004).

66 Zhao, J., Chen, O., Strasfeld, D. B. & Bawendi, M. G. Biexciton Quantum Yield Heterogeneities in Single CdSe (CdS) Core (Shell) Nanocrystals and Its Correlation to Exciton Blinking. *Nano Letters* **12**, 4477-4483, doi:10.1021/nl3013727 (2012).

67 Galland, C. *et al.* Two types of luminescence blinking revealed by spectroelectrochemistry of single quantum dots. *Nature* **479**, 203-U275 (2011).

68 Javaux, C. *et al.* Thermal activation of non-radiative Auger recombination in charged colloidal nanocrystals. *Nature Nanotechnology* **8**, 206-212, doi:10.1038/nnano.2012.260 (2013).

69 Dahan, M. *et al.* Time-gated biological imaging by use of colloidal quantum dots. *Optics Letters* **26**, 825-827, doi:10.1364/ol.26.000825 (2001).

70 Margolin, G., Protasenko, V., Kuno, M. & Barkai, E. in *Fractals, Diffusion, and Relaxation in Disordered Complex Systems, Part A* Vol. 133 *Advances in Chemical Physics* 327-356 (2006).

71 Frantsuzov, P. A. & Marcus, R. A. Explanation of quantum dot blinking without the long-lived trap hypothesis. *Physical Review B* **72**, doi:10.1103/PhysRevB.72.155321 (2005).

72 Frantsuzov, P. A., Volkan-Kacso, S. & Janko, B. Model of Fluorescence Intermittency of Single Colloidal Semiconductor Quantum Dots Using Multiple Recombination Centers. *Physical Review Letters* **103**, doi:10.1103/PhysRevLett.103.207402 (2009).

73 Walsh, C. B. & Franses, E. I. Ultrathin PMMA films spin-coated from toluene solutions. *Thin Solid Films* **429**, 71-76, doi:10.1016/s0040-6090(03)00031-2 (2003).

74 Mohajerani, E., Farajollahi, F., Mahzoon, R. & Baghery, S. Morphological and thickness analysis for PMMA spin coated films. *Journal of Optoelectronics and Advanced Materials* **9**, 3901-3906 (2007).

75 Shimizu, K. T., Woo, W. K., Fisher, B. R., Eisler, H. J. & Bawendi, M. G. Surface-enhanced emission from single semiconductor nanocrystals. *Physical Review Letters* **89**, doi:10.1103/PhysRevLett.89.117401 (2002).

76 Anger, P., Bharadwaj, P. & Novotny, L. Enhancement and quenching of single-molecule fluorescence. *Physical Review Letters* **96**, doi:10.1103/PhysRevLett.96.113002 (2006).

77 Fu, Y. & Lakowicz, J. R. Modification of single molecule fluorescence near metallic nanostructures. *Laser & Photonics Reviews* **3**, 221-232, doi:10.1002/lpor.200810035 (2009).

78 Lee, K. S. & El-Sayed, M. A. Gold and silver nanoparticles in sensing and imaging: Sensitivity of plasmon response to size, shape, and metal composition. *Journal of Physical Chemistry B* **110**, 19220-19225, doi:10.1021/jp062536y (2006).

79 Boardman, A. D. *Electromagnetic surface modes*. (Wiley, 1982).

80 Liedberg, B., Nylander, C. & Lundstrom, I. Surface-Plamson Resonance for Gas-Detection and Biosensing. *Sensors and Actuators* **4**, 299-304, doi:10.1016/0250-6874(83)85036-7 (1983).

81 Welford, K. Surface-Plasmon Polaritons and Their Uses. *Optical and Quantum Electronics* **23**, 1-27, doi:10.1007/bf00619516 (1991).

APPENDIX A: MATLAB CODE FOR BLINKING CORRELATION ANALYSIS

```
%% This routine takes a 512 x 512 text image file (array) and finds
%% the PPMCC on two sets of data that are each 11 pixels wide.  It is
%% designed for use with the fast-scanning confocal microscopy
%% technique.
% 2013 by Ryan Hefti

% Close all figures
close all;
% Delete all variables other than the file location and text file name
clearvars -except pathname1 savefile1;
% Establish the default to directory (unless the directory is defined
% from this routine already) to open files and then choose the file
if exist('pathname1','var');
    [filename, pathname] = uigetfile('*.txt', 'Choose the file you wish
to import.',pathname1);
else
    [filename, pathname] = uigetfile('*.txt', 'Choose the file you wish
to import.');
end
% This opens the file specified
fopen([pathname filename]);
% Define a variable using all of the image data imported
fullimage1 = importdata([pathname filename]);
% Sum up one dimension of the array to see the layout of quantum dots
columns1 = sum(fullimage1, 1);

% The following variable defines the scan range of the image (in nm).
% It is not included as a prompt since the vast majority of images are
% 3 micrometer scan ranges.  Alter as necessary.
scanrange1 = 3000;

% Now for the figure
bcfig1 = figure('Color',[.9 1 1]);

% Create axes
axes1 = axes('Parent',bcfig1,...
    'XTick',[0 20 40 60 80 100 120 140 160 180 200 220 240 260 280 300
320 340 360 380 400 420 440 460 480 500 520],...
    'XMinorTick','on',...
    'XAxisLocation','top',...
    'XGrid','on',...
    'Position',[0.04 0.01 0.96 0.95]);

xlim(axes1,[0 512]);
hold(axes1,'all');

% Create plot
plot(columns1,'LineWidth',2,'DisplayName','First trace',...
    'Color',[0 0 0]);
set(bcfig1,'Position',[100 100 800 600]);
set(bcfig1, 'menubar', 'none');
```

```
% Prompt for peak value corresponding to the first quantum dot to be
% analyzed
prompt = 'What is the integer value of the peak you want to use (>5;
<507)? ';
peak1 = input(prompt);

% Generate blinking binary string with the following steps:
% Extract only the 11 lines needed for correlation
data1 = fullimage1(1:511, peak1-5:peak1+5);
% Sum those 11 lines
columns2 = sum(data1, 2);
% Find the average counts of the sum across all 512 points
avg1 = mean(columns2);
% Convert each point from the sum to a "1" or a "0" by comparing it to
% the average
binary1 = columns2 > avg1;

% Now for the second data string (basically repeating all of the
% commands).  This section will be commented less since it's so similar
% to the first section of code.
[filename1, pathname1] = uigetfile('*.txt', 'Choose the file you wish
to import.',pathname);
fopen([pathname1 filename1]);
fullimage11 = importdata([pathname1 filename1]);
columns11 = sum(fullimage11, 1);

% The figure
bcfig11 = figure('Color',[0.9 1 1]);

% Create axes
axes11 = axes('Parent',bcfig11,...
    'XTick',[0 20 40 60 80 100 120 140 160 180 200 220 240 260 280 300
320 340 360 380 400 420 440 460 480 500 520],...
    'XMinorTick','on',...
    'XAxisLocation','top',...
    'XGrid','on',...
    'Position',[0.04 0.01 0.96 0.95]);

xlim(axes11,[0 512]);
hold(axes11,'all');

% Create plot
plot(columns11,'LineWidth',2,'DisplayName','Second trace',...
    'Color',[0 0 0]);
set(bcfig11,'Position',[100 100 800 600]);
set(bcfig11, 'menubar', 'none');

% Prompt for peak value
prompt = 'What is the integer value of the peak you want to use (>5;
<507)? ';
peak11 = input(prompt);

% Generate blinking binary string
data11 = fullimage11(1:511, peak11-5:peak11+5);
columns12 = sum(data11, 2);
```

```
avg11 = mean(columns12);
binary11 = columns12 > avg11;

% Determine the correlation between the two quanum dots' blinking
appmcc1 = corr(binary1,binary11);

% Calculate the error in the PPMCC value
% First, an array is preallocated as it will be filled by a set number
% of values (nominally 1000 of them)
pixelval = zeros(1000,1); % preallocate
% Using the randn function, this will generate new sum strings of the
% original two data sets by adding a random number to them
% The average of the new "randomized" strings will be taken again and
% turned into binary strings, just like above
% The strings are then correlated
% Finally, after this is done 1000 times (or whatever pixelval is set
% to), the standard deviation of all of those correlation values is
% reported and used as the error in the PPMCC

for ix=1:1000
    error1 = columns2 + (randn(511,1)*(avg1/2));
    error12 = columns12 + (randn(511,1)*(avg11/2));
    avg2 = mean(error1);
    avg12 = mean(error12);
    binary2 = error1 > avg2;
    binary12 = error12 > avg12;
    pixelval(ix) = corr(binary2,binary12);
end
appmcce1=std(pixelval);

% Calculate distance between the dots
ddist1 = (scanrange1/512)*abs(peak11-peak1);

% Save all values to a text file
% First, the name of the text file, if not already established, is
$ written.
% The columns names are printed into the file
% These 2 steps occur only if save file with column names is not
% already established due to running the routine previously
% The file is then opened with write access so it is ready
if exist('savefile1','var')<0.5;
    prompt1 = 'Name the text storage file and add ".txt" to the name.
';
    savefile1 = input(prompt1,'s');
    fileID = fopen(savefile1,'a');
    fprintf(fileID, '%10s %10s %10s %25s %5s %25s %5s\r\n',...
        'Corr','CorrErr','Dist_(nm)','File1','Line1','File2','Line2');
else fileID = fopen(savefile1,'a');
end
% The format for adding data to the text file is eatablished
myformat1 = '%10.6f %10.6f %10.2f %25s %5.0f %25s %5.0f\r';
% There is an option to truncate the filename if so desired (using the
% line beginning with "file1")
% The spaces are converted to underscores so that the text file is
% truly space delimited
file1 = filename;
```

```
% use this line in place of the previous line to shorten filename:
% file1 = filename(end-16:end-4);
file3 = strrep(file1,' ','_');
file2 = filename1;
% use this line in place of the previous line to shorten filename1:
% file2 = filename1(end-16:end-4);
file4 = strrep(file2,' ','_');
% All needed data is written to the save file
fprintf(fileID, myformat1, appmcc1, appmcce1, ddist1, file3, peak1,
file4, peak11);
% The save file is closed and the two image files are closed
fclose(fileID);
fclose('all');
```

APPENDIX B: MATLAB CODE FOR 3D MUXI ANALYSIS

```
%% This routine uses the space delimited data generated by t3rmuxi.m
%% and generates an array of the center-to-outside peak ratio for 320
%% locations.  Only data taken over >450 seconds with a scan speed of
%% 20 pixels per second and a resolution of 1024 x 8 pixels is
%% currently accepted.  Small changes in the code can accomodate
%% experiments with alternate parameters.  Future iterations of the
%% code will allow for user-input parameters to allow for a variety of
%% possibilities.
%%
% 2013 by Ryan Hefti

% Placeholder number
width2=10000;

% Loop to correct for start time of the HBT detectors compared to the
% imaging start.
for crop1 = 1:10;
    % The relevant channel from the bursts file from t3rmuxi.m is
    % extracted.
    m1 = bursts(:,2);
    % Certain photons are removed from the file to assure that the
    % image is aligned with the HBT detected photons.
    m2 = m1(crop1:crop1+319);
    % The remaining collected photons are arranged into 20 rows by 16
    % columns, equivalent to the imaging resolution (given that 8 x 2 =
    % 16 due to raster scanning)
    m5 = reshape(m2, 20, 16);
    % Reverse every other column since the raster scan is essentially
    % traveling in a reverse direction.
    m5(:, [1 3 5 7 9 11 13 15]) = flipud(m5(:, [1 3 5 7 9 11 13 15]));
    % Sum the data to establish an overall dot profile, used for
    % Gaussian fitting and establishing the proper alignment of the HBT
    % detectors and the scanner.
    m6 = sum(m5, 2);
    % Set up the x values for the Gaussian fitting.
    xdata = 1:20;
    % Set up the y values for the Gaussian fitting.
    ydata = transpose(m6);
    % Establish the maximum value of y to use as a starting guess.
    max1 = max(m6(:));
    % Starting guess for Gaussian fit.
    x0 = [max1; 10; 1];
    % Call the Gaussian fitting function.
    [x,resnorm] = lsqcurvefit(@gaussianfit1,x0,xdata,ydata);
    % Check the width of the function, which should be minimized to
    % show the best fit.
    width1=x(3);
    % Compare the width from previous iterations of the loop.
    % Establish a new cropping value if the width improves.
    if width1<width2;
        cropping1=crop1;
        width2=width1;
    elseif width2==10000;
```

```
        width2=width1;
    end;
end;

% Extract HBT photons from the main data file generated by t3rmuxi.m.
xx4=dlmread(outfile,' ',2,0);
% The extraction must be reformatted to a 2 column matrix, which is
% accomplished with the next 3 lines.
xx5 = transpose(xx4);
xx6 = xx5(xx5~=0);
xx7 = vec2mat(xx6,2);

% Clean up variables a bit.
clearvars -except xx7 bursts lifetime_hist outfile cropping1;

% Set counter to 0
ctr1=0;
% Apply the cropping value located earlier.
crp1=cropping1-1;
% Preallocate an array.
xx33=zeros(20,16);

% Loop that writes all 320 center-to-outside peak ratios to a variable.
for ii=(crp1*1.28):1.28:408.32;
    % Establish where in the main array to write the next ratio.
    ctr1=ctr1+1;
    % Create an index array for only the data from this segment of the
    % array.
    xx8 = xx7(:,1) < (ii+1.28) & xx7(:,1)>ii;
    % Convert the index array to two identical columns.
    xx9=[xx8,xx8];
    % Apply the index to the extracted data to obtained only the
    % desired values, namely the photon arrival times and their
    % corresponding bins.
    xx10=xx7(xx9);
    % Convert back to a 2 column array
    xx11=reshape(xx10,[],2);
    % Extract only the second column (the bins).
    xx12=xx11(:,2);
    % Index the bins that correspond to the center peak.
    xx14=xx12>218 & xx12<274;
    % Sum the index to give the total center peak counts.
    xx15=sum(xx14);
    % Index the bins that correspond to the first side peak.
    xx16=xx12>110 & xx12<166;
    % Sum the index to give the total (first) side peak counts.
    xx17=xx12>324 & xx12<380;
    % Index the bins that correspond to the second side peak.
    xx19=sum(xx16);
    % Sum the index to give the total (second) side peak counts.
    xx20=sum(xx17);
    % Add the counts from both side peaks.
    xx21=xx20+xx19;
    % Calculate the ratio and use a factor of 2 to account for the
    % inclusion of both side peaks.
    ratio1=(xx15)/(xx21)*2;
```

```
    % Write the ratio value into the appropriate location in the main
    % array, which was established earlier.
    xx33(ctr1)=ratio1;
end

% Inverse of the main array to show approximate dot profile.
xx44=1./xx33;


% Gaussian fit function referenced by muxi3d.m (titled gaussianfit.m)
function F = gaussianfit1(x,xdata);
F = x(1)*exp(-(xdata-x(2)).^2/(2*(x(3).^2)));


%% This is the t3rmuxi.m routine used before the previous routine.
%% Adapted from demo for accessing TimeHarp TTTR data files (*.t3r)
%% from MATLAB TimeHarp 200, Software version 6.0, Format version 6.0
%% Peter Kapusta, PicoQuant GmbH 2006

% Revised 5 Nov 2007 Wes Parker
% Revised 2013 by Ryan Hefti

clear all;
clc;
fprintf(1,'\n');

%init array counter

j=1;

%desired bintime (in ms)

DesiredBintime = 1280;
bintime = DesiredBintime/1000;

%  read data file

[filename, pathname]=uigetfile('*.t3r', 'TTTR data:');
fid=fopen([pathname filename]);

fprintf(1,'============================================================
===== \n');
fprintf(1,'  Content of %s : \n', strcat(pathname, filename));
fprintf(1,'============================================================
===== \n');
fprintf(1,'\n');

fseek(fid,368,'bof');

AcquisitionTime = fread(fid, 1, 'int32');
fprintf(1,'Acquisition Time: %d ms \n', AcquisitionTime);
TotalBins = AcquisitionTime/DesiredBintime+1;
fprintf(1,'bintime: %d ms \n', DesiredBintime);
```

```
fprintf(1,'Total Bins: %d bins \n', TotalBins);

fseek(fid,588,'bof');

TTTRGlobclock = fread(fid, 1, 'int32');
fprintf(1,'TTTR Global Clock: %d ns\n', TTTRGlobclock);

fseek(fid,40,'cof');

NumberOfRecords = fread(fid, 1, 'int32');
fprintf(1,'Number Of Records: %d\n', NumberOfRecords);

fseek(fid,4,'cof');

%  Set up arrays for histogram and bursts
%  Right now, we assume 60 sec data collection, make this variable
later

lifetime_hist = zeros(4096,2);
bursts = zeros(TotalBins,2);

%  This reads and interpret the TTTR event records
outfile = [pathname filename(1:length(filename)-3) 'txt'];

fpout = fopen(outfile,'W');

fprintf(1,'\n');
fprintf(1,'Writing data to %s\n', outfile);
fprintf(1,'This may take a while ...');

% set up screen progress counter

endvalue=NumberOfRecords;
required_blanks=ceil(log10(endvalue))+1;
backspace_string='';
for l=1:required_blanks
    backspace_string=strcat(backspace_string,'\b');
end
% build format_string: put backspaces in, define format specifier
(leftalign)
format_string = [backspace_string '%-' num2str(required_blanks) 'd'];

fprintf(1, '\nProcessing record: \n\n\n\n\n\n\n');
fprintf(1,'\n');

Ofltime = 0;
Photon = 0;
Overflow = 0;
Marker = 0;

for i=0:NumberOfRecords-1
    fprintf(1,format_string, i);
    TTTRRecord = fread(fid, 1, 'uint32');
    TimeTag = bitand(TTTRRecord,65535);        %the lowest 16 bits
```

```
    Channel = bitand(bitshift(TTTRRecord,-16),4095); %the next 12 bits
    Route   = bitand(bitshift(TTTRRecord,-28),3);    %the next 2 bits
    Valid   = bitand(bitshift(TTTRRecord,-30),1);    %the next bit

    Truetime = (Ofltime + TimeTag) * TTTRGlobclock * 1e-9;

    if Valid
        fprintf(fpout,'%11.7f  %5u\n', Truetime, Channel);
        Photon = Photon + 1;

        %  set up histogram

        lifetime_hist(4096-Channel, Route+1)=lifetime_hist(4096-
Channel, Route+1)+1;

        %record bursts in time interval

        if Truetime < bintime

            % If I am in the current subset of data then
            % determine burst array element photon goes in.
            % Using ceil function allows me to find the correct row
number
            BurstBin = ceil((Truetime-(bintime-
(DesiredBintime/1000)))/(DesiredBintime/1000));
            %record number of photon counts in burst interval

            bursts(BurstBin,Route+1)=bursts(BurstBin,Route+1)+1;
        else
            % We can't forget that we have to account for the current
            % photon event
            BurstBin = ceil((Truetime-(bintime-
(DesiredBintime/1000)))/(DesiredBintime/1000));
            bursts(BurstBin,Route+1)=bursts(BurstBin,Route+1)+1;
        end;



    else %this means we have a special record
        if bitand(Channel,2048) %this is an overflow record
            Overflow = Overflow + 1;
            Ofltime = Ofltime + 65536;
        end;
        if bitand (Channel,7)   %this is a marker
            Marker = Marker + 1;
        end;
    end;


end;
fclose(fid);
fclose(fpout);

time = zeros(TotalBins,1);
```

```
for i=1:TotalBins
    time(i)=DesiredBintime*i;
end

% Save results

save bursts.txt bursts -ascii -tabs;
save lifetime_hist.txt lifetime_hist -ascii -tabs;

fprintf(1,' Ready!\n');
fprintf(1,'\nStatistics:\n');
fprintf(1,'\n%u photon records', Photon);
fprintf(1,'\n%u overflows', Overflow);
fprintf(1,'\n%u markers', Marker);
```